(NASA-CR-163852) HEAT STORAGE IN ALLOY TRANSFORMATIONS Final Report (Delaware Univ.) 163 p HC A08/MF A01 CSCL 10C

N81-15466

Unclas
G3/44 29704

Final Report

Heat Storage in Alloy Transformations

C. Ernest Birchenall, principal investigator
Selçuk İ. Güçeri, associate investigator
Diana Farkas
Michael B. Labdon
Nikhil Nagaswami
Bruce Pregger

University of Delaware, Newark, Delaware 19711
December, 1980

Prepared for
National Aeronautics and Space Administration
Lewis Research Center
Cleveland, Ohio 44135
Under Grant NSG-3184

for
U. S. Department of Energy
Energy Technology
Energy Storage Systems Division
Washington, D. C. 20545
Under Interagency Agreement EC-77-A-31-1034

Heat Storage in Alloy Transformations

Introduction

This project has explored the eutectic transformation of alloys containing plentiful metals as a means of storing heat at moderately high temperatures. In the course of this work, the theory of eutectic transformation was examined to find guidelines to the best material combinations to examine. The heats of transformation were measured calorimetrically, and the volume changes of expanding solid mixtures and homogeneous liquid solutions, and especially during the transformation between the two states at fixed temperature,were measured by changes in X-ray absorption. Heat flow models appropriate to storage in phase change materials have been developed along with efficient calculating procedures so that the relative importance of the problems associated with energy storage density, heat conduction and similar properties can be assessed in light of what is possible now. In the plan to use alloy eutectics as heat storage media the one step that is not completely resolved and demonstrated is containment in a manner that will retain the advantages of excellent thermal conductivity. It has been demonstrated that silicon carbide resists attack by the molten storage alloys. However, it has not been demonstrated that carbide films can be grown on oxidation resistant alloys and

retained through many melting and freezing cycles of the storage system. It has been proposed to extend the research work in this direction so that working storage systems can be designed and tested once containment is assured.

This report is constructed with the cited conditions in mind. The first section is a summary statement intended to show what has been accomplished in preparing heat storage systems utilizing alloy eutectic transformations as the working core. The discussion is in fairly general terms, because the detailed support for the statements is given in a series of extended appendices. The appendices are reprints of published papers or papers being prepared for publication. In several cases more extended discussion of the topics is available in Master's or Ph.D. theses accepted by the University of Delaware or which soon will be submitted to the faculty of the University of Delaware.

Heat Storage in Eutectic Alloys

Appendix A, "Heat Storage in Eutectic Alloys," by C. Ernest Birchenall and Alan F. Riechman, Met. Trans. A, 11A, 1415-1420 (1980), contains the thermodynamic equations governing eutectic transformations in binary systems. The

relative costs of elements and their availability indicates a current preference for S, Al, Si, Zn, P, Na, Cu, Mg, Ca. Fe, although plentiful and cheap, is most likely to be needed in the solid containment systems.

Metal or alloy heat storage by phase change appears to be feasible from 1219K to moderately low temperatures. Inorganic salts with comparable storage capabilities per unit mass or volume also are available, as shown in Table II, Appendix A, but the thermal conductivities are one to two orders of magnitude higher for the metallic storage materials than they are for the salts. Simpler and smaller heat exchangers should be possible with the metals than with the salts.

The theory of heats of eutectic transformation shows that the important contributions come from heats of fusion of the participating elements, possibly modified by their combinations in intermetallic compounds, and from the differences in the entropies of mixing of the relatively well-ordered solid phases and the eutectic liquid. Alloys were chosen for study, or sought where they were not previously known, in order to optimize the heat storage density. For a current tabulation see Appendix B. Although it is not possible to state that the best alloys have been found, reasonable assurance can be given that the reported

alloys are representative of good thermal storage behavior. They give the alloys a fair test in comparison with other storage materials.

It is important to consider one other cost factor which appears to favor the alloys. Even after prolonged use, they remain refined metallic materials that have other valuable uses. They retain much of their initial value. As a specific example, the Al-Si eutectic alloy has been widely used in cast automotive parts, including engine blocks. Although many other alloys are not in precisely the compositions that would be used in other applications, they could be adjusted by simple additions.

Volume Change During Transformation

To maintain efficient heat transfer from the PCM containment vessel to the heat transfer fluid or to a heated surface such as the receiver cavity of a solar receiver the solid or liquid PCM must always be in direct contact. Large volume change during transformation will require design complexity to insure that direct conducting paths are maintained. The large volume changes reported for halide eutectics, on the order of 20 to 25 percent of the total volume, were sufficient incentive to measure the

changes that occur for the metal eutectics.

An X-ray absorption method that is readily used with ductile samples is described in Appendix C. Its application is illustrated by measurements on pure aluminum and the Al-Cu and Al-Si eutectics that agree well with previously published values. Thermal expansion coefficients for the liquid and solid phases or mixtures of phases also are in reasonable agreement where published values are available for comparison.

Some refinements have been added to the method in Appendix D to simplify the selection of a useful X-ray wavelength and improve control of furnace temperature. The measurement of fractional volume change during eutectic transformation has been extended to two ternary systems, with work still progressing. Expansion coefficients have been measured again.

The alloy eutectics show volume changes of about 5 to 7 pct. for the aluminum alloys and near 3 pct. for a Cu-P-Zn eutectic. There is no reason to believe that these modest changes are atypical, so the operation of a PCM storage system should be simpler with these materials than with those that have much larger volume changes during transformation.

Modeling Heat Flow in Cylindrical Heat Exchangers Containing Phase-Change Materials

Appendix E describes the development of a numerical routine for calculating heat flow efficiently in a vessel of cylindrical symmetry containing a material capable of storing latent heat during a solid to liquid transformation, including the special case in which the solid is a mixture of phases. This paper was presented at the 3rd Miami International Conference on Alternative Energy Sources, December 15 to 18, 1980, and will appear in the proceedings of that conference to be issued by the Hemisphere Publishing Company. The utility of the procedure for dealing with metal and salt eutectic storage materials and the factors affecting their performances in simple heat exchangers is demonstrated in this work.

An improved procedure is outlined in Appendix F that has all of the capabilities of the earlier procedure but is capable of more precise calculation. Results have been collected with this procedure right up to the preparation of the report,with additional runs to be made. The paper is being prepared for the AIAA Thermophysics Conference, Palo Alto, Cal., to be held in June, 1981. The calculations show the advantages for the highly conducting alloys in giving faster storage and retrieval of heat for fixed geometry as compared with those materials that have lower thermal conductivities.

These limited applications have given assurance that the calculation techniques can be used in comparing alternative designs as well as competitive PCMs in establishing optimum system designs. Following demonstration of a proven containment procedure, heat exchanger designs consistent with the containment method and storage materials will be evaluated, leading to the choice of the optimum configurations for the various applications that seem reasonable for these combinations.

Containment

Recent studies that show the short term stability of silicon carbide in contact with molten storage alloys are described in Appendix G. Alloys rich in aluminum or copper, containing significant concentrations of silicon, magnesium and zinc have shown little tendency to attack silicon carbide, but an appreciable rate of attack on Type 304 stainless steel (19Cr, 9Ni). Although the exact properties of the containment materials that are desirable will be determined by the geometrical configuration selected, it seems likely that the structure will have to be fabricated from an alloy that combines good high temperature strength, good thermal conductivity, and reasonably good low temperature ductility. In addition, resistance to chemical attack by the heat storage materials must be provided without impairing these other properties.

One reasonable procedure would be to construct the system from a stainless steel or other oxidation resistant alloy, then coat surfaces that will be exposed to the heat storage alloy with silicon carbide. The coating would cause little loss in heat transfer and would provide a small increase in high temperature strength. If the surfaces exposed to air were also coated, somewhat lower grade alloys might be used, because silicon carbide should provide good oxidation resistance.

It is important to emphasize that this item is the last bit of undemonstrated technology needed to embark on a serious design. In particular, the stability of a carbide coated steel to many thermal storage and release cycles should be verified on a laboratory scale before the construction of a working system is undertaken. Several substrate alloys, differing in their thermal expansion properties, should be coated and tested before a final choice of containment material is made.

A more complete summary of Appendices E and F prepared by Michael Labdon follows.

INTRODUCTION

The thermal storage units depicted in Figures 1, 2, and 3 represent conceptual designs for use in the collection and transmission of energy concentrated from parabolic-dish solar receivers. Due to the high energy flux imposed on the inner cylinder, the ongoing investigation dealt with the contrasting of candidate phase-change materials (PCM's) for conducting the heat energy, as well as finding an appropriate material for PCM containment.

Due to the array of potential PCM candidates and the complicated geometries associated with the storage structure, an efficient and versatile numerical routine was required for analyzing their thermal behavior.

PROCEDURE

Method

An extensive literature search was initiated to determine if a solution method already existed which could be modified, or if an original routine needed to be developed. The result of the search was to utilize a complex method originally posited by Forster (1), Murray (2) and Lazaridis (3), which was subsequently demonstrated as workable by Farouk (4), and finally clarified by Harding (5) and Labdon (6) as to its inherent simplicity and efficiency.

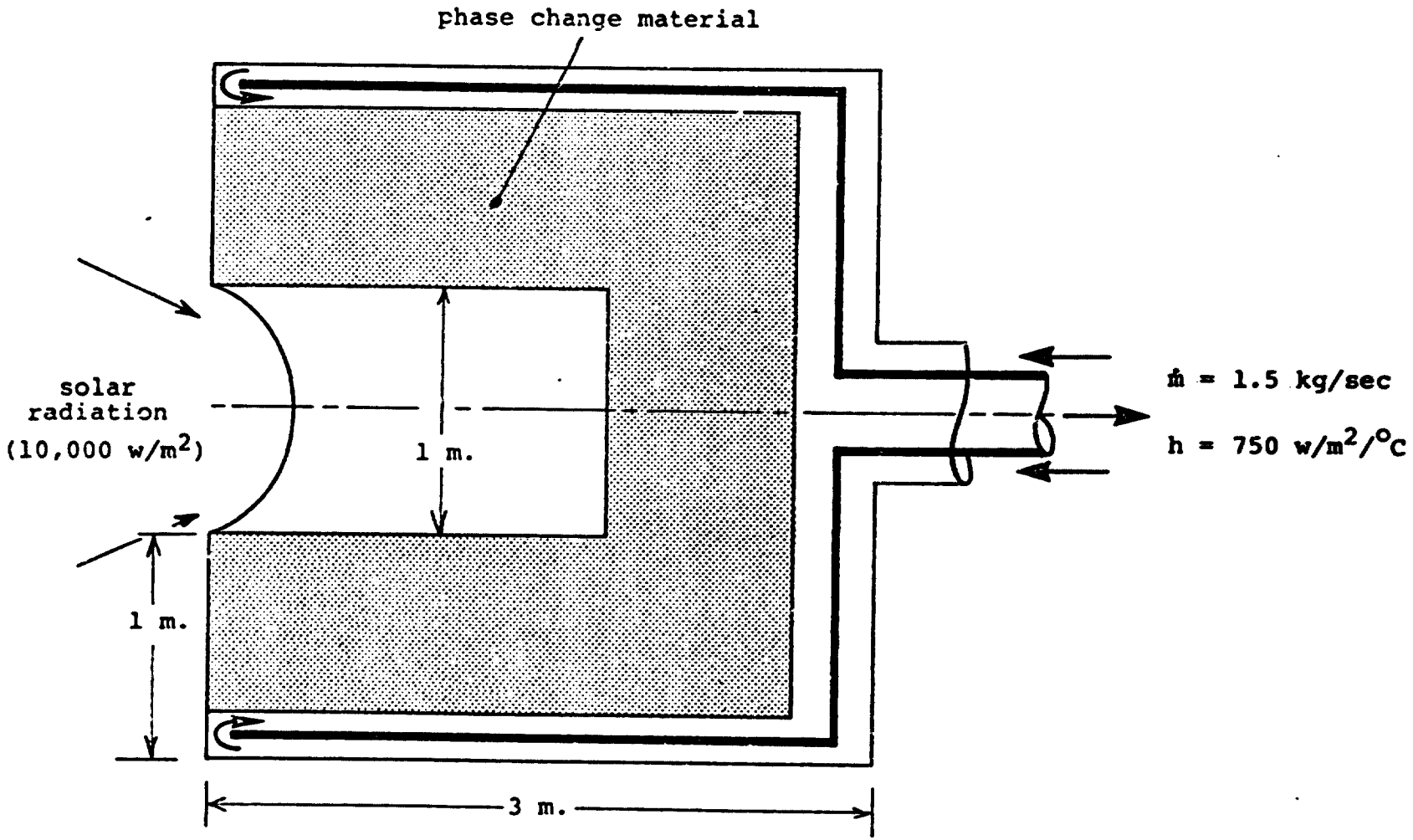

A solar receiver/thermal storage unit using phase change material

FIGURE 1

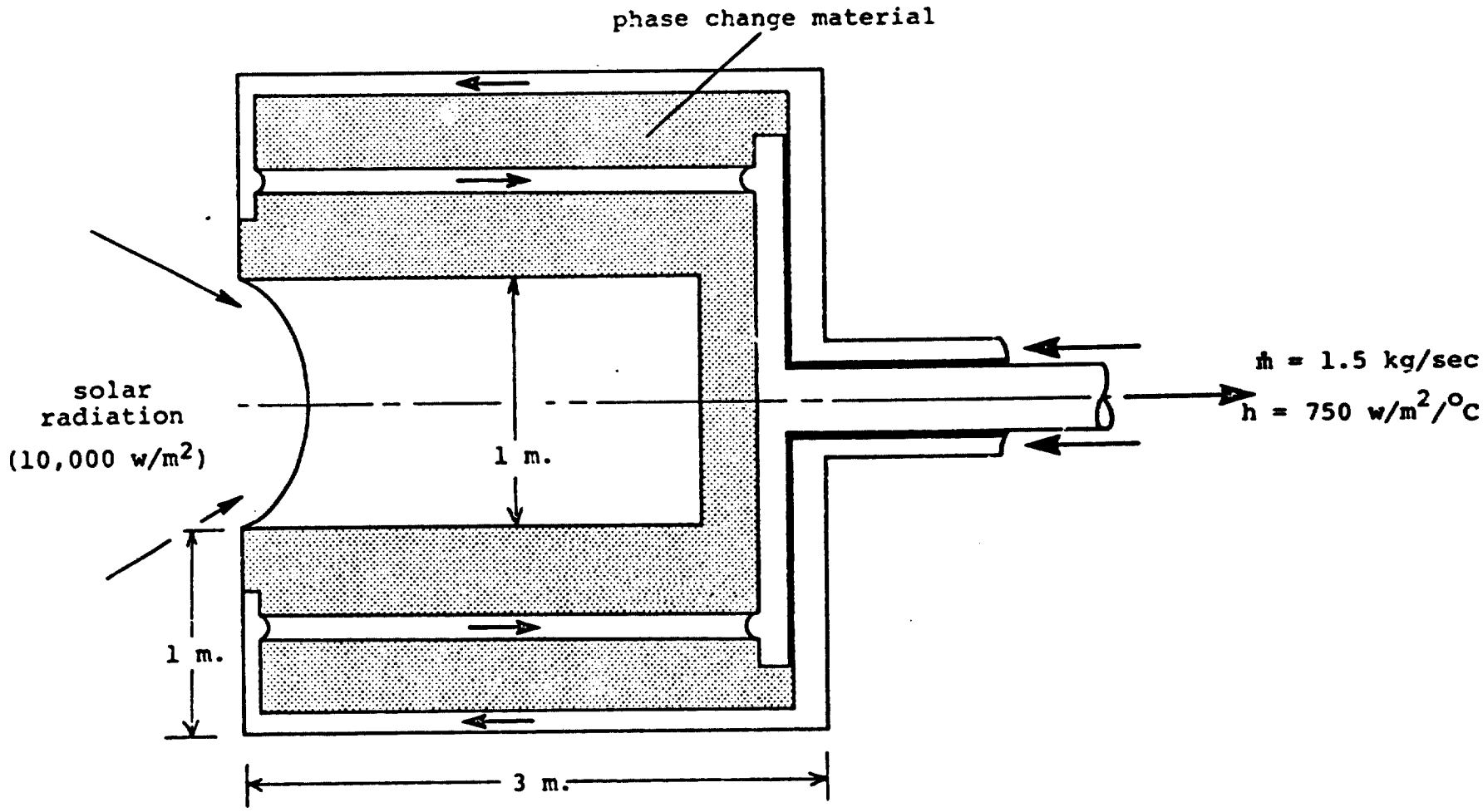

A solar receiver/thermal storage unit using phase change material

FIGURE 2

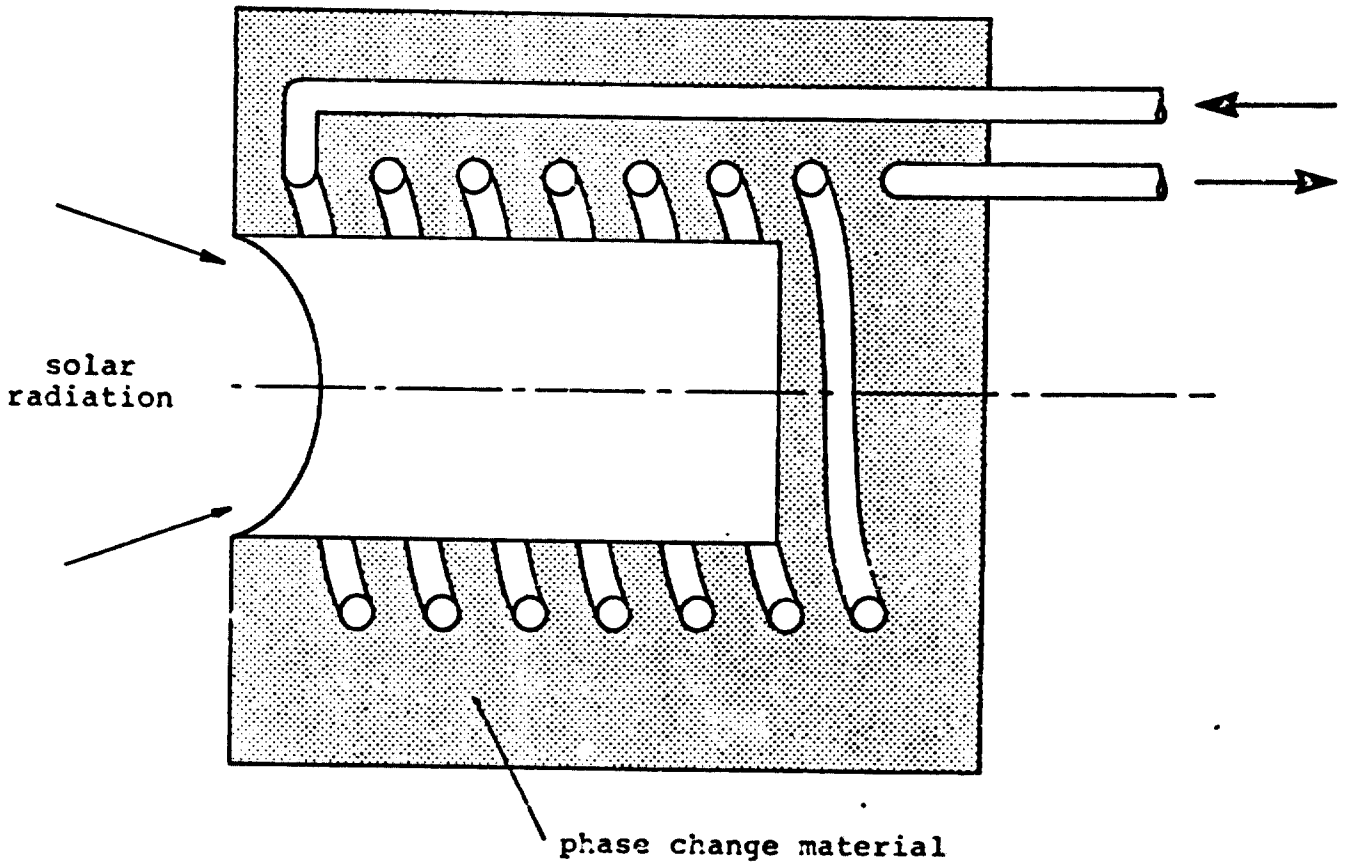

A solar receiver/thermal storage unit using phase change material

FIGURE 3

The versatility of the routine is reflected in the fact that time and spatial dependent boundary conditions, temperature-dependent properties and initial temperature distributions may be included,which represents the more realistic condition encountered with solar energy and storage systems. Outputs include prediction of melt-line locations, temperature histories and charging rates. The method models heat conduction within an annulus of phase-change material subjected to various boundary conditions, by overcoming the inherent difficulty of determining the temperature distributions around the melt-line (hence, its velocity) which is non-linear in nature. Essentially, finite-difference equations monitor the heat transfer in the regions away from the interface, while Taylor-series expansions of temperature are made near the fusion front so as to describe the temperature fields and thus couple the thermal behavior between the solid and liquid regions.

The mathematical derivations, assumptions and solution process of the numerical routine appear in two publications, Appendix E and Appendix F, where the latter models both the radial and axial heat conduction within the material. The various thermal properties of the candidate PCM's, and the assumptions used in facilitating the generation of results are listed on page 15, Appendix E.

Analysis of Storage Units

The solar receiver/storage units dimensioned in Figure 1-3 do not represent an attempt in design optimization, but merely provide a parity for the contrasting of any desirable phase-change materials, which in this case are metal alloys and salts.

Figure 1 was subjected to the simultaneous application of heat flux and convection on the inner and outer surfaces respectively, with the entire medium containing a 10°C initial superheat. In this manner, an evaluation of the PCM's can be made while the storage unit is in the actual working mode.

Figure 2 differs from that of Figure 1 by the cylindrical array of internal tubes which contain the heat-convecting medium. Only the discharging case will be modeled by assuming the entire medium is initially in a constant molten state. Six equally-spaced, 4 cm.diameter tubes are situated halfway between the inner and outer surfaces. Termination of the discharging case occurs when the radially-expanding melt-lines intersect each other and the unit's surfaces. The small amount of material left over is taken into account by forming an extra concentric ring around each tube.

The third storage unit, depicted in Figure 3, represents a more complicated configuration presently outside the scope of this work, but it is reasonable to expect that the contrasting performance between the salt and metal alloys would be similarly evident in this geometry as well.

RESULTS

Figures 4 through 9 represent output from the routine for the first solar receiver/storage unit (Figure 1). Figures 4, 5, 6 represent melt-line locations within the receiver for the salt, Al-Si, and Mg-Si data respectively. The melt-line contours actually represent a three-dimensional surface similar to a cone or trumpet-end. The more curved lines of the alloys represent the increased heat transfer within the upstream nodes due to the higher thermal conductivity. The smaller times required for melt-line penetration are also indicative of the alloys. Interface locations are shown only for the outer half of the unit due to the large computer process times required for output generation, and due to the fact that a steady-state operation is approached where the heat flux imposed on the inner cylinder equals the heat convected out, thus yielding a melt-line velocity nearing zero.

Figures 7 and 8 describe the heat flux boundary surface temperatures for equal time increments. Both show the steady-state temperature distribution being approached, as well as the much higher surface temperatures associated with the use of the salt PCM; attributable again to the low thermal conductivity. Figure 8 indicates the effect of increased melt-line penetration on the "cooling" or surface temperature reduction of the unit, typical of metal alloys.

A measure of the effectiveness of this type of heat exchanger is gleaned from the charging rates shown in Figure 9. The area under the curves represents the amount of energy transferred within a certain amount of time, and as can be seen, the metal alloys are more efficient in storing and transferring the collected energy.

As a further display of the versatility of this routine, the discharging rate of Figure 2 was determined by the amount of energy transferred from the six tubes, and contrasted to that obtained from the discharging case of Figure 1 (when the heat flux was terminated), the results of which appear in Figure 10. This indicates the role the method plays in design optimization of the receiver/ storage units, by showing the increased discharging rates associated with installing the convection tubes within the PCM, as opposed to a sheet surrounding the entire medium.

FIGURE 4

Melt-line locations at six different times (min.) within the outer half of the storage unit, for the salt phase-change material.

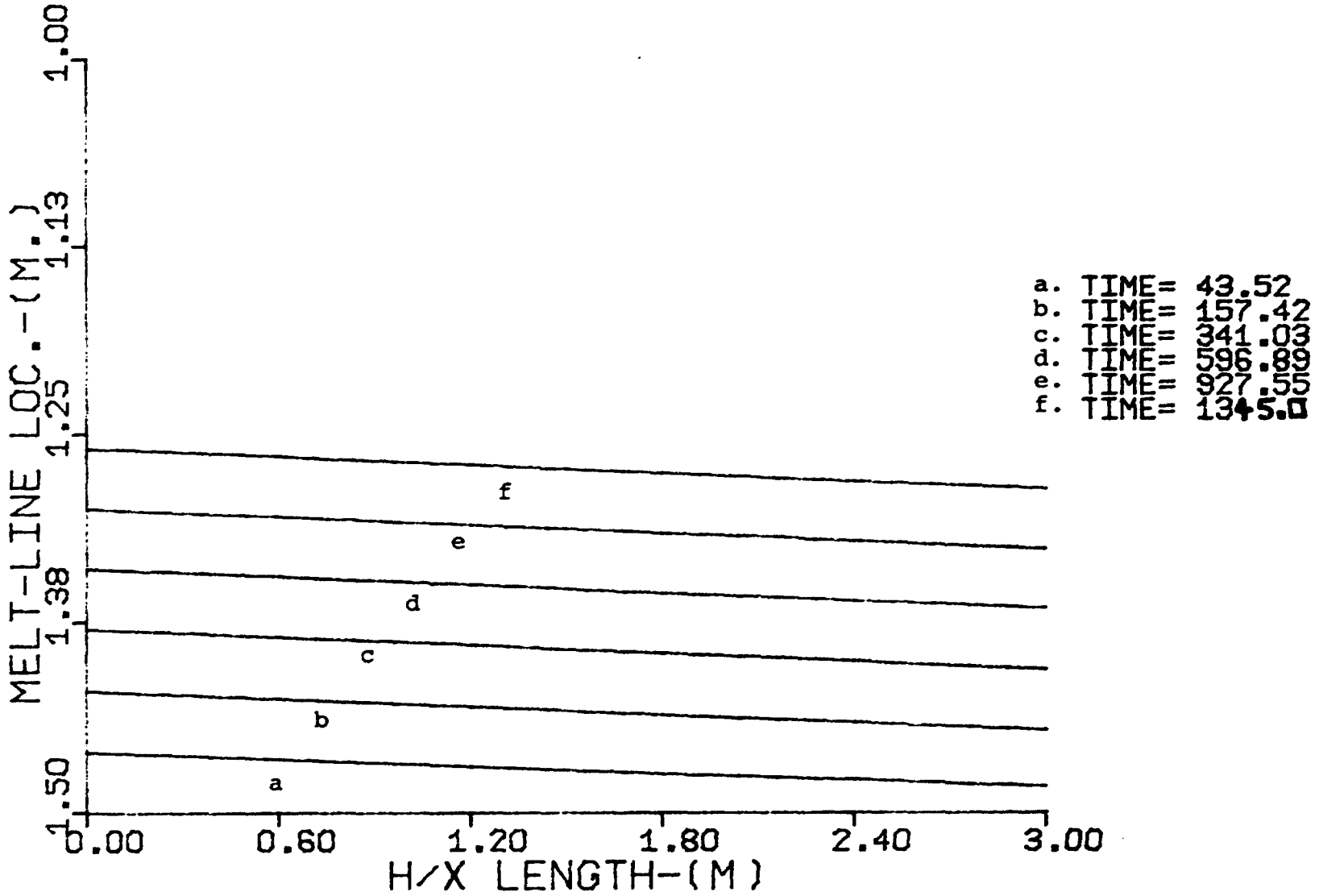

FIGURE 5

Melt-line locations at various times (min.) within the outer half of the storage unit, for the metal alloy Al-Si.

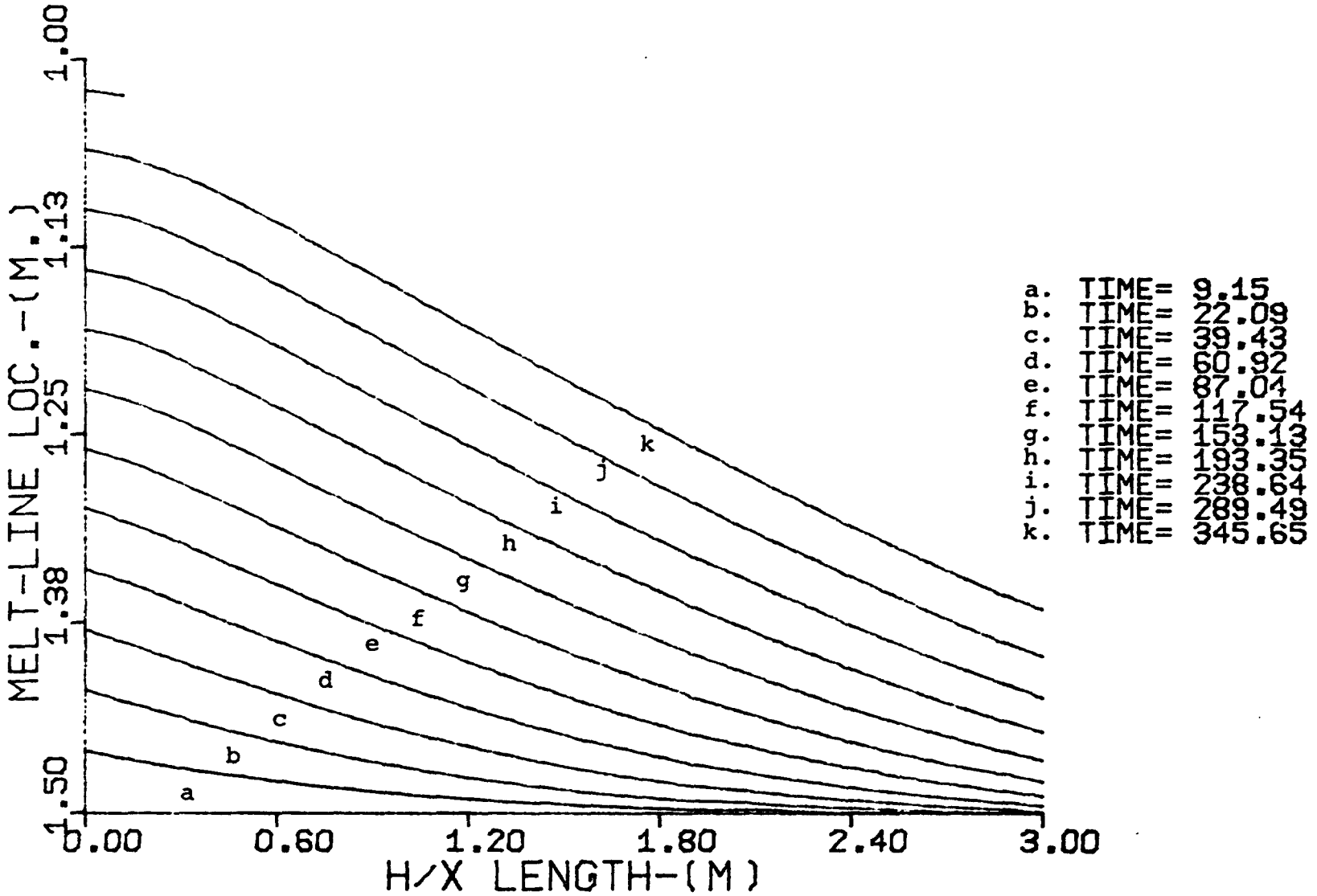

FIGURE 6

Melt-line locations at eight different times (min.) within the outer half of the storage unit, for the metal alloy Mg-Si.

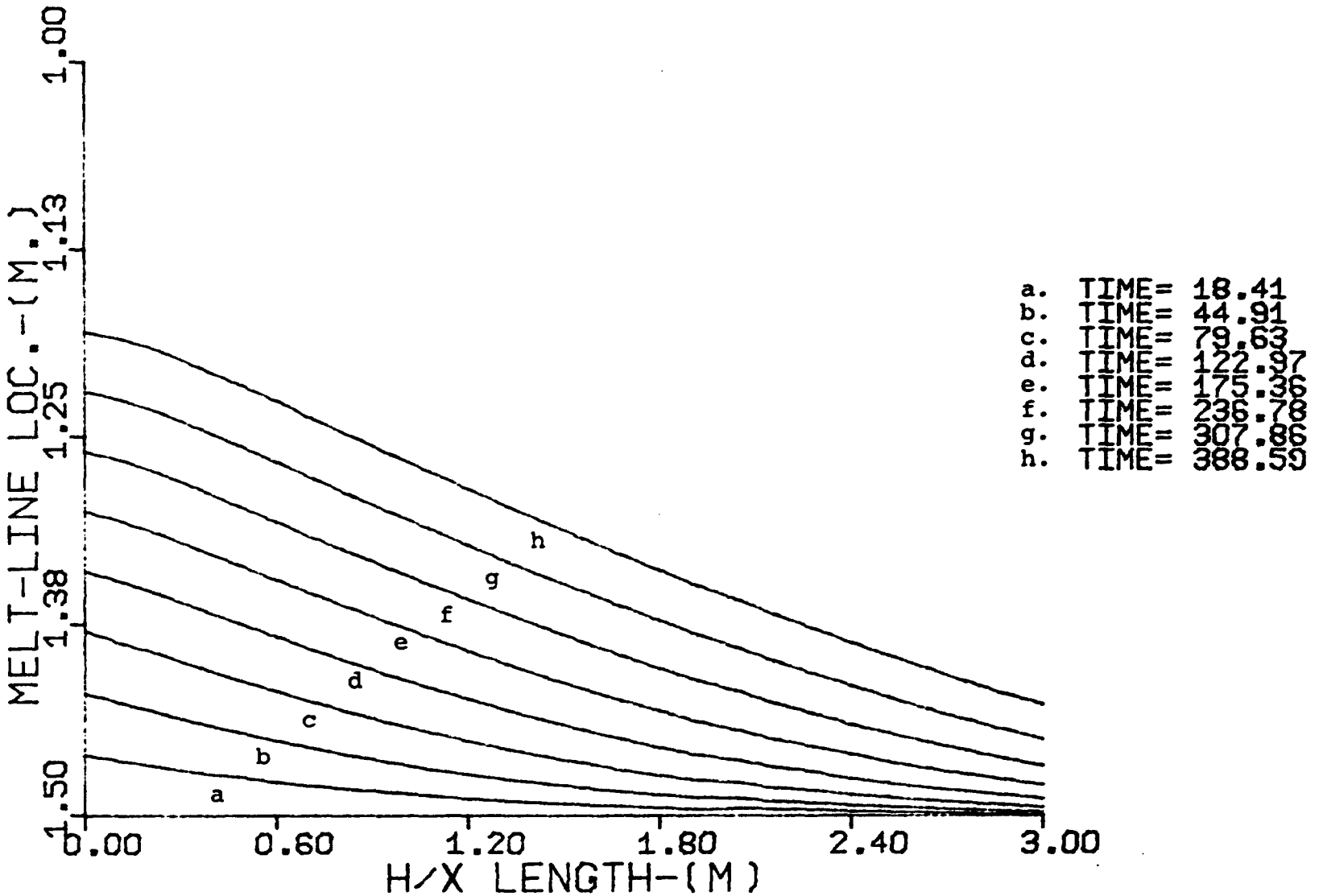

FIGURE 7

Heat flux (inner) surface temperature for the storage unit at various times (min.) using the salt phase-change material.

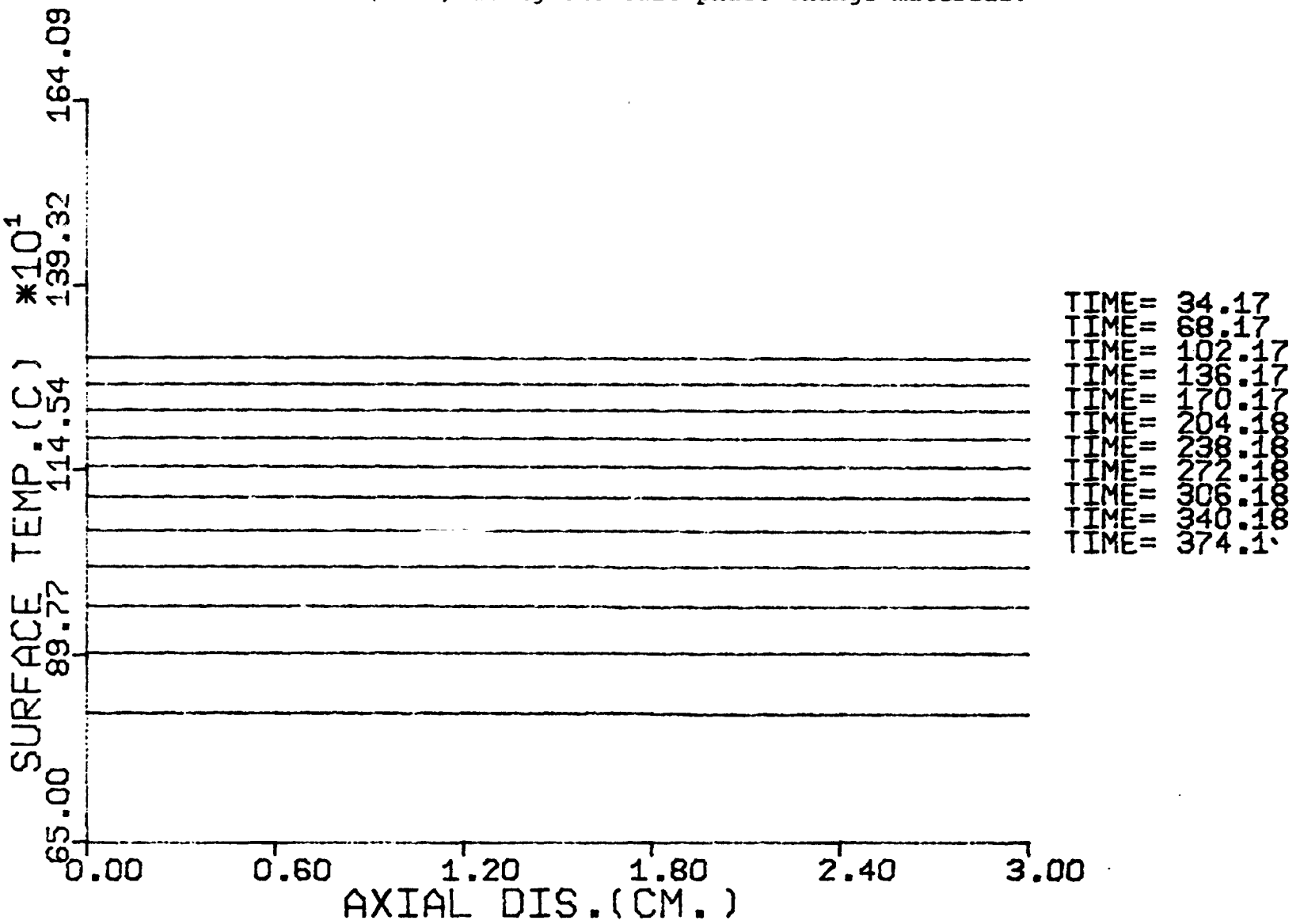

FIGURE 8

Heat flux (inner) surface temperature for the storage unit at various times (min.) using the metal alloy, Al-Si.

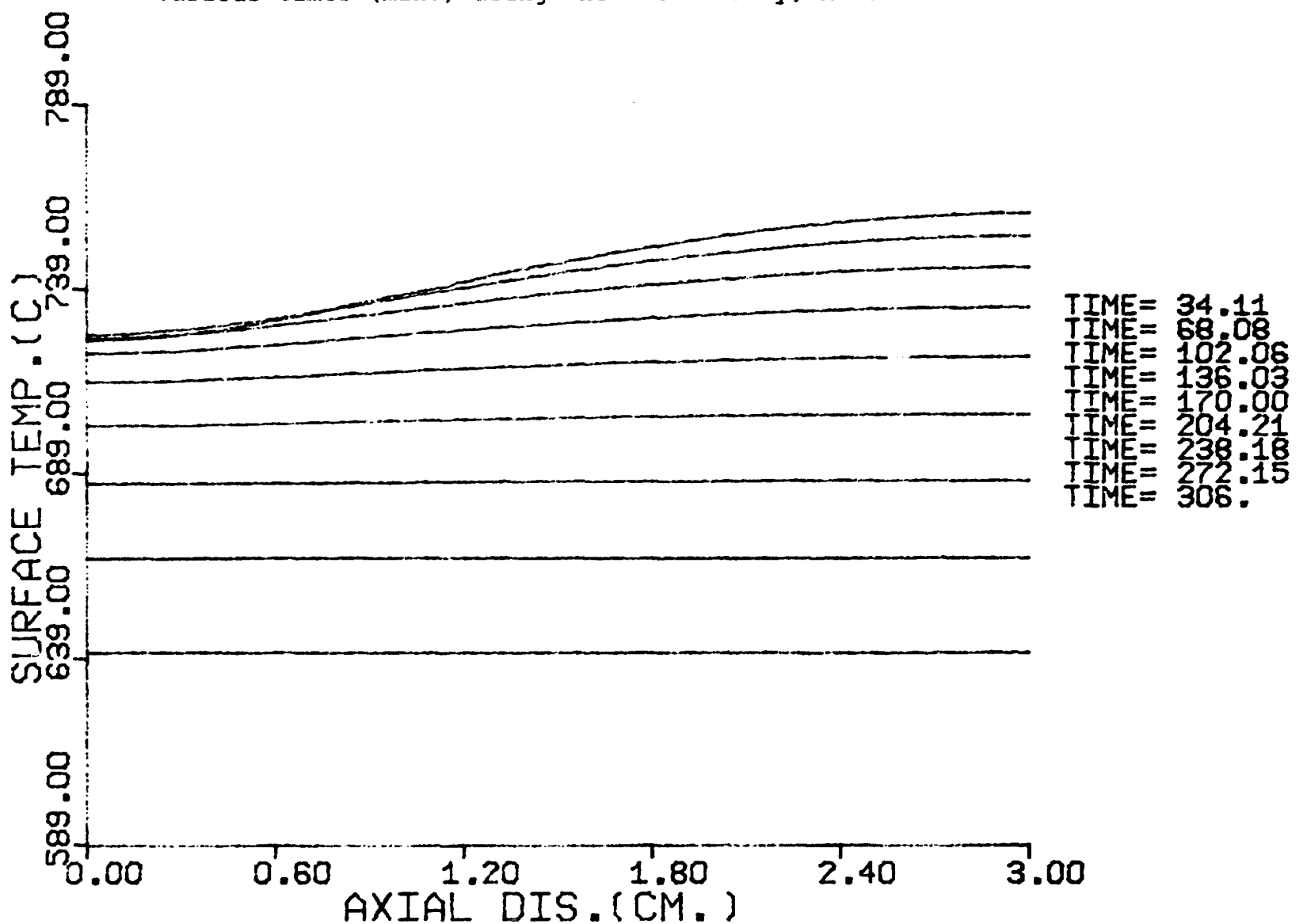

FIGURE 9

Non-dimensionalized, instantaneous discharging rates of the first receiver/storage unit, for the three candidate phase-change materials.

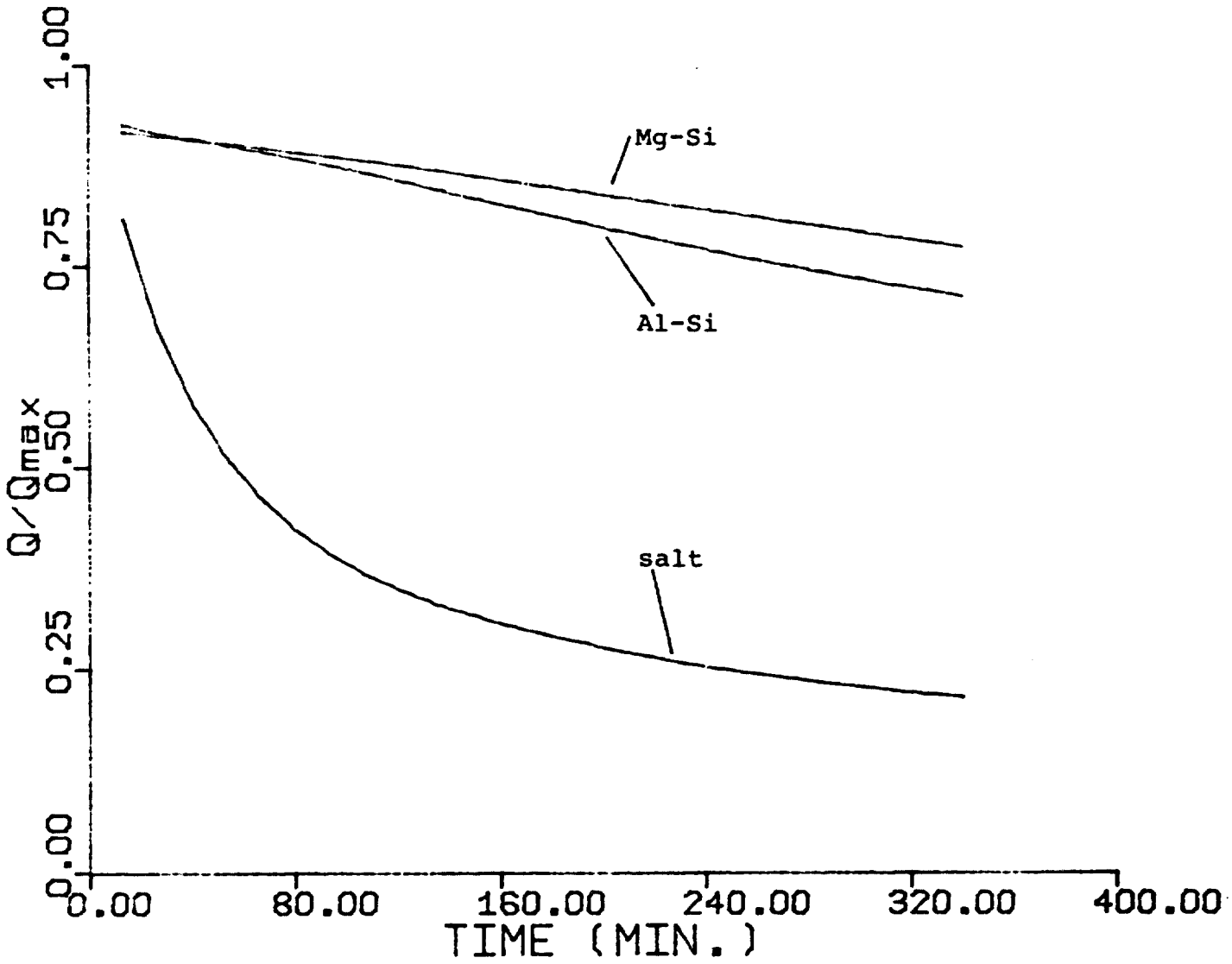

FIGURE 10

Non-dimensionalized, instantaneous discharging rates of the first and second storage units, for the salt PCM.

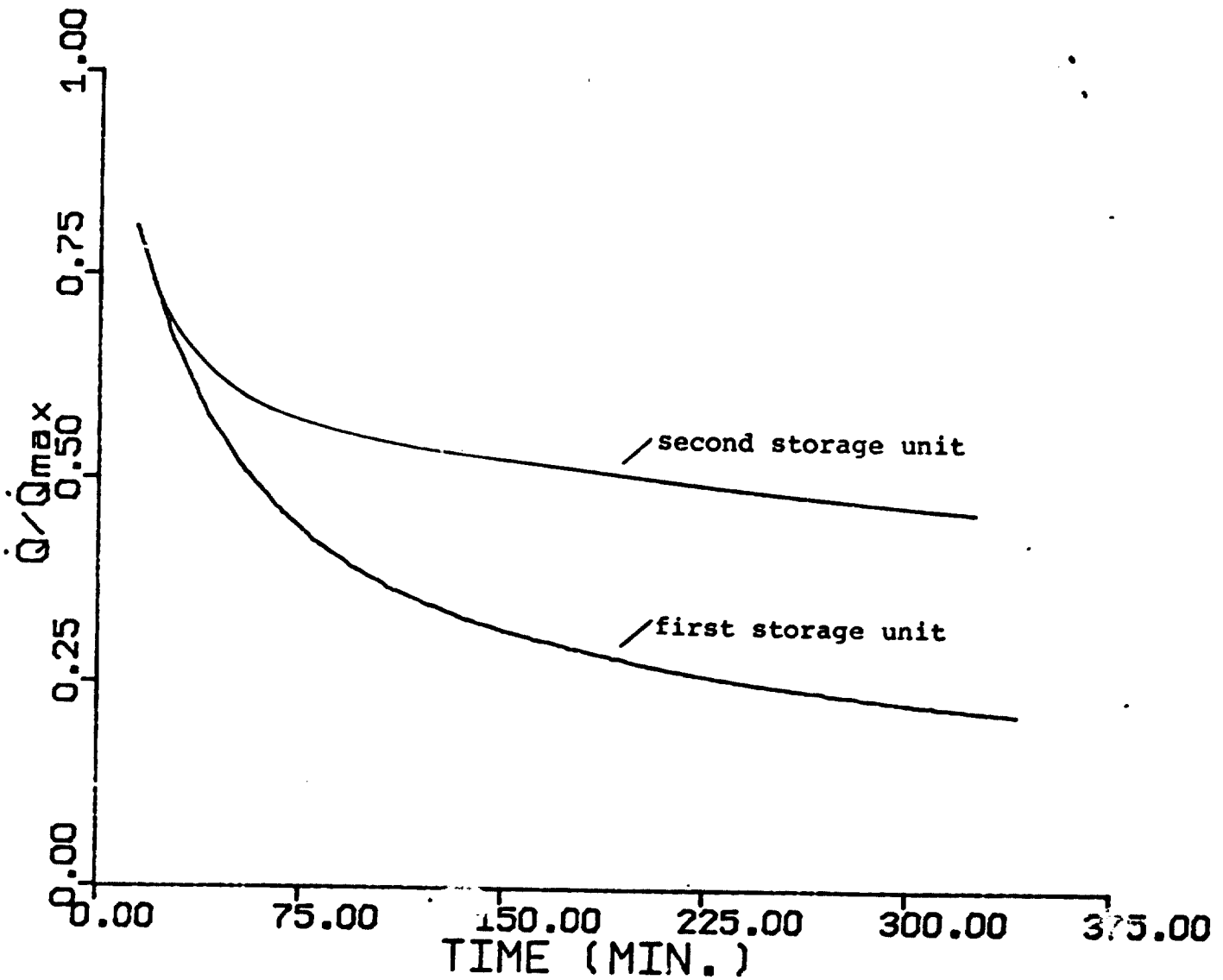

REFERENCES

1. C. A. Forster, "Finite-Difference Approach to Some Heat Conduction Problems Involving Change of State," Report of the English Electric Company, Luton, England 1954.

2. W. D. Murray and F. Landis, "Numerical and Machine Solutions of Transient Heat-Conduction Problems Involving Melting or Freezing," Trans. Am. Soc. Mech. Eng. 81, 106 (1959)

3. A. Lazaridis, "A Numerical Solution of the Multidimensional Solidification (or Melting) Problem," Int. Journ. Heat Mass Transfer, 13, 1459 (1970).

4. B. Farouk and S. I. Guceri, "Trombe-Michel Wall Using Phase-Change Materials," Second Miami International Conference on Alternative Energy Sources, December 1979.

5. A. Harding, Ph.D. Dissertation, University of Delaware, 1981.

6. M. B. Labdon, Master's Thesis, University of Delaware, January, 1981.

APPENDIX A Remover
REPRINT
NASA Support

APPENDIX A

APPENDIX B

New Autectic Alloys and Their Heats of Transformation

DIANA FARKAS AND C. E. BIRCHENALL

Diana Farkas is a graduate student and C. E. Birchenall is Distinguished Professor of Metallurgy, Department of Chemical Engineering, University of Delaware, Newark, DE 19711

ABSTRACT

Eutectic alloys and intermetallic compounds of the common elements, Al, Ca, Cu, Mg, P, Si, Zn, may be useful for high temperature heat storage. A number of binary and ternary eutectic alloys have already been studied and their heats of fusion measured. In this work heats of fusion, and in some cases heat capacities, of new multicomponent eutectics and intermetallic phases are reported. Some of the alloys investigated are competitive with molten salts for heat storage density at high temperatures.

A method to determine unknown eutectic compositions was developed, based on combined results of differential thermal analysis with metallography and microprobe analysis. A new differential thermal analyzer, which gave satisfactory accuracy for qualitative measurements, was built to handle the relatively large samples that are required for this procedure. The method allows determination of eutectic composition in no more than three steps.

The heats of fusion of the resulting alloys were measured using commercial calorimeters, a differential thermal analyzer and a differential scanning calorimeter. The possibility of measuring heat capacities by differential thermal analysis was also examined.

INTRODUCTION

There are various ways in which heat storage can reduce costs and make more efficient use of power generating equipment. A thermal storage unit would eliminate the difference between peak and off-peak hours, storing heat when demand is less than the generating capacity and returning it as needed. The generator could be designed for the average, instead of the maximum, power requirement. A central storage system could thus reduce the cost of building and operating a power generating plant.

An efficient way to store heat is to use phase transformations that take place at a definite temperature. The storage density depends upon the latent heat of transformation, which is the entropy change times the transformation temperature. This entropy change is small for solid-solid transformations but much larger in melting. For solid-gas transformations, advantages of the still larger entropy change are offset by the practical problems in handling the large volume of gases.

The first materials considered for high temperature heat storage were inorganic salts. Fluoride eutectics were studied by Schroeder (1). Lithium compounds and eutectics were characterized by Tye et al. (2). Further study in molten salts was carried out by Ferrara et al. (3),

by Haru et al. (4), and by Clayton (5). Some of the problems found in molten salts were:

i) They have low thermal conductivity, leading to large irreversible losses and requiring a very large surface to volume ratio.

ii) They are highly corrosive and must be dried very carefully, even if expensive, corrosion-resistant containers are used.

iii) They have large volume changes during melting, around 20%.

iv) Lithium and fluoride compounds, those with the best heat storage densities, are relatively expensive materials.

Metals diminish these problems, and therefore might be strongly competitive even if they have somewhat lower storage densities. Materials were selected in the range of 300 to 1000°C, on the basis of cost and availability, as well as storage density (6). The heats of fusion of many binary and ternary eutectics were calculated approximately (7), and the most promising of these were measured (8).

In choosing particular eutectics, calculations were done for the heats of fusion using two different ideal solution models as well as a regular solution model.

These calculations are discussed below. The results are only approximate, but it was possible to identify qualitatively the contributions to the heat of fusion in order of importance.

i) Heats of fusion of the constituent elements.

ii) Heat of formation of intermetallic compounds present.

iii) Difference in entropies of mixing between solid and liquid phases.

Analysis of the results obtained by Riechman shows that alloys have the best observed heat storage densities in the range from 700°K to 850°K. Better alloys are sought in the region 900°K to 1000°K and below 700°K by further alloying. Therefore, it is necessary to determine the congruently melting compositions in multicomponent systems and evaluate the heats of fusion.

Ternary phase diagrams are not generally known, and few thermal data are available. In some cases the formation of ternary intermetallic compounds is reported. With this lack of information any theoretical approach to the problem is a crude approximation. Nevertheless, such an approach can be the useful starting point of a trial-and-error method for experimental determination.

Although it is clear that alloys will be used primarily as latent heat storage systems and only incidentally for sensible storage, it is important to know their heat capacities as well. Complete information is needed to analyze the possible heat storage systems and develop practical design.

CALCULATION OF EUTECTIC COMPOSITIONS AND TEMPERATURES

For the ideal solution model all calculations are simple, and no thermal data are needed except heats of fusion of the components. For the regular solution case, the binary equations have been extended to ternary systems, an approximation that allows calculation of ternary free energies from binary data. This was first done by Darken (9) in 1950 and developed further by Toop (10). The derivation is very well presented by Richardson (11).

An alternative but equivalent treatment is given by Olson and Toop (12). This approximation has been used successfully in the calculation of phase diagrams with no ternary intermetallic compounds, for example, the Ni-Cu-Cr system by Meijering (13). Tne limitations of the method were analyzed by Olson and Toop (14). In cases where compound formation is suspected, they concluded that the regular solution model does not yield useful results.

In addition to these two equations, a polynomial approach has been used. This Guggenheim-type equation has been generalized by Hillert (15).

The three approaches were compared by Ansara et al. (16) for the determination of phase boundaries. In the systems Fe-Cr-V and Cd-Bi-Sb it was found that the results derived from these three equations did not differ much. In

cases where compounds are formed or where there is a strong ordering in the liquid these approaches are not expected to be useful, especially the first two models that assume regular solution throughout the system. The advantage of these models is that they are based on binary data and no ternary measurements are needed.

In this work both ideal and regular solution models were applied and the results compared. Clausius-Clapeyron equations, one for each component phase, and the condition that all the fractional compositions sum to unity yields n + 1 equations in n unknown compositions and the temperature. This set of non-linear equations was solved by computer fitting. The predicted eutectic temperatures for some alloy systems are shown in Table 1.

A regular solution model applied on the basis of pure components will not give adequate results if intermetallic compounds are present in the system. For this reason the same approximation was used taking the constituent solid phases as the components of the system. Thermal data for the calculations were taken from Hultgren et al. (17), except in the Mg-Si case (18), where activities are always given with the pure elements as standard states. These reference states were changed to be the pure intermediate phases. The eutectic points predicted by this model are also shown in Table 1.

Table 1. Calculation of Eutectic Compositions and Temperatures

System	Ideal Model		Regular Model		Experimental	
Al-Cu	15% Cu	654°K	17% Cu	790°K	17% Cu	821°K
Al-Mg	36% Mg	555°K	40% Mg	676°K	37% Mg	724°K
Al-Si	0% Si	--	7% Si	834°K	12% Si	850°K
Mg-Si	52% Mg	1183°K	53% Mg	1289°K	48% Mg	1219°K
Mg-Zn	32% Zn	592°K	33% Zn	655°K	29% Zn	615°K
Mg-Al-Cu	10% Mg 18% Cu	546°K	11% Mg 17% Cu	541°K	8% Mg 17%Mg	797°K

CALCULATION OF THE HEATS OF FUSION

For eutectic melting the ideal solution model can be applied to the prediction of heats of fusion using either the participating elements or the constituent phases as components. The two approaches yield different results. Both assume complete ordering in the solid with different ordering in the liquid. Random mixing of elements is likely to be better for disordered liquids and random mixing of phases for partially ordered liquids.

Regular solution equations for eutectics (19) permit calculation of the latent heat either from the entropy change or from the enthalpy change, assuming random mixing in the liquid. If the solutions are truly regular and the data are correct, both equations should be equivalent.

Table 2 is a comparison between the described theoretical methods and experimental results. It appears that the ideal mixing calculation from the participating phases often is the best choice for accuracy and simplicity. The calculations by all methods tend to overestimate the heat of fusion, and they should be taken as an upper bound to the true value.

Table 2. Calculation of Heats of Fusion

Alloy	T(°K)	ΔH_f (cal/gr)				
		Ideal 1*	Ideal 2*	Regular 1*	Regular 2*	Measured
Al-Cu	821	106.3		86	91	83.8
Al-Si	852	136.5	136.5			123.1
Al-Cu-Si	797	134.0	97.8			101
Al-Mg-Si	833		137.1	131	107	130.3
Al-Mg-Zn	720		95.9			74
Al-Mg	724		89.6	109	114	74.1
Mg-Cu-Zn	725	97.5				60.5
Mg-Zn	615		55	59	111	40
Al-Mg-Cu	779		89.7	97	96	86.1
Mg-Ca	790	102.8				63.1
Mg-Si	1253	300	256			185

* In column 1 the pure elements are taken as components; in column 2 the participating phases are taken as components.

EXPERIMENTAL DETERMINATION OF EUTECTIC COMPOSITIONS

An experimental method for finding and characterizing eutectics was needed that would work with no information at all on the system but would be able to use known information to converge faster. The combined results of DTA, electron microprobe and metallography provide such a trial-and-error method. Any theoretical approximation or empirical data can be used to improve the initial guess of eutectic composition.

A sample of an arbitrary or guessed starting composition is prepared, and the melting behavior is determined by DTA. Metallographic inspection of the alloy is done optically and in a scanning electron microscope (SEM). The observed phases are correlated with the DTA results. The sample is searched for a small eutectic region, and the composition of any small zone suspected of being a eutectic mixture is analyzed quantitatively by SEM with an energy dispersive analyzer for the emitted x-rays (EDAX). If some doubt remains about the number or identity of the phases present, x-ray diffraction measurements are made.

If there is a eutectic region with a melting temperature in a desirable range, a new sample is prepared with the composition obtained by EDAX on the previous sample. The procedure is repeated until an alloy that is completely eutectic is obtained. When an intermetallic compound is

found in the process, it is also studied, especially in higher order systems where the probability of finding a desirable eutectic is lower.

In order to be sure that the observed DTA peaks correspond to the observed phases and the compositions measured, it is necessary to work with the three techniques on the same sample. In this case inhomogeneities in the alloy are not a serious problem.

Commercial calorimeters work with very small samples in order to minimize the errors in quantitative measurements. A DTA apparatus that will give good qualitative measurements with a large sample is diagrammed in Fig. 1. Temperature was varied under control of a programmer. The differential temperature was amplified and plotted directly against sample temperature on an XY recorder.

FIGURE 1. LARGE-SAMPLE DTA

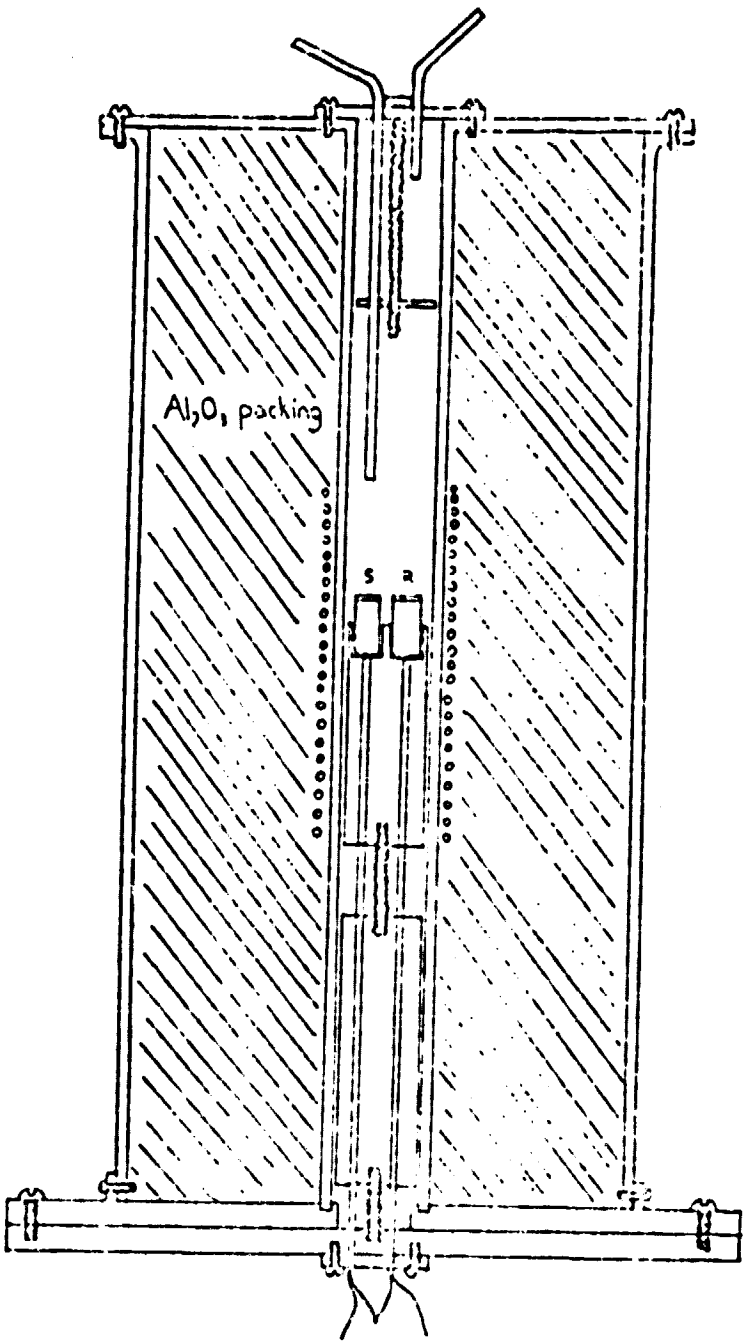

PREPARATION OF ALLOYS

The first alloys were made in a resistance furnace following the procedures of Riechman (8,19). However, when the starting materials differed greatly in melting temperatures, vapor losses could not be avoided, even with a collar on the stirrer shaft closely fitted to the crucible.

Owing to the repeated failure to prepare the alloys in which the starting materials have large differences in melting temperatures, an induction furnace was assembled. The relatively low frequency (50 kHz) of the mercury spark gap resonator provided vigorous internal stirring to the melt.

The starting materials were introduced into alumina crucibles that were then sealed by an alumina disc of the same diameter cemented with Sauereisen cement No. 78. In the cases where most of the starting materials were semiconductors, graphite crucibles were used, sealing them in the same way. The crucible was placed in a mullite tube, with a thermocouple touching it from the bottom and argon flowing in from the top. This setup was entirely successful in preventing vapor losses and providing good stirring to the melt.

MEASUREMENT OF HEATS OF FUSION AND HEAT CAPACITIES

Two commercial instruments were used for the measurement of heats of fusion, the Perkin Elmer DSC-II and the Du Pont 990 DTA. The former gave better precision, about 3%, and was used for alloys with melting points below 700°C. The Du Pont 990 DTA with its high temperature cell gave measurements with 5% accuracy for temperatures above 700°C.

For alloys with melting temperatures below 700°C the measurement of heat capacities can be carried out by DSC with a 10% accuracy. Manufacturers of commercial DTA instruments for measurements at higher temperatures do not claim sufficient baseline control for heat capacity determination. However, the Du Pont 990 DTA was tested for measuring heat capacities because of its improved electronic control of the baseline. Twelve baselines were analyzed, and it was found that they were straight within 10%. To check reproducibility several runs were made with the same sample pan that was opened and repositioned in the furnace between runs.

After two successful calibrations with sapphire, measurements on Al and Ag gave results shown in Table 3. For Al the agreement with tabulated data is very good. For Ag agreement is not as good, because its heat capacity

Table 3

Heat Capacity of Al and Ag

Measured with DTA 1200°C Cell

T(C°)	c_p(meas) (cal/g)	c_p(tabulated) (cal/g)
Aluminum		
550	.26	.28
580	.26	.28
600	.26	.28
630	.27	.29
650	.29	.29
(liq)710	.36	
Silver		
800	.12	.07
850	.10	.07
900	.15	.07
930	.25	.07
(liq)1000	.5	- -

taken at higher temperatures, is much lower. At lower temperatures the agreement improves.

Measurements were also attempted for the Mg-Si, Cu-Si and Mg-Cu-Si eutectics. At high temperatures, the values obtained are too low. In some cases the solid and liquid baselines crossed, owing to the evaporation of the volatile elements.

It appears that the specific heat values from DTA for non-volatile alloys are reliable within about 20%, but the values for volatile alloys cannot be trusted.

RESULTS

New Eutectics and Intermetallic Compounds

A search for new eutectics and intermetallic compounds was conducted in several ternary systems and two quaternaries. The search method converges in three steps, in two cases to negative results. The diagram in Table 4 summarizes the results step by step. X-ray data on the new compounds found are reported separately (20), together with several interesting microstructures.

Measurement of Heats of Transformation

Heats of eutectic transformation were measured in the Perkin Elmer DCS II when the melting temperature was lower than 700°C. For higher temperatures the Du Pont DTA model 990 was used with its high temperature cell.

Several known eutectics were characterized. Two of the previously measured eutectics (19) were repeated, Mg-Zn because the previous result was believed to be too low, and Mg-Si for further check. For Mg-Zn a higher value was obtained, and for Mg-Si excellent agreement was found with the previous measurement. The results for the known alloys are listed in Table 5, together with those newly determined. Table 5 also includes the measurements of heat capacities for the alloys that are interesting as heat storage materials. The room temperature densities used in calculating

Table 4.

Steps in the Search for New Eutectics and Intermetallic Compounds

System	Alloy No. 1		Alloy No. 2		Alloy No. 3	
	Microstructure	Thermogram	Microstructure	Thermogram	Microstructure	Thermogram
Mg-Si-Cu	$Mg_6Si_7Cu_{16}$+ segregated Mg_2Cu	2 peaks	$Mg_6S_{17}Cu_{16}$+ eutectic	2 peaks	ternary eutectic: $Mg_6Si_7Cu_{16}$, Mg_2Si,Si	1 peak 770°C
Mg-Cu-Ca	ternary eutectic + segregated Mg_2Cu	1 peak 453°, bump after the	ternary eutectic: Mg_2Ca, Mg, ternary comp.	1 peak 445°C		
Mg-Si-Zn	MgSi eut.+ Zn 3% Mg eutectic	1 broad peak 800°C	Mg-Si eut. +Zn 3% eut.	1 broad peak 850°C	Mg-Si eut. + Zn	1 broad peak 900°C
P-Cu-Zn	eutectic: β brass, Cu_3P, terndry comp.	1 peak 720°C				
P-Cu-Si	1 homogeneous phase	1 peak 840°C				
Cu-Si-Zn	ternary compound + ternary eutectic	2 peaks	ternary eutectic: Cu_4Si, ternary comp, other phase?	1 peak 765°C		
Mg-Si-Ca	$CaSi_2$ + Si + Ca_2MgSi_3	2 peaks	$CaSi_2$ + Si + Ca_2MgSi_3	2 peaks	Mg_2Si + Si + Ca_2MgSi_3	1 peak 865°C
Al-Cu-Mg -Si	Al_2Cu + Si + Mg_2Si + quat. comp.	4 peaks	Al_2Cu + Si + Mg_2Si + quat comp.	4 peaks		
Al-Cu-Mg -Zn	2 quat. comp. + quat. eutectic	2 peaks	eutectic: 2 quat.comp., Al, other phase	1 peak 520°C		
Al-Mg-Si -Zn	Al-Mg-Zn eut. + Mg_2Si + Si	2 peaks	Al-Mg-Zn eut. +Mg_2Si+Si	2 peaks		

Table 5. Summary of Heat of Fusion Measurements

System	Composition (Wt%)	Temperature (°C)	ΔH_f (cal/g)	Density (g/cm^3)	ΔH_f (cal/cm^3)	Cp (cal/g°C)
Mg-Zn	52% Zn	340	43	--	--	
$MgZn_2$	--	588	55	--	--	
Mg-Si*	56% Si	946	181	1.90	343	0.19 solid
Cu-Si*	20% Si	803	47	6.60	310	0.12 solid
Mg-Ca	16% Ca	790	65	1.38	90	
Mg_2Cu	--	841	58	--	--	
Cu-P	9% P	715	32	5.60	179	
Al-Cu-Si*	30%Cu 5%Si	571	101	2.73	276	0.31 solid 0.29 liquid
Mg-Cu-Zn LT	25%Cu 15%Zn	452	61	2.80	171	
Mg-Cu-Zn HT*	45%Cu 6%Mg	705	42	8.67	364	0.10 solid
Al-Mg-Zn*	35%Mg 6%Zn	443	74	2.38	176	0.39 solid 0.35 liquid
Ca-Mg-Zn	28%Ca 17%Zn	400	35	2.26	79	
Cu-Mg-Si*	27%Si 17%Mg	770	101	4.15	419	0.18 solid
Mg-Cu-Ca	25%Cu 15%Ca	453	44	2.00	88	
Mg-Si-Zn HT	38%Si 15%Zn	800	75	--	--	
P-Cu-Zn*	17%Zn 14%P	720	88	7.00	616	0.13 solid
P-Cu-Si	10%P 7%Si	840	22	6.88	151	
Cu-Si-Zn	19%Zn 7%Si	765	30	7.17	215	
Mg-Si-Ca	30%Mg 21%Ca	865	73	2.25	164	
Al-Cu-Mg-Zn*	22%Cu 18%Mg 6%Zn	520	73	3.14	229	0.36 solid 0.27 liquid

* Best alloys for heat storage purposes.

the volumetric storage densities were measured with a pycnometer bottle.

DISCUSSION

The search method exceeded expectations by converging in three steps in the most complicated case. SEM metallography was used in almost all cases. Even with electron microscopy it was not possible to distinguish easily all the phases present. In a number of systems the phases had to be recognized either by composition or X-ray diffraction measurements. Eutectic mixtures also were difficult to recognize; lamellar morphologies seldom occurred. In addition to metallography, comparison of the overall composition to that of the fine, clearly eutectic region was helpful. Size of the phases was not by itself an adequate criterion. Extreme cases were found. Mg-Cu-Ca had such a small eutectic spacing that X-ray diffraction studies were necessary to determine whether there was a eutectic or a single intermetallic compound. Several cases exhibited widely varied spacings in different regions of the sample, probably as a consequence of different freezing rates.

Compositions by EDAX can be measured within 3% absolute error. The most serious limitation of the EDAX measurement is its spatial resolution. If a small particle of a phase to be analyzed is embedded in a different matrix, the penetration of the beam at the

lowest possible voltage in some cases excites the matrix elements beneath the particle. Also it is impossible to get precise composition values for the different phases that constitute an eutectic if the spacing is small.

The performance of the DTA for large samples was entirely adequate for qualitative measurements. A 30°C difference between the measured and actual transition temperatures was found consistently for all the runs owing to the thermocouple position. However, the interpretation of the DTA results for multicomponent alloys was not always clear. For example, in the Al-Cu-Si-Mg case four peaks were obtained, one peak corresponding to each of the intermetallic compounds present in the microstructure. The temperatures of these peaks did not correspond to the melting temperatures of the compounds that were previously known.

From an experimental point of view the characterization of congruently melting alloys as heat storage materials poses no great problems. The commercial calorimeters performed well within the expected limits, uncertainties of 5% for DTA and 3% for DSC. Conversion of heat storage densities from a mass to a volume basis requires improved density measurements. The present uncertainty in the room-temperatures densities is due mainly to the porosity of the alloys. The use of the induction furnace, with its vigorous stirring yielded alloys with low

porosity. Measurements of densities at the transition temperatures are being performed in a related study (20).

Although the DCS gave reliable heat capacities for alloys that melt below 700°C, for the higher temperature alloys the measurement of heat capacities of the liquid should be done by some method other than DTA. Vaporization losses and reaction of the vapors with the Pt cups are likely to be responsible for the failure of DTA to yield acceptable heat capacities. The vaporization problem does not affect the measurements of heat of fusion appreciably because this shift occurs to the baseline as a whole. However, there may be a residual effect that cannot be determined from the present results.

As reported previously (19), the heats of transformation are systematically well below the calculated values as summarized in Table 5. The predictions of the ideal model deviate to a large extent from the true eutectic temperatures, but the compositions are a useful approximation. The regular solution model improves the values obtained for the temperatures, but not appreciably those for the compositions. In the ternary case there is no improvement whatsoever, due to the assumptions that had to be made in estimating the ternary activities from binary data.

Further alloying of the promising binary eutectics lowers the transformation temperature as expected, but it does not necessarily improve the heat storage density as expected. The deviation of the actual values from those calculated is erratic and unpredictable. The main reason for this variation probably is the different degrees of ordering that take place in the liquids. Since the presence of stable intermetallic compounds was sought to increase the heat of transformation, the probability of ordering in the liquid is high. To take this complication into account additional thermodynamic data are needed.

The fact that in many cases the addition of a third component did not improve the heat of transformation as expected suggests that ordering in the liquid is more likely for multicomponent systems than for binary systems. Statistically it is more likely that some pair of elements will exhibit strong affinity in the liquid and therefore contribute to short range ordering.

The practical implication of these conclusions is that it will be difficult to find alloys among these metals that have storage densities substantially greater than the ones presently reported, although some aspects of their performance such as volume change during melting may continue to improve. Investigation of quaternary alloys

may put metals into a more competitive position for heat storage at lower temperatures. Further alloying may also yield a better accommodation of the melting temperatures to the sources.

References

1. J. Schröder, J. Eng. Ind., 1975, vol. 97, pp. 893-396.
2. R. P. Tye, J. G. Bowne and A. O. Desjarlais, "Molten Salt Thermal Energy Storage," Dynatech Report 1503.
3. Ferrara, "Molten Salt Energy Storage," 12th Intersociety Energy Conversion Engineering, Washington, D.C., 1977.
4. Haru et al., NASA Report CR135419, March 1978.
5. Clayton, NASA Report CR 159427, October 1974.
6. C. E. Birchenall and M. Telkes, "Sharing of the Sun," vol. 8.
7. N. Pryor, unpublished research, University of Delaware, 1976.
8. Alan Riechman, Master's Thesis, Applied Sciences Program, University of Delaware, 1977.
9. L. S. Darken, J. Am. Chem. Soc., 1950, vol. 72, pp. 2909.
10. G. W. Toop, Trans, AIME, 1965, vol. 233, pp. 850.
11. F. D. Richardson, "Physical Chemistry of Melts in Metallurgy," vol. 1.
12. Olson and Toop, Trans. AIME, 1966, vol. 236, pp. 590.
13. Meijering, Acta Met., 1957, vol. 5, pp. 257.
14. Olson and Toop, Trans, AIME, 1969, vol. 245, pp. 905.
15. M. Hillert, "Phase Transformations," ASM, 1970.
16. Anasara, et al., CALPHAD, 1978, vol. 2, p. 1.
17. R. Hultgren et al., "Selected Values of the Thermo-hydamic Properties of Binary Alloys," 1973.
18. Eldridge et al., Trans. AIME, 1967, vol. 239, pp. 777.
19. C. E. Birchenall and Alan Riechman, "Heat Storage in Eutectic Alloys," Met. Trans. 1980, vol. 11A, p. 1415.

APPENDIX C REMOVED
REPRINT
NSG 3184

APPENDIX C

APPENDIX D

VOLUME CHANGE DURING MELTING OF EUTECTIC ALLOYS

BRUCE PREGGER

Radiation Source

In previous work the source of radiation used was an X-ray tube powered by a Philips XRG-3000 high voltage generator (Appendix C). An Ag tube was used to provide AgKα X-rays at 22Kev. The high intensity of this source necessitated the use of a graphite monochromator and Zr foil filters. Results for the volume expansion of Al, Al-0.12Si, and Al-0.18Cu were obtained with this system that agreed with previously reported data. However, several characteristics of this source were undesirable. Variations in the observed intensity were systematic in nature and were attributed to a real variation in the output of the X-ray tube over the course of an experimental run. These variations were dependent on the change of the rate of flow of cooling water to the generator, and possibly also on variations in line voltage. The total intensity of the tube was a problem. The simple addition of absorbing Zr foils was not satisfactory, because high energy continuum radiation was relatively unaffected and remained to saturate the detector. A monochromator eliminated the unwanted radiation, though problems in beam alignment resulted. After alignment, however, the monochromator-Zr foil combination produced an intensity which yielded good counting statistics with an intrinsic Ge detector. Finally, the nature of the experiment required that the sample furnace be placed in close contact with

the X-ray generator, a situation which led to the premature termination of experimental runs as the furnace became hot. A theoretical limit of 1000°C was obtainable with the furnace, but at about 800°C the metal base reached what was determined to be a maximum safe temperature.

The use of a radioactive isotope as an X-ray source in place of the X-ray tube and generator offers a number of advantages. The output intensity of an isotope is constant over experimental times within the limits of radioactive decay statistics. Such a source is small and easily managed; alignment can be facilitated. The source can be physically separated from the furnace, allowing maximum temperatures. The radiation from an isotope is characterized by sharp energy peaks, so that the use of an energy dispersive counting system with such a source makes possible measurements without a monochromator. The judicious choice of an isotope, most of which have more than one useful energy peak, allows measurements to be made on materials of very different densities. From these considerations it was concluded that the volume change studies should continue with an isotope replacing the X-ray tube/ generator.

The choice of an isotope was dependent upon the following factors--the energy peak (or peaks) had to optimize the volume change measurements for the greatest

number of alloys, and the isotope had to be commercially available at a reasonable price.

To optimize volume change measurements the equation

$$\frac{(I_\ell/I_s)}{2\sigma} = \frac{e^{-(\mu/\rho)t(\rho_s-\rho_\ell)}}{2(\sqrt{N}+\sqrt{BKG})}$$

N = number of counts - background (BKG)

2σ = uncertainty/measurement

must be maximized. This depends upon the thickness of the sample, a controllable parameter, the number of counts per measurement and background, which are somewhat adjustable, and on the volume change and mass absorption coefficient, determined by the material.

The alloys to be measured fell into two groups separated by their absorption characteristics--those containing Cu or Zn, and those that did not. Cu and Zn absorb radiation much more strongly than Al, Si, Mg, or P, and thus an alloy with either one must be measured with high energy X-rays. Radiation of this energy does not show enough variation with density to be of use with the lighter alloys. Another consideration is the detector, as a NaI crystal and a Ge detector behave considerably differently at different energies.

Calculations were done to compare the relative value of two promising isotopes, Cd-109 and Gd-153. Cd-109 has peaks at 22, 25 and 88 KeV, Gd-153 at 41 and 47 KeV. Calculations were made for the 22 KeV Cd and the 41 KeV Gd peak as they would be detected with a Ge solid state detector, and for the 88KeV Cd peak as it would be detected in a NaI crystal. A series of calculations was performed for each alloy at each wavelength in order to determine the sample thickness that would give the best volume change precision. Values of density were measured from our prepared samples. Mass absorption coefficients were estimated by summing the mass fractions of the coefficients of the component elements.* Elemental absorption coefficients are given in Table 1, estimated alloy coefficients in Table 2, and optimum volume change precisions with corresponding sample thicknesses in Table 3.

From Table 3, it can be seen that the 41 KeV Gd peak with Ge detector gave the best precision for the dense Cu,Zn alloys. For the lighter alloys the 22 KeV Cd peak gave the best results. This peak energy could not be used

*Volume change estimates were made by summing the mass fractions of reported elemental change values. The count rate was estimated through consideration of detector efficiencies and collimated radiation beam intensities produced by 5 mCi sources. Counting time was taken to be 1000 seconds.

Table 1

Mass Absorption Coefficients for Cd-109
Gd-153 (Cm^2/gm)

KeV	Mg	Al	Si	P	Cu	Zn	In
22(Cd)	2.12	2.60	2.7	3.95	24.38	26.75	
41(Gd)	0.4*	0.5*	0.6*	0.6*	4.0*	5.0*	
88(Cd)	0.17	0.19	0.2*	0.2*	0.67	0.78	2.2

Sources: "Handbook of Chemistry and Physics," 50th edition, C. R. C. Press, 1970; C. S. Barrett and T. B. Massalski "Structure of Metals," 3rd edition, McGraw-Hill, 1966. Starred values are interpolated.

Table 2

Estimated Mass Absorption Coefficients for Alloys

KeV	Al-0.12Si	Al-0.12Si-0.05Mg	Si-0.35Cu-0.28Mg	Cu-0.25P-0.14Zn	Zn-0.40Cu-0.15Mg
22(Cd)	2.6	2.5	10.3	20.6	24.3
41(Gd)	0.5	0.5	1.0	3.0	3.0
88(Cd)	0.19	0.19	0.36	0.57	0.65

Table 3

Calculated Relative Precisions for Volume Change Measurements; (optimum sample thicknesses (cm))

KeV	Al-0.12Si	Al-0.12Si-0.05Mg	Si-0.35Cu-0.28Mg	Cu-0.25P-0.14Zn	Zn-0.40Cu-0.15Mg
22(Cd)	8.5(0.4)	8.1(0.4)			
41(Gd)	4.8(0.5)	4.6(0.5)	1.1(0.3)	9.3(0.2)	6.8(0.2)
88(Cd)			0.26(0.5)	3.4(0.5)	2.6(0.5)

with the Cu and Zn alloys, but the 88KeV peak can, though with less precision than the Gd peak. It was decided to use the Cd-109 source. The better results for the light alloys would be useful for comparison to the results obtained for such materials with the X-ray tube used previously.

APPARATUS

Radiation Source

The Cd-109 isotope used was in the form of a small disk, 0.79 cm in diameter and 0.51 cm in thickness. It was supplied by New England Nuclear (model NER-465 LE66) and had an activity of 5 mCi. The source is collimated into a narrow beam by having it rest at the closed end of a 15 cm stainless steel tube, held in place by a smaller diameter tube of the same material which slides into the first tube. The second tube has an inside diameter of 0.4 cm which acts as the collimator. The 0.4 cm diameter corresponds to the active area of the disk source, ensuring the greatest possible radiation intensity for the collimated beam. These tubes containing the source are sunk into a lead brick, as shown in Figure 1.

Sample Furnace

The furnace is basically that used by Harrison (Appendix C) with some minor modifications. Five meters of Nichrome wire are wound about the outside of a 9 cm diameter

X-RAY SOURCE HOLDER

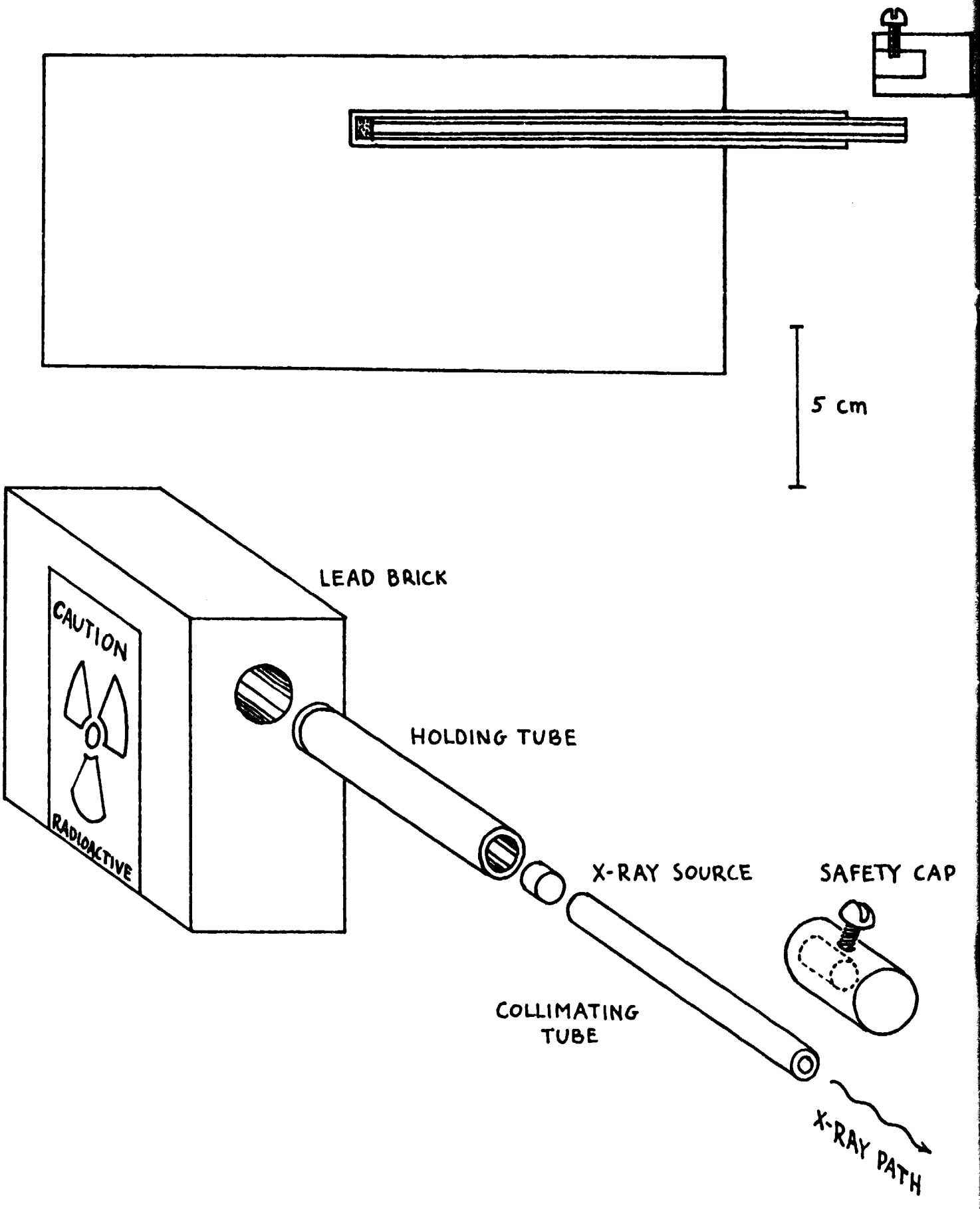

FIGURE 1

alumina tube. This tube has two 1 cm diameter holes drilled through it in order to let the X-ray beam pass. The tube sits upright in the center of the furnace on a refractory base. The sample holder is placed inside this tube. The furnace is designed to operate under vacuum. This vacuum is maintained in a stainless steel cover which fits onto an O-ring in the furnace base, and which has two windows built into it to allow the entrance and exit of the X-ray beam. These windows are made of beryllium, 0.01" thick, held in place by O-rings in stainless steel fittings soldered to the cover with silver solder. Thermocouple wires, electrical connections, and the vacuum line penetrate through the base of the furnace. The thermocouple is Chromel-Alumel. A vacuum of less than 5 torr is realized with a small mechanical vacuum pump. Between the furnace windings and the vacuum cover are two stainless steel heat shields and 1 cm thickness of heavy Alundum refractory. The furnace is shown in Figure 2.

Radiation Detectors

Two types of radiation detectors were used, depending on the energy of the radiation being measured. For low energies, the Cd-109 22 and 25 KeV peaks, a General Electric 400 high purity germanium spectrometer was found to give the best results. The resolution of this device at 22 KeV was measured to be 2.3%. At this energy a NaI scintillation crystal had very poor resolution, and could not resolve the 22 and 25 KeV peaks and thus could not

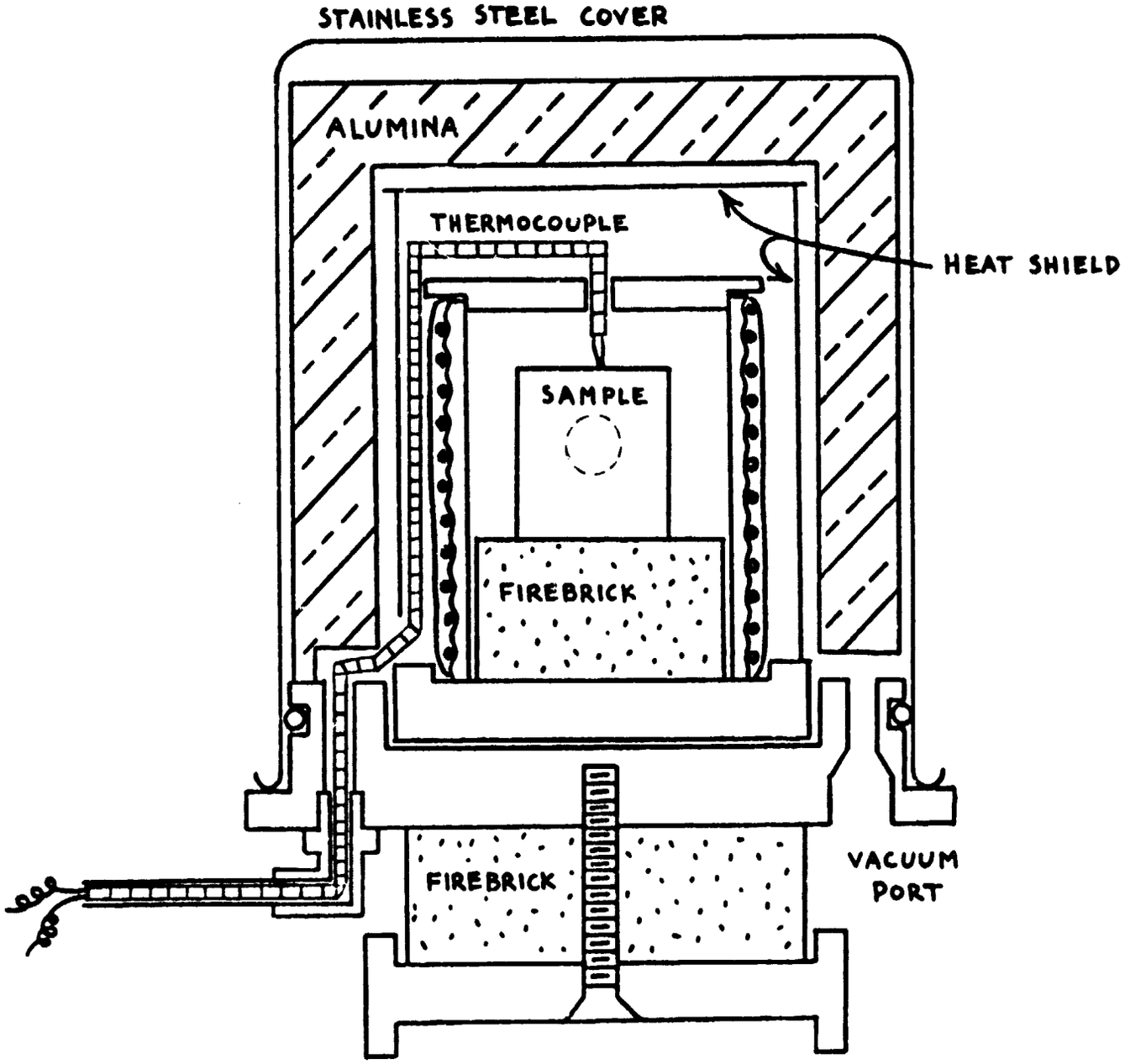
STAINLESS STEEL COVER
ALUMINA
THERMOCOUPLE
HEAT SHIELD
SAMPLE
FIREBRICK
FIREBRICK
VACUUM
PORT

FIGURE 2

measure truly monochromatic radiation, leading to erroneous results. However, as the energy increases the efficiency of the Ge counter drops rapidly. At 88 keV the counting rate of the Ge detector is at such a level that a NaI crystal is of more value as a monitoring device, even though the background count rate in the scintillation crystal is much greater.

The apparatus is arranged on a nonconducting bench top in such a manner as to allow changing from the solid state to the scintillation counter. The isotope holder and furnace are both small and easily repositioned, being physically separate.

Either detector was connected to a Tennelec TC 203BLR linear amplifier, from which the signal was run to a General Electric 700 multi-channel analyzer.

The arrangement of the apparatus is given in Figure 3.

Sample Holder

The sample holder has three requirements. It must keep the sample thickness constant throughout the experimental temperature range; it must allow enough radiation through the sample to provide good counting statistics; it must be made of material that will not react with the samples at elevated temperature. Graphite

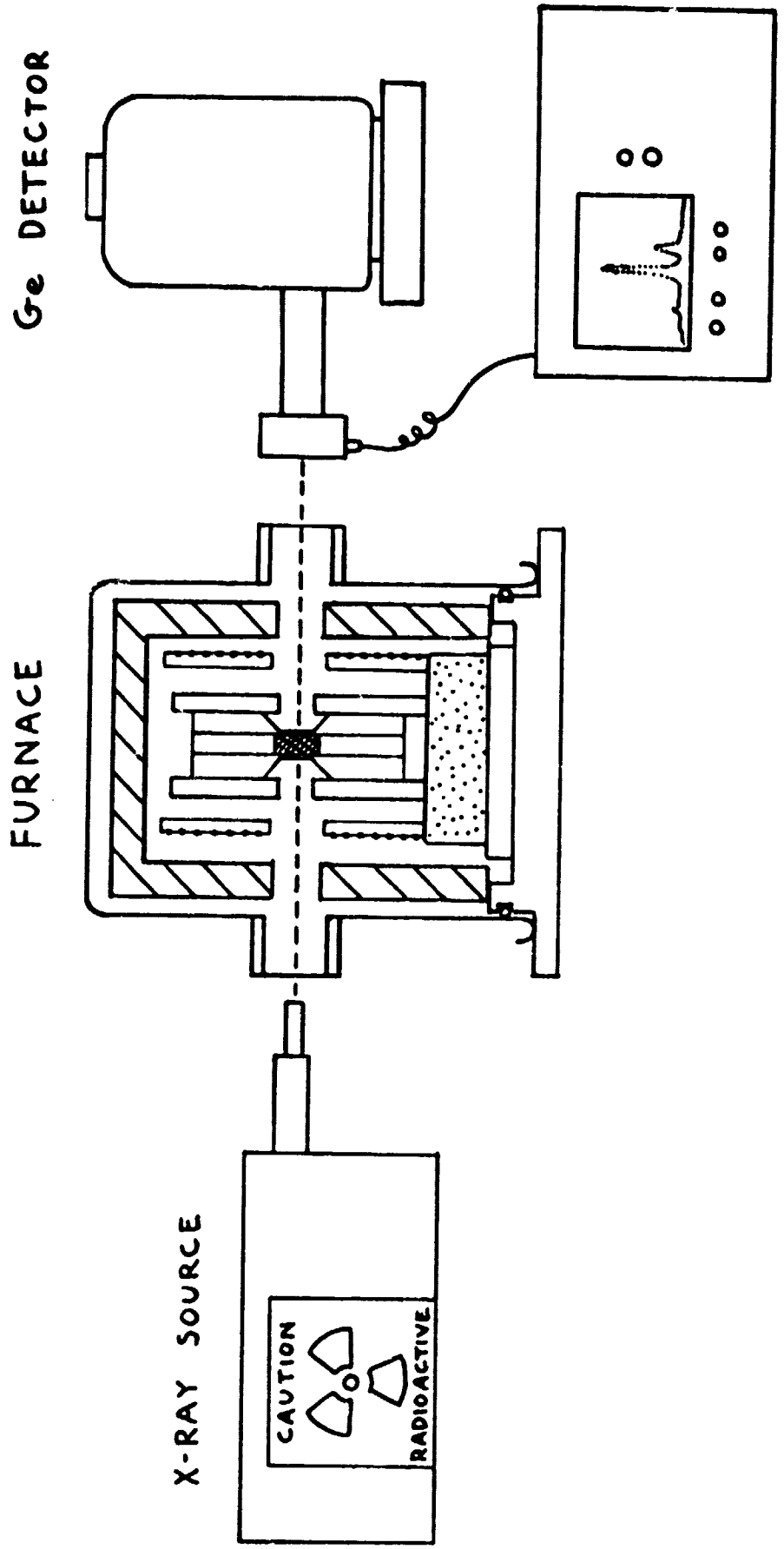
Ge DETECTOR
ANALYZER
FURNACE
X-RAY SOURCE
CAUTION
RADIOACTIVE

FIGURE 3

was chosen as the sample containment material. Three graphite plates are placed together, the center plate cut out in the center to contain the sample. The outer plates are thinned to 0.2 cm in their centers to allow passage of the radiation. These three plates are sandwiched between stainless steel plates and pressed together tightly with eight screws. The steel plates have holes cut out of their centers to allow X-ray transmission. The configuration is shown in Figure 4. Graphite was chosen as containment material because of ease of fabrication and low X-ray absorption characteristics. The 0.4 cm total path length for X-ray absorption in the sample holder is calculated to transmit 90.9% of incident radiation at the 22KeV Cd-109 peak, and 95.8% at the 88 KeV peak.

To facilitate alignment of the sample holder with the furnace windows, radiation source, and radiation detector, the holes in the stainless steel plates were threaded and fitted with 5 cm long tubes of the same material. These tubes defined the radiation path through the furnace winding and sample holder.

Samples

The aluminum and Al-0.12 Si samples were commercial materials. All other alloys were prepared by heating

SAMPLE HOLDER

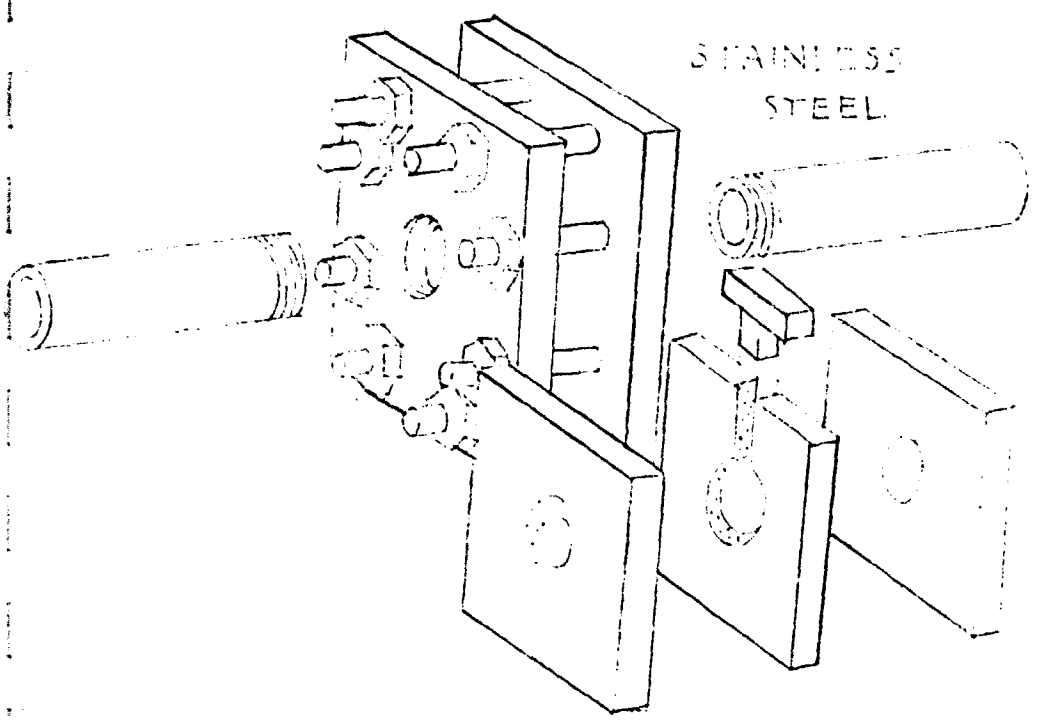

FIGURE 4

constituent elements and various commercial Mg, Si, P-metal compounds in an Ajax-Northrup induction furnace. The preparations were sealed in alumina crucibles to prevent vaporization of the volatile elements, and heated in an argon atmosphere to prevent oxidation. The induction heating provided good mixing of the alloys so that homogeneous eutectic structures resulted. The alloys were machined into disks that would fit tightly between the two outer graphite plates in the sample holder, but smaller in diameter than the hole in the center plate to allow for transverse expansion on heating and melting. The sample thicknesses were determined by optimum volume change calculations (see Table 3).

The alloys themselves were those which showed promise as heat storage materials. Eutectic compositions in the various systems were found by Farkas, Appendix B. The heats of fusion were measured in the same work. Those alloys which demonstrated the greatest heats of fusion have possible commercial utility and were chosen for this study. Their compositions are given in Tables 2 and 3.

Experimental Procedure

The alloy sample is placed inside the sample holder which is then screwed together tightly. The sample holder is positioned in the furnace so that the radiation passes from the source to the detector by way of the radiation

path tubes on the sample holder. The radiation from a 5 mCi Cd-109 source is too weak to permit the use of a fluorescent screen to check alignment; accuracy in this regard must be determined by counting with the detector. After satisfactory positioning of the sample holder in the furnace, the furnace cover is put in place and the vacuum pump is turned on. With the vacuum at 5 torr or less,counting may begin. The integral number of counts in the proper peak is recorded by the multi-channel analyzer for a period of 1000 seconds. A variable output transformer which controls furnace heating is turned on and the furnace is allowed to heat so that the temperature, as recorded by the Chromel-Alumel thermocouple, is raised by about 100 °C. At this point the transformer is adjusted until a temperature equilibrium is achieved. The multi-channel analyzer is turned on to record for another 1000 seconds. Changes is furnace temperature in this time period can be minimized with a skilled hand at the transformer; such variations are accounted for by averaging. The process is then continued, raising the temperature in 100° intervals through the melting temperature and into the liquid range as far as the furnace allows. Measurements are also taken for 1000 seconds during the heating intervals for comparative purposes, in which temperatures are recorded at the beginning and end of the 1000 sec interval and averaged.

RESULTS

The values obtained for volume changes of the various alloys studied are given in Table 4. Figures 5 and 6 show plots of ℓn intensity vs. temperature for the various materials studied. The solid and liquid phase data points were separately characterized as straight lines by the method of least squares. It was felt that the scatter of the data precluded the use of higher order polynomials. These lines were extrapolated to the melting point of the material. The values of the solid and liquid line at the melting point were taken as the natural log of the incident intensity produced by the solid and liquid melting point densities, and as such were used in calculating those densities. The value of the solid phase data line was used at room temperature to represent the room temperature density; the measured room temperature intensity was not. Precision was gained in this manner.

Numbers obtained for the solid and liquid expansion coefficients were not in agreement with previously measured values, nor were they to any great extent reproducible. This is a serious problem, for it can affect the fusion volume change calculation. The fusion volume changes calculated appear to agree with those that have been determined by Harrison and others (2-4). This study is concerned primarily with new alloys on which no data of this nature are available for verification.

Table 4

Volume Changes on Melting of In, Al, and Various Eutectic Alloys

	$(\Delta V/V_s)$ Measured	Tabulated	
In	0.031	0.025	(1)
Al	0.09	0.072	(2)
		0.0769	(3)
Al-0.12Si	0.041	0.040	(2)
		0.038	(4)
Al-0.12Si-0.05Mg	0.066		
Cu-0.25P-0.14Zn	0.033		

(1) Smithells, "Handbook of Metals" 1955.

(2) Harrison, Appendix C.

(3) P. J. Wray, Met. Trans., 1974, vol. 5, p. 2602.

(4) L. Mondolfo, "Aluminum Alloys," Butterworths, London, 1976.

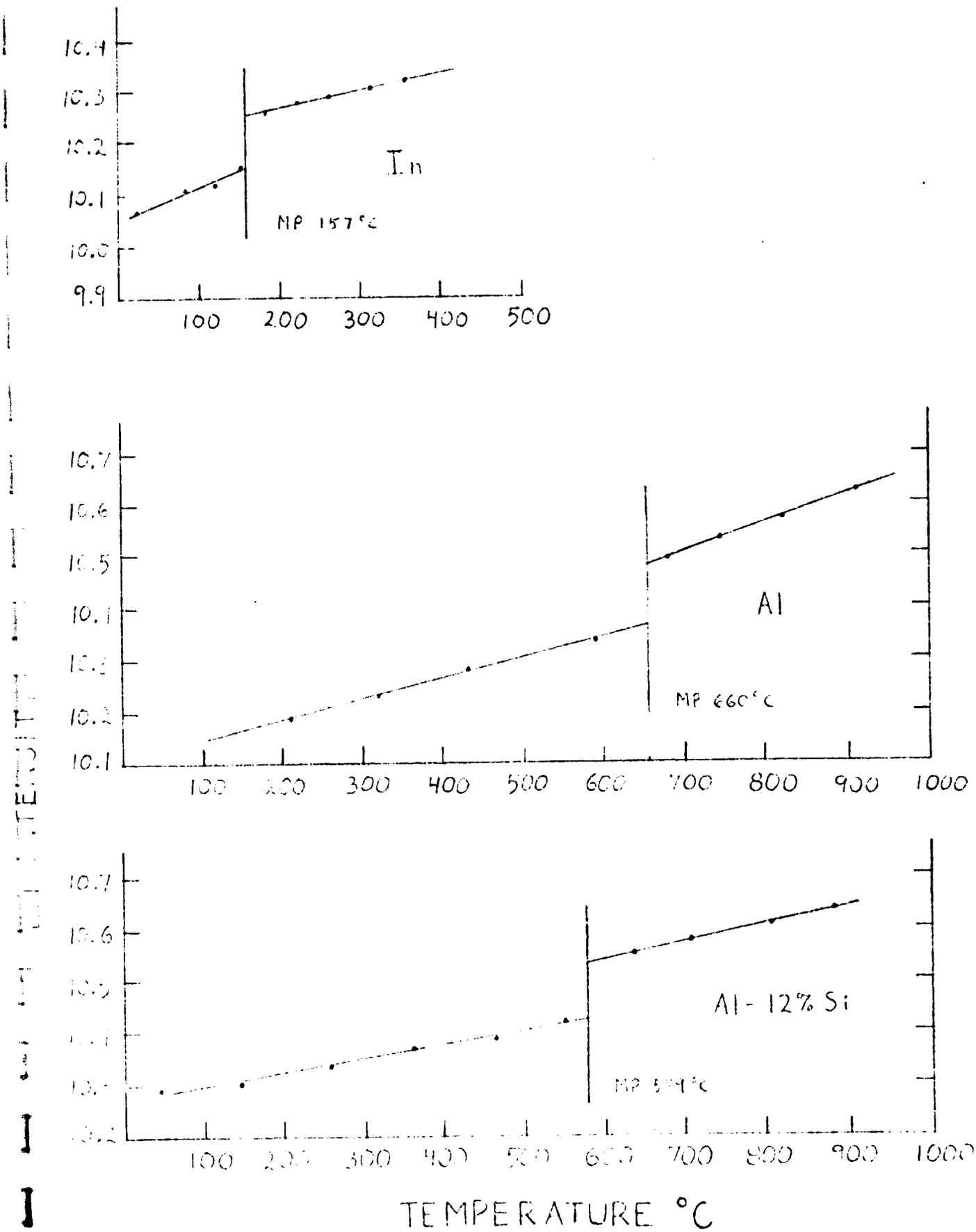
10.4
10.3
10.2
10.1
10.0
9.9
In
MP 157°C
100
200
300
400
500
10.7
10.6
10.5
10.1
10.2
10.1
Al
MP 660°C
100
200
300
400
500
600
700
800
900
1000
Al - 12% Si
MP 577°C
100
300
400
600
700
800
900
1000
TEMPERATURE °C

FIGURE 5

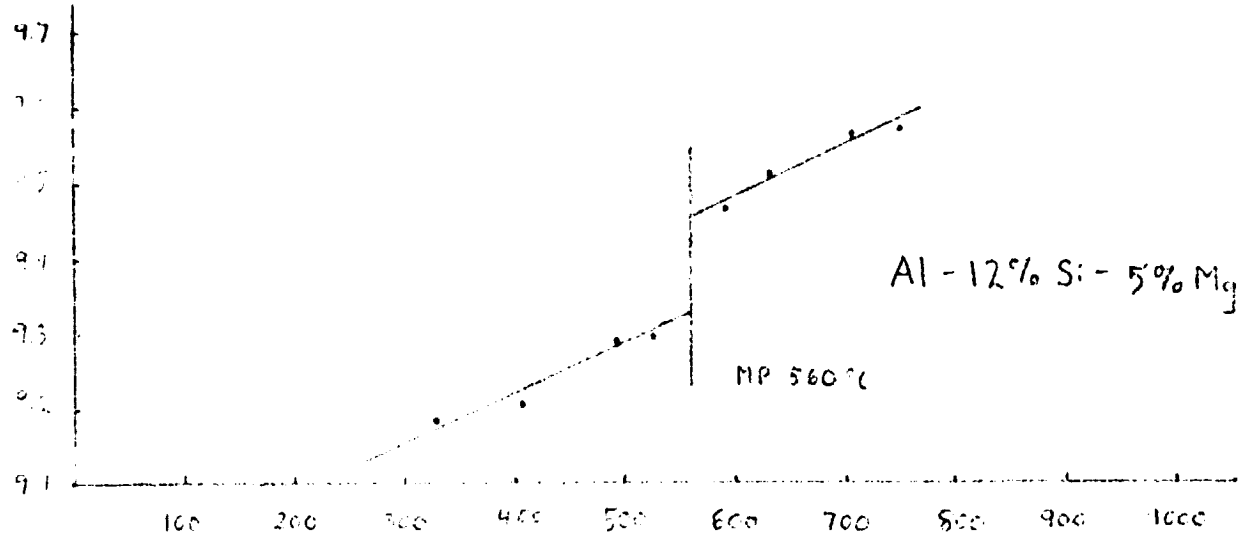

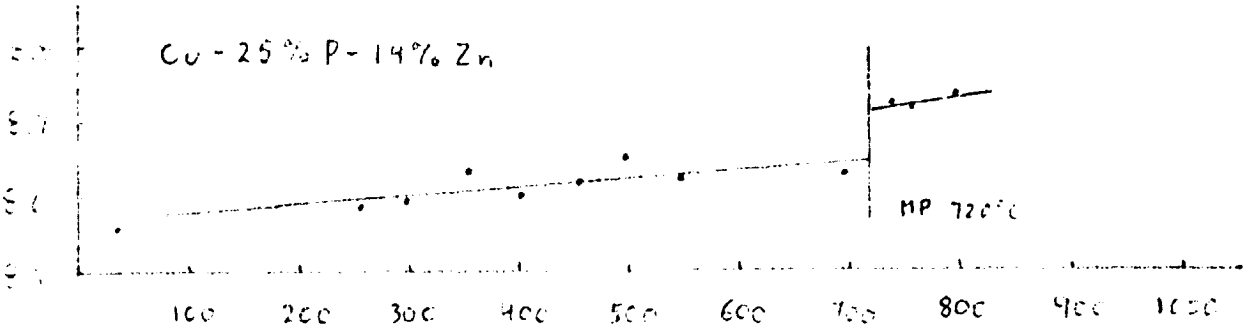

TEMPERATURE °C

FIGURE 6

Al-0.12Si had a change of volume on melting that was measured to be 4.1%, very close to the change of 4.0% given by Mondolfo (4) and 4.8% as measured by Harrison (2) with this method using an X-ray tube source.

In, measured with the 88 KeV peak, gave a value of 3.1% for the volume change. Smithells (1) gives 2.5%.

The runs made on pure aluminum were not altogether satisfactory. High volume changes were calculated from them, around 20% higher than the grouping of other experimental values (2-4). The reason for this remains unknown.

Al-0.12Si-0.05Mg gave a measured volume change of 6.6%. This value is probably too high, although there are no other measured values to check against. The presence of Mg has been found to be detrimental to the acquisition of good data when present in larger amounts in a graphite container; perhaps it is not helpful in this case.

Cu-0.25P-0.14Zn is an easy-to-handle alloy. The volume change measured was 3.3%, which in concert with a high heat storage capacity and ease of handling (it was made successfully in a resistance furnace) makes this material look very promising for commercial utilization.

DISCUSSION

The variability of solid and liquid expansion coefficients demands resolution. The problem stems from the changing of the radiation intensity in other parts of the furnace than the sample. Due to the low level of intensity produced by the radiation source, as wide a beam as possible is used. This leads to blocking by opaque surfaces in the furnace. When the furnace heats, these surfaces may move in such a manner as to increase or decrease the theoretical incident intensity so that the equation for $\rho_{mp} - \rho_{ROOM\ T}$ does not hold. To decrease the beam diameter to that usable with an X-ray tube source would decrease the intensity from the radioactive source to a level that would eliminate any chance of useful results. Experiments were done using an empty sample holder to test this theory of changing incident intensity, and what was found was that the furnace did change the intensity on heating, although not always by the same amount nor always even in the same direction. The $\rho_\ell - \rho_s$ is relatively unaffected by this problem coming from data of a single temperature, but if ρ_s is calculated wrong then the percentage volume change on melting will not be accurate.

A solution to this problem involves the simultaneous measurement of two peaks of different energies. Opaque blocking accounting for a changing incident intensity

may be eliminated between equations for the absorption at the two energies giving the following equation:

$$I''_{adjusted} = I''_{measured} \exp - \left(\frac{\left[\left[\frac{\mu/\rho_1}{\mu/\rho_2} \right] \ln \left(\frac{I'_2}{I''_2} \right) - \ln \left(\frac{I'_1}{I''_1} \right) \right]}{\left[1 - \left[\frac{\mu/\rho_1}{\mu/\rho_2} \right] \right]} \right)$$

where

$I''_{adjusted}$ = the intensity that would be measured had not the incident intensity been changed by opaque blocking from T' to T"

$\mu/\rho_{1,2}$ = mass absorption coefficients for radiation of energies 1 and 2

I'_1 = measured intensity at T' with energy 1 (for example)

$I''_{measured}$ = I''_1 or I''_2 , yielding corrections at both energies.

This equation accounts for partial opaque blockage, but there is no solution for the opposite effect, partial free transmission. Thus any porosity in the sample cannot be mathematically eliminated. Samples prepared in the induction furnace have shown good density characteristics, without excessive porosity.

Cd-109 has two peaks in the same energy range: 22 and 25 KeV. Test measurements were made on Al for corrections by the above equation. The 25 KeV peak is

relatively weak, yielding poor counting statistics, and results were inconclusive. Gd-153 on the other hand has two strong peaks in the same range, at 41 and 47 KeV. An active Gd source could be a solution to the problem.

Another problem was encountered when dealing with alloys rich in Mg. At elevated temperatures the Mg reacted with the graphite of the sample holder changing both sample thickness and sample composition. Such was the case for Si-0.35Cu-0.28Mg and Zn-0.40Cu-0.15Mg. A new material must be found to contain these alloys.

It appears as though a Gd-153 source could provide better results than the present Cd-109. The source and experimental configuration now being used do not seem wholly satisfactory, especially for expansion coefficient determination.

APPENDIX E

ANALYSIS OF CYLINDRICAL HEAT EXCHANGER WITH PHASE CHANGE MATERIALS

Michael B. Labdon
Graduate Student

Selçuk İ. Güçeri
Assistant Professor

Mechanical and Aerospace Engineering Department
University of Delaware
Newark, Delaware 19711, U.S.A.

ABSTRACT

Within the field of energy, there is an increasing emphasis on the use of phase-change materials (PCM) for thermal energy storage, but the analytical and numerical methods available to describe their thermal behavior in cylindrical coordinates are relatively few in number. In addition, these methods are either mathematically too complex for engineering purposes, or simplified to the point of solving a pseudophase-change process far removed from the actual system itself. In this paper, an efficient, numerical method is presented for modeling one-dimensional heat conduction (including sensible and latent heat) around an internally-convected cylinder of PCM. Finite-difference equations monitor the heat transfer within the solid and liquid regions, while Taylor-series expansions of temperature are made in the regions close to the interface. Inputs to the routine include temperature-dependent properties, initial temperature distributions, time-varying convection boundary conditions and time-varying inlet fluid temperatures. Outputs from the method include melt-line locations and temperature distributions vs. time, as well as charging rates and pipe surface temperatures.

1. INTRODUCTION

Many heat transfer processes include a change of phase of a material due to melting or solidification. Ice formation, ablation of missile skins and solidification of metal castings are a few such applications. Within the fields of Thermal and Solar Energy Storage, there is an increasing emphasis on the use of such phase-change materials (PCM), for the collection, storage and transmission of the forms of energy which today are more costly to generate and more actively conserved. The many applications of, and increased interest in, PCM's require accurate mathematical modeling of the thermal behavior of such materials. Predictions of melt-line locations and temperature histories throughout the medium are useful in: a) choosing the appropriate material for PCM containment, b) optimum design of the PCM apparatus, and c) the contrasting of several PCM's to choose those applicable for a specific use. Due to the inherent temperature non-linearity at the interface, mathematical modeling of the phase-change process via an

analytic approach is quite complicated. As a result, solutions exist for systems with simple geometries and very restrictive boundary and initial conditions. The extension to systems in cylindrical coordinates further reduces the number of available solutions due to the added mathematical complexity of the 1/r term in the original heat conduction equation. However, this is the system geometry often used with PCM's and energy storage or transmission; such as that found with heat exchangers, heat pipes, tube flows, etc.

Authors such as Meyer [2], Poots [3], Solomon [4], Boley [5], Krieth [6], JiJi [7], Shubin [8] and Sikarskie [14] have attempted such modeling, but required such restrictions as constant wall temperature, constant material properties or temperature distribution assumptions. The intricate mathematics or system-simplification of such methods preclude their use for engineering purposes. This is also evident in the numerical solutions alternately employed to model the phase-change process. Talwar [9] and others reduced the problem to one of pseudomelting whereby the thermal properties at the interface were "smoothed out" to provide a continuous relationship between the solid and liquid regions. Forster [10] considered the use of a quadratic temperature profile through the melt-line between two known points in an effort to compute the temperature gradients at the melt-front and hence its velocity. Murray and Landis [11] further refined Forsters model by instituting temperature profiles three nodes from the interface, but resulted in starting and terminating errors that propagated throughout the solution. Lazaridis [12] attempted to expand Murray and Landis' work to multidimensional systems, and resulted in developing a routine both mathematically and computationally difficult to implement with various geometries.

This paper outlines an efficient, numerical routine for solving one-dimensional heat conduction (including sensible and latent heat) around an internally-convected cylinder of PCM, by noting the dominant mode of heat conduction to be in the radial direction. Finite-difference equations monitor the heat conduction in the regions away from the fusion front, while Taylor-series expansions of temperature are made near the melt-line, in such a manner as to continually trace its propagation throughout each node, while adjusting all nodal temperatures. The versatility of the method is reflected in the fact that temperature-dependent properties and initial temperature distributions may be included as well as time-varying boundary conditions. Time-dependent inlet fluid temperatures can also be handled which represents the more realistic condition encountered with energy storage and transfer systems

2. PROBLEM STATEMENT

The heat exchanger geometry under consideration is depicted in Figures 1 and 2. Figure 1 is an axial view of a cylinder section of length "ℓ", containing a PCM partitioned into "N" equal-thickness, concentric, annular regions or nodes, with a representative melt-line location. Heat convection occurs at the inner radius R_1, and, for the analysis, one-dimensional solidification occurs radially outward. The outer radius R_2, is an insulated boundary, but may also be subjected to convection if required. As

the convecting fluid travels through the cylinder section an energy balance, described in Section 4.5, is performed on its bulk temperature to arrive at an increased outlet temperature. This in turn becomes the inlet flow temperature for the next downstream section. This process is repeated for "M" sections until the desired pipe length of "Mℓ" is attained, as depicted in Figure 2. In this manner, by taking a sufficiently large number of axial segments, the heat exchanger can be effectively modeled as a two-dimensional system with the one-dimensional radial heat conduction mode dominating the axial conduction mode.

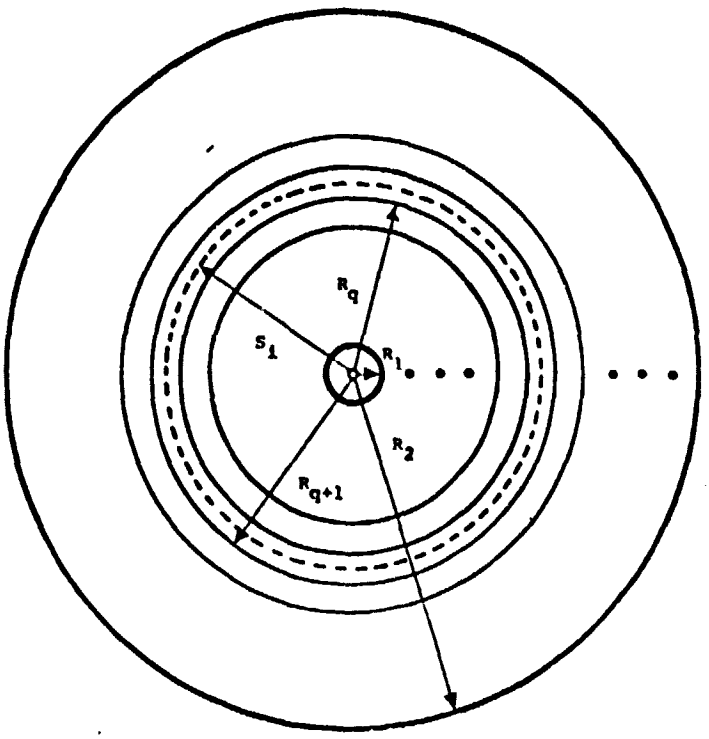

Figure 1. Axial view of heat-exchanger with representative concentric rings (nodes) of PCM, depicting a particular melt-line location.

3. PROBLEM SOLUTION

The only requirements of the following analysis are that the fusion temperature is constant, the density is constant in both phases, and that natural convection effects are negligible. Use of the foregoing restrictions is acceptable for many engineering purposes, while exclusion of the same would result in a more complicated system modeling. As previously mentioned, only radial heat conduction will be considered.

The problem analysis is facilitated by the introduction at

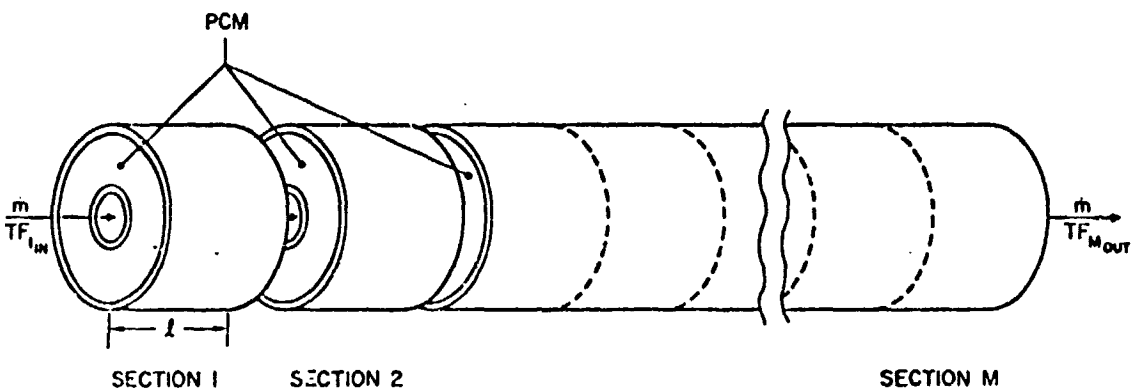

Figure 2. Horizontal view of heat exchanger of length "Mℓ" containing a PCM between an internally-convected pipe and an insulated outer one.

this point, of the governing equations used throughout the phase-change medium:

$$\frac{\partial^2 T_1}{\partial r^2} + \frac{1}{r}\frac{\partial T_1}{\partial r} = \frac{1}{\alpha_1}\frac{\partial T_1}{\partial t} \qquad R_1 \leq r \leq S \qquad (1a)$$

$$\frac{\partial^2 T_2}{\partial r^2} + \frac{1}{r}\frac{\partial T_2}{\partial r} = \frac{1}{\alpha_2}\frac{\partial T_2}{\partial t} \qquad S \leq r \leq R_2 \qquad (1b)$$

$$k_1 \frac{\partial T_1}{\partial r} - k_2 \frac{\partial T_2}{\partial r} = L\rho \frac{dS}{dt} \qquad r = S(t) \qquad (2)$$

$$T_1 = T_2 = T_m \qquad r = S(t) \qquad (3)$$

where subscripts 1 and 2 denote the solid and liquid regions respectively. Eqs. 1a, b are the field equations in the solid and liquid regions. Eq. 2 is the well-known Stefan Condition resulting from an energy balance at the interface, and Eq. 3 is the condition of constant fusion temperature. As an added convenience, the following non-dimensionalizing parameters are introduced into the above equations:

$$\xi \equiv r/R \; ; \; \tau \equiv \alpha_1 t/R^2 \; ; \; \varepsilon(\tau) \equiv S(t)/R \; ; \; \Delta\xi \equiv \Delta r/R \; ; \; K \equiv k_2/k_1$$

$$\gamma_\ell \equiv \alpha_2/\alpha_1 \; ; \; \lambda \equiv L/C_1 \; ; \; \delta\xi \equiv \delta r/R \; ; \; \xi_1 \equiv R_1 \; ; \; \xi_N \equiv R_2$$

where R is a chosen reference length. The resulting equations, in which all variables except temperature are non-dimensionalized, appear as:

$$\frac{\partial^2 T_1}{\partial \xi^2} + \frac{1}{\xi}\frac{\partial T_1}{\partial \xi} = \frac{\partial T_1}{\partial \tau} \qquad \xi_1 \leq \xi \leq \varepsilon \qquad (4a)$$

$$\frac{\partial^2 T_2}{\partial \xi^2} + \frac{1}{\xi}\frac{\partial T_2}{\partial \xi} = \frac{1}{\gamma_\ell}\frac{\partial T_2}{\partial \tau} \qquad \varepsilon \leq \xi \leq \xi_N \qquad (4b)$$

$$\frac{\partial T_1}{\partial \xi} - K\frac{\partial T_2}{\partial \xi} = \lambda \frac{d\varepsilon}{d\tau} \qquad \xi = \varepsilon(\tau) \qquad (5)$$

Figure 3 illustrates the cross-sectional, radial view of a

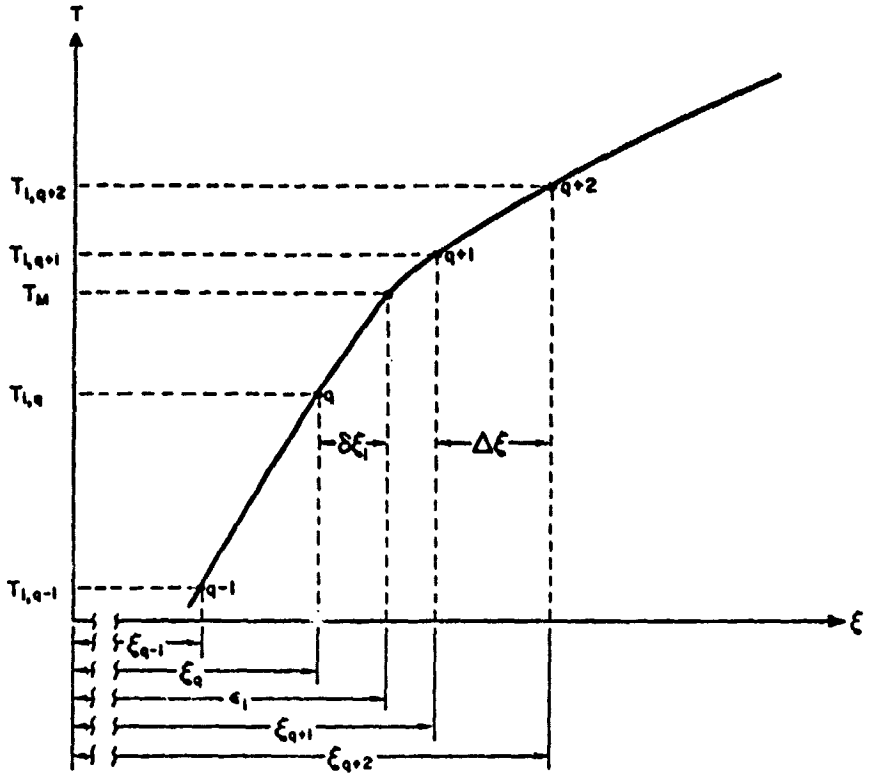

Figure 3. Radial Temperature distribution near the interface, within a particular pipe section.

representative pipe section "i", $1 \leq i \leq M$, undergoing solidification at some intermediate time "τ", where the melt-line has just traveled to the distance $\epsilon_i(\tau)$. The node in the solid region closest to the interface is denoted as "q", while "q + 1" represents the similar node in the liquid region. The nodal spacing, $\Delta\xi$, is defined as $(\xi_N - \xi_1)/(N - 1)$ while $\delta\xi$ is the time-varying distance between node q and ϵ_i. At this particular time τ, only the current location ϵ_i is known, as well as the "old" $(\tau - \Delta\tau)$ nodal temperatures $T_{i,j}$; i = 1, M; j = 1, N. The calculation of "current" temperatures and future melt-line positions requires the successive execution of the following computational logic:

a) Determine all nodal temperatures except $T_{i,q}$ and $T_{i,q+1}$, at time τ via the finite-difference equations,

b) Compute the current temperature gradients at the interface, $\partial T_1/\partial\xi\,|_{\epsilon_i} \equiv A_i$ and $\partial T_2/\partial\xi\,|_{\epsilon_i} \equiv B_i$ and,

c) Determine the current values for temperatures $T_{i,q}$ and $T_{i,q+1}$, as well as the melt-front velocity $d\epsilon_i/d\tau$,

all of which are outlined in the next three sub-sections.

3.1. Finite-Difference Equations

Temperatures at all nodes i,j where $1 \leq i \leq M$ and $1 \leq j \leq q-1$,

$q + 2 \leq j \leq N$ are computed from the usual finite-difference approximation to the original heat conduction equation (4),

$$\left(\frac{T_{i,\,j-1} + T_{i,\,j+1} - 2T_{i,j}}{\Delta\xi^2}\right) + \frac{1}{\xi}\left(\frac{T_{i,j+1} - T_{i,j-1}}{2\Delta\xi}\right) = \frac{1}{\gamma}\left(\frac{T'_{i,j} - T_{i,j}}{\Delta\tau}\right) \tag{6}$$

where $T'_{i,j}$ denotes the new value for $T_{i,j}$ after the time increment $\Delta\tau$, and $\gamma = 1$ when j is within the solid region or $\gamma = \gamma_\ell$ when j is within the liquid region. $T_{i,j}$ is solved from (6) as,

$$T'_{i,j} = T_{i,j}\left(1 - \frac{2\gamma\Delta\tau}{\Delta\xi^2}\right) + \frac{\gamma\Delta\tau}{\Delta\xi^2}\left(T_{i,j+1} + T_{i,j-1}\right) + \frac{\gamma\Delta\tau}{2\xi\Delta\xi}\left(T_{i,j+1} - T_{i,j-1}\right) \tag{7}$$

yielding the first familiar stability criterion

$$\Delta\tau < \Delta\xi^2/2\gamma \tag{8}$$

Two modifications of (7) are required for the two boundary conditions specified in the problem description.

Insulated boundary. The outer boundary temperatures are determined from (7) by setting $T_{i,j+1} = T_{i,j-1}$, thus

$$T'_{i,N} = T_{i,N}\left(1 - \frac{2\gamma\Delta\tau}{\Delta\xi^2}\right) + \frac{2\gamma\Delta\tau}{\Delta\xi^2}\,T_{i,N-1} \tag{9}$$

Convection boundary. Using the fictitious node concept posited by Özışık [13], the nodes $T_{i,j-1}$ for $j = 1$ are defined as T_{fic_i}, and their values are arrived at via an energy balance at the convective boundary

$$k_1\left(\frac{T_{i,2} - T_{fic_i}}{2\Delta r}\right) = h\,(T_{i,1} - T_{f_i}) \tag{10}$$

where T_{f_i} is the bulk fluid temperature at location "i". Solving

for the fictitious nodal temperatures in (10) yields,

$$T_{fic_i} = 2\Delta\xi \, Bi(T_{f_i} - T_{i,1}) + T_{i,2} \tag{11}$$

where the Biot number $Bi = h\,R/k_1$ Inserting (11) into (7) yields the relation

$$T'_{i,1} = T_{i,1}\left[1 - \frac{2\gamma\Delta\tau}{\Delta\xi}\left(\frac{1}{\Delta\xi} + Bi + \frac{Bi\Delta\xi}{2\xi_1}\right)\right] + T_{i,2}\left(\frac{2\gamma\Delta\tau}{\Delta\xi^2}\right)$$

$$+ T_{f_i}\left(\frac{2}{\Delta\xi} - \frac{1}{\xi_1}\right)\gamma\Delta\tau \, Bi \tag{12}$$

From (12) arises a more restrictive time stability criterion,

$$\Delta\tau \leq \frac{\Delta\xi}{2\gamma}\left(\frac{1}{\Delta\xi} + Bi + \frac{Bi\Delta\xi}{2\xi_1}\right)^{-1}$$

to be used in place of (8), and a second, milder, geometric criterion from the coefficient of the third term in that

$$\frac{2}{\Delta\xi} - \frac{1}{\xi_1} > 0 \quad \text{or} \quad \Delta\xi \leq 2\xi_1$$

which implies that the mesh size should be sufficiently smaller than the cylinder inner radius. Thus, equations (7), (9) and (12) are used to determine all "current" nodal temperatures except $T_{i,q}$ and $T_{i,q+1}$.

3.2. Interface Region

At this point, Taylor series expansions of temperature are imposed from the melt-line to the two known temperatures, $T_{i,q+2}$ and $T_{i,q-1}$, in the form

$$T_k(\xi) = T_k\Big|_{\varepsilon_i} + (\xi - \varepsilon_i)\frac{\partial T_k}{\partial \xi}\Big|_{\varepsilon_i} + \frac{(\xi - \varepsilon_i)^2}{2}\frac{\partial^2 T_k}{\partial \xi^2}\Big|_{\varepsilon_i}$$

$$k = 1, 2 \tag{14}$$

generating the following two equations:

$$T_{i,q-1} = T_m - (\Delta\xi + \delta\xi_i)A_i + \frac{(\Delta\xi + \delta\xi_i)^2}{2} \left.\frac{\partial^2 T_1}{\partial \xi^2}\right|_{\varepsilon_i} \tag{15}$$

$$T_{i,q+2} = T_m + (2\Delta\xi - \delta\xi_i)B_i + \frac{(2\Delta\xi - \delta\xi_i)^2}{2} \left.\frac{\partial^2 T_2}{\partial \xi^2}\right|_{\varepsilon_i} \tag{16}$$

containing the unknowns A_i, B_i and the two second derivatives. In addition, (17) is valid at the melt-line for all times,

$$\left.\frac{dT_k}{d\tau}\right|_{\varepsilon_i} = 0 = \left.\frac{\partial T_k}{\partial \tau}\right|_{\varepsilon_i} + \left.\frac{\partial T_k}{\partial \xi}\right|_{\varepsilon_i} \frac{d\varepsilon_i}{d\tau} \qquad k = 1, 2 \tag{17}$$

where the first quantity on the right hand side is merely the heat conduction equation (4). Thus, (17) gives rise to two more equations

$$\left.\frac{\partial^2 T_1}{\partial \xi^2}\right|_{\varepsilon_i} + \frac{A_i}{\varepsilon_i} + A_i \frac{d\varepsilon_i}{d\tau} = 0 \tag{18a}$$

$$\left.\frac{\partial^2 T_2}{\partial \xi^2}\right|_{\varepsilon_i} + \frac{B_i}{\varepsilon_i} + B_i \frac{d\varepsilon_i}{d\tau} = 0 \tag{18b}$$

with the introduction of another unknown $d\varepsilon_i/d\tau$, which is the Stefan Condition (5) rewritten below as,

$$\frac{d\varepsilon_i}{d\tau} = \frac{1}{\lambda}(A_i - KB_i) \tag{19}$$

Hence, by solving (15) and (16) for the second derivative terms and substituting (19) into (18) yields two coupled equations with the two unknown gradients,

$$A_i^2 + A_i\left(\frac{\lambda}{\epsilon_i} + \frac{2\lambda}{d_1}\right) - A_iB_iK + \frac{2\lambda}{d_1^2}\left(T_{i,q-1} - T_m\right) = 0 \qquad (20)$$

$$B_i^2 + B_i\left(\frac{2\gamma\lambda}{Kd_2} - \frac{\gamma\lambda}{K\epsilon_i}\right) - \frac{A_iB_i}{K} + \frac{2\gamma\lambda}{d_2^2K}\left(T_m - T_{i,q+2}\right) = 0 \qquad (21)$$

where $d_1 = \Delta\xi + \delta\xi_i$, $d_2 = 2\Delta\xi - \delta\xi_i$. These two equations are then applied at each "ith" location, where A_i and B_i are found via an iterative process, such as a Newton-Raphson routine.

3.3. Determination of $T_{i,q}$ and $T_{i,q+1}$

With the known temperature gradients, (15) and (16) can be solved for the two second derivatives, in which case everything is known about the Taylor-series expansions made near the interface. Of further significance is the fact that such expansions imply a quadratic temperature distribution throughout the interface regions which is evident in the similarity between (14) and

$$T(\xi) = a + b\xi + c\xi^2 \qquad (22)$$

where $a = T_m$, $b = A_i$ or B_i and $c = \partial^2T_1/\partial\xi^2\,|_{\epsilon_i}$ or $\partial^2T_2/\partial\xi^2\,|_{r_i}$ depending upon the region. Thus, temperatures at nodes "q" and "q + 1" can be calculated from (22) by using $\xi = -\delta\xi_i$ and $\xi = \Delta\xi - \delta\xi_i$ respectively.

Lastly, the new melt-front velocity at each "i" location is computed from (19). In general, the future melt-line position within each pipe section is determined by multiplying the melt-line velocity times the time-discretization parameter $\Delta\tau$ (this represents an inherent limitation in the finite-difference method where the values calculated are to remain constant over the time interval $\Delta\tau$). However, due to the cylindrical nature of the problem, i.e. the increase in surface area faced by a radially expanding interface, the Stefan Condition which heretofore was appropriately utilized in the mathematical derivations at the melt-front, must be interpreted differently when dealing with a time-increment analysis. The energy balance at the interface, assuming unit depth, is

$$k_1(2\pi r_t)\frac{\partial T_1}{\partial r} - k_2(2\pi r_t)\frac{\partial T_2}{\partial r} = \frac{\rho LV}{\Delta t} \qquad (23)$$

where V is the volume of material undergoing a change of phase during the time increment, or $\pi(r^2_{t-\Delta t} - r_t^2)$, and r_t is the radial melt-line location at time "t". In non-dimensional form, (23) re-

duces to

$$A_i - KB_i = \lambda \left(\frac{\varepsilon_{\tau+\Delta\tau} - \varepsilon_t}{\Delta\tau} \right) \cdot \left(\frac{\varepsilon_{\tau+\Delta\tau} + \varepsilon_\tau}{2\varepsilon_\tau} \right) \tag{24}$$

which is similar to (19) multiplied by an adjustment factor that reduces to unity as $\Delta\tau$ is made relatively small. With the newly computed value of melt-line location at each "ith" section, the process outlined in 3.1 to 3.3 is repeated anew, and in this manner the melt-line propagation and nodal temperatures are continuously monitored throughout the medium.

3.4 Starting Procedure

For the initialization analysis, the more general case of superheat will be taken and it is assumed that the entire medium is subject to a temperature distribution containing temperatures greater than T_m. Heat convection imposed at the inner radius successively reduces the wall temperature, at a particular "i" location, to a point where change of phase is about to begin ($\tau = 0$). At this time the temperature distribution throughout the liquid has been determined by the finite-difference equations alone. From this existing distribution, the first three nodal temperatures are used in (22) to determine a temperature distribution, from which $\partial T_2/\partial \xi \,|_{\varepsilon_1}$ can be determined, in a manner similar to that of [16],

$$B_i\Big|_{\tau=0} = \left(2\, T_{i,2} - \frac{T_{i,3}}{2} - \frac{3}{2}\, T_m \right) \Big/ \Delta\xi \tag{25}$$

Alternately, we can solve for the second derivative term in (22), and use (18b) to solve for the fusion front velocity during the first time increment,

$$\frac{d\varepsilon}{d\tau}\Big|_{\tau=0} = \left(\frac{-\partial^2 T_2}{\partial \xi^2}\Big|_{\xi_1} - \frac{B_i}{\xi_1} \right) \Big/ B_i \tag{26}$$

Although theoretically the melt-line velocity initiates at infinity, the above analysis provides a usable value of velocity for input to the finite-difference routine. This novel approach obviates the more difficult task of first determining the values A_i, which now are more easily derivable from (19) as

$$A_i = \frac{d\varepsilon_i}{d\tau}\, \lambda + K\, B_i \qquad \tau = 0 \tag{27}$$

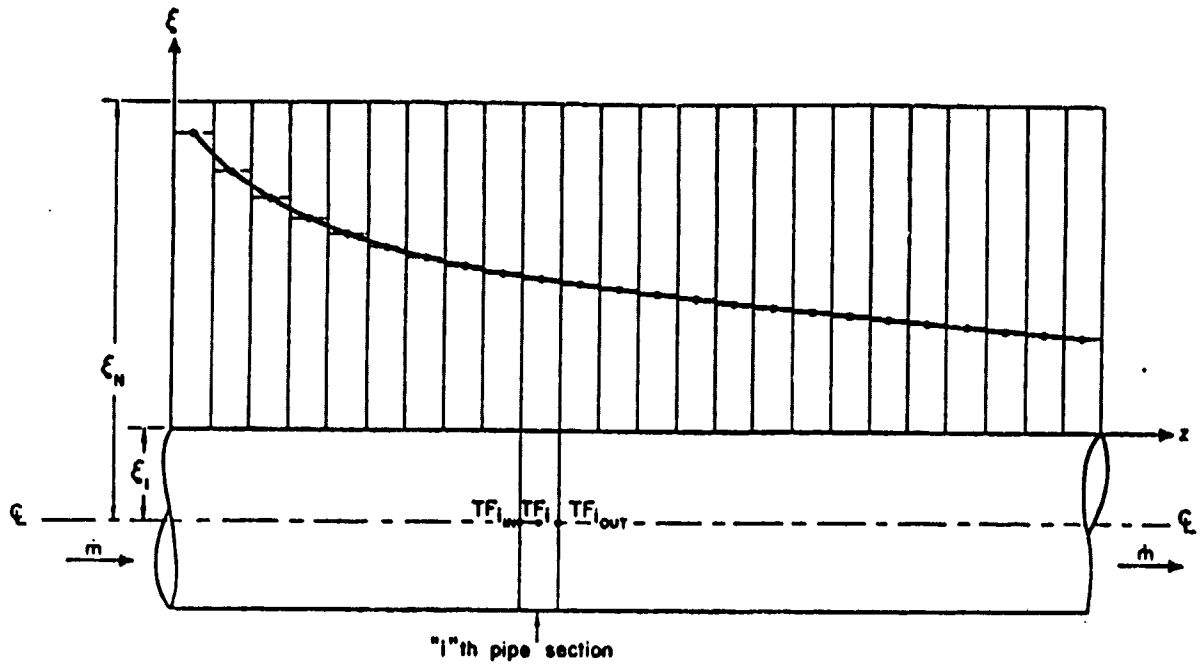

Figure 4. Cross-sectional view of the heat-exchanger with a smooth-line approximation to the "M" melt-line locations, and an elemental fluid flow section, at an intermediate time "τ".

line locations of the "M" axial sections, as well as a representative pipe flow section. An iterative method is employed to determine the average bulk temperature T_{f_i}, whereby successive energy balances are performed on the volume of fluid passing through the particular node "i". During the first pass in the method, T_{f_i} is assumed to be equal to the incoming fluid temperature $T_{f_{i,in}}$. Thus, an energy balance on the fluid element (31) yields the maximum fluid outlet temperature $T_{f_{i,out}}$

$$Q = \left(hA\ T_{i,1} - T_{f_i}\right) = \dot{m}C_f\left(T_{f_{i,out}} - T_{f_{i,in}}\right) \qquad (31)$$

Of course, the actual bulk fluid temperature T_{f_i} is higher than that of $T_{f_{i,in}}$ due to the heating of the fluid as it passes through the node, and is now approximated by averaging the newly computed values as

$$T_i = \frac{T_{f_{i,in}} + T_{f_{i,out}}}{2}$$

The energy balance (31) is again applied to yield a smaller value of $T_{f_{i,out}}$ and the above process is iterated until successive calculations of T_{f_i} are within a desired tolerance. At this point $T_{f_{i+1,in}} = T_{f_{i,out}}$, and the method is carried out repeatedly until

the fluid exits the pipe. The fluid temperatures are adjusted after each time step used in the finite-difference routine.

3.6 Melt-Line Crossing a Node

When a newly computed melt-line at an "ith" location indicates that the melt-line has crossed over node "q+1", an error arises in the computation of $T_{i,q-1}|_{\tau}$ (formerly $T_{i,q}|_{\tau-\Delta\tau}$), whereby the temperature $T_{i,q}|_{\tau-\Delta\tau} = T_m^+$ is erroneously used in the finite-difference routine to compute $T_{i,q-1}|_{\tau}$ (Actually, during the time-increment, its temperature varies from T_m^+ to T_m^-, or, a value less than the melting temperature). To avoid this inconsistency, the time step is adjusted (reduced) so that the melt-line falls exactly on the node q+1. At this time, the Taylor-series expansions are properly carried out, the new melt-line time location is determined by resuming the full time step, and the normal-procedure is followed.

3.7 Terminating Procedure

In the case of an insulated boundary at ξ_N, the following routine is used as the melt-line just crosses the node ξ_{N-1}. Similar to the starting solution (3.4), the nodal temperature $T_{i,q+2}$ is non-existent, and the Taylor-series (14) is made only to node ξ_N. Using the insulated boundary condition

$$\left.\frac{\partial T_2}{\partial \xi}\right|_d = 0$$

in (14) where $d = \Delta\xi - \delta\xi_i$, solving for the second derivation term, and substituting this into (18b) yields

$$B_i^2 + B_i\left(\frac{\lambda}{Kd} + \frac{\lambda}{\epsilon_i K}\right) - \frac{B_i A_i}{K} = 0 \qquad (32)$$

which replaces (21) when the melt-line is between the nodes ξ_{N-1} and ξ_N. The current value of $T_{i,N}$ is then computed from (22) which reduces to

$$T_{i,N} = T_m + \frac{dB_i}{2} \qquad (33)$$

3.8 A Third Stability Criterion

The third and most restrictive stability criterion results from an analysis in Appendix I, (adapted from [16]), whereby the start-

ing solution used in Sec. 3.4 to generate nodal temperatures is meshed with the finite-difference routine yielding the same nodal temperatures. The resulting criterion is that the thermal parameters and node size should be chosen such that $B \Delta\xi > 1.0$ or

$$\frac{h}{k_l} \Delta r > 1 \tag{34}$$

Violation of (34) results in starting solutions that yield fluctuating temperatures and melt-line velocities.

This condition of course will not arise from the use of a constant wall temperature at the inner radius. The problem solution with this boundary condition can be attained by the method outlined in Appendix II, or by the use of convection with a very high value for the heat-transfer coefficient, in which case (34) would again have to be satisfied and result in an extremely small time-step.

4. RESULTS AND CONCLUSIONS

The following representative program outputs were generated from the thermal property data of two types of phase-change materials currently under investigation, namely, salts and metal alloys. The purpose of this is twofold: first, to provide usable data concerning each PCM, and second, to emphasize the ability of the present program in contrasting several PCM's to determine their applicability. A Burroughs Corporation B-7700 series computer was utilized to illustrate the behavior of three chosen PCM's, the thermal properties of which appear in Table 1. The heat-exchanger system is similar in function to that used in [15] where a workable configuration was developed for use in a Solar Brayton Power Plant concept, and its dimensions appear in Table 2, where an effort was made to contrast the materials by choosing equal governing parameters (e.g. constant h and constant temperature difference between the melting and inlet convecting temperatures). The assumptions used in producing the results are listed in Table 3, where only 1 through 4 are required by the foregoing analysis.

Figures 5 - 7 depict the melt-line locations within the heat-exchanger at different times, for the salt and metal-alloy PCM's. Actually, each interface location represents a contour surrounding the internally-convected pipe, so that in effect the three-dimensional shape of the melt-line resembles a cone in Figure 5, or a trumpet end in Figures 6 & 7. Due to the higher conductivity of the alloys, more heat is convected within the upstream pipe sections than that by the salt, hence, the contours are more curved. The slight curving of the fusion fronts with time in Figure 5 is attributable to the decreasing fluid temperatures within the downstream pipe section; as less heat is conducted into the upstream sections, its temperature rise is smaller. The lower thermal conductivity of the salt yields an expected increase in the time required for solidification. The similarity of the metal alloys is reflected in the similar interface shapes, with the Mg-Si alloy requiring more time

PCM	Latent Heat (kj/kg.)	Specific Heat (kj/kg/°C)	Thermal Conductivity (w/m/°C)	Density (kg/m^3)	Melting Temperature (°C)
Salt $7CaF_2$ - 54KF - 39NaF	598.0	.80	4.3	2,339.0	640.0
Metal Alloy Al-Si	515.0	.87	75.0	2,250.0	579.0
Metal Alloy Mg-Si	1,212.0	.87	75.0	2,000.0	947.0

Table 1. Thermal property data for three representative phase-change materials.

H/X inner radius (cm.)	- 2.5
H/X outer radius (cm.)	- 8.0
H/X length (cm.)	- 20.0
Working fluid	- Helium
Working fluid specific heat (kj./kg.-°C)	- 5.2
Mass flow rate (gr./sec.)	- 15.0
Heat transfer coefficient (w/m^2-°C)	- 5454.5
Initial superheat (°C)	- T_M + 10°C
Working fluid temperature (°C)	- T_M - 140°C

Table 2. Heat exchanger data.

1. Neglect natural convection
2. Constant melting temperature
3. Density is a constant in both phases
4. Neglect axial conduction within PCM and working fluid
5. Constant material properties
6. PCM initially superheated
7. No crystallization at interface
8. Heat convection at inner radius
9. Insulated outer radius
10. Linear bulk-temperature distribution within each pipe section
11. Neglect pipe thermal capacity
12. Constant heat-transfer coefficient and inlet fluid temperature

Table 3. Assumptions used to generate results in Figures 5 - 12.

to solidify due to its higher latent heat of fusion. Due to the small time step (high h value required from (34)) the melt-line propagation only up to about 5 cm. was plotted to facilitate computer generation of the results; however with greater access to com-

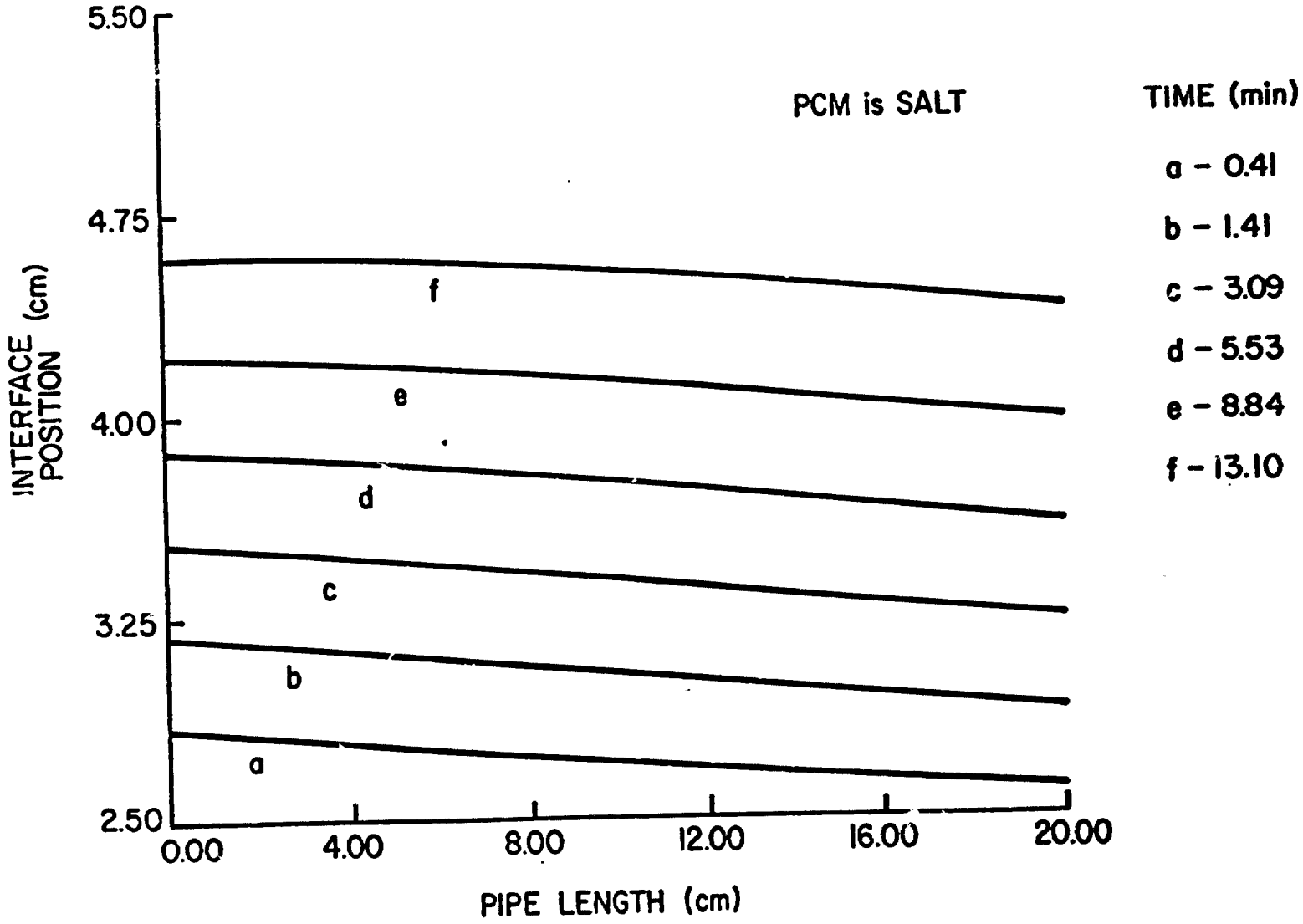

Figure 5. Melt-line location at six different times within the heat exchanger for the salt PCM. (Biot No. = 2537.0)

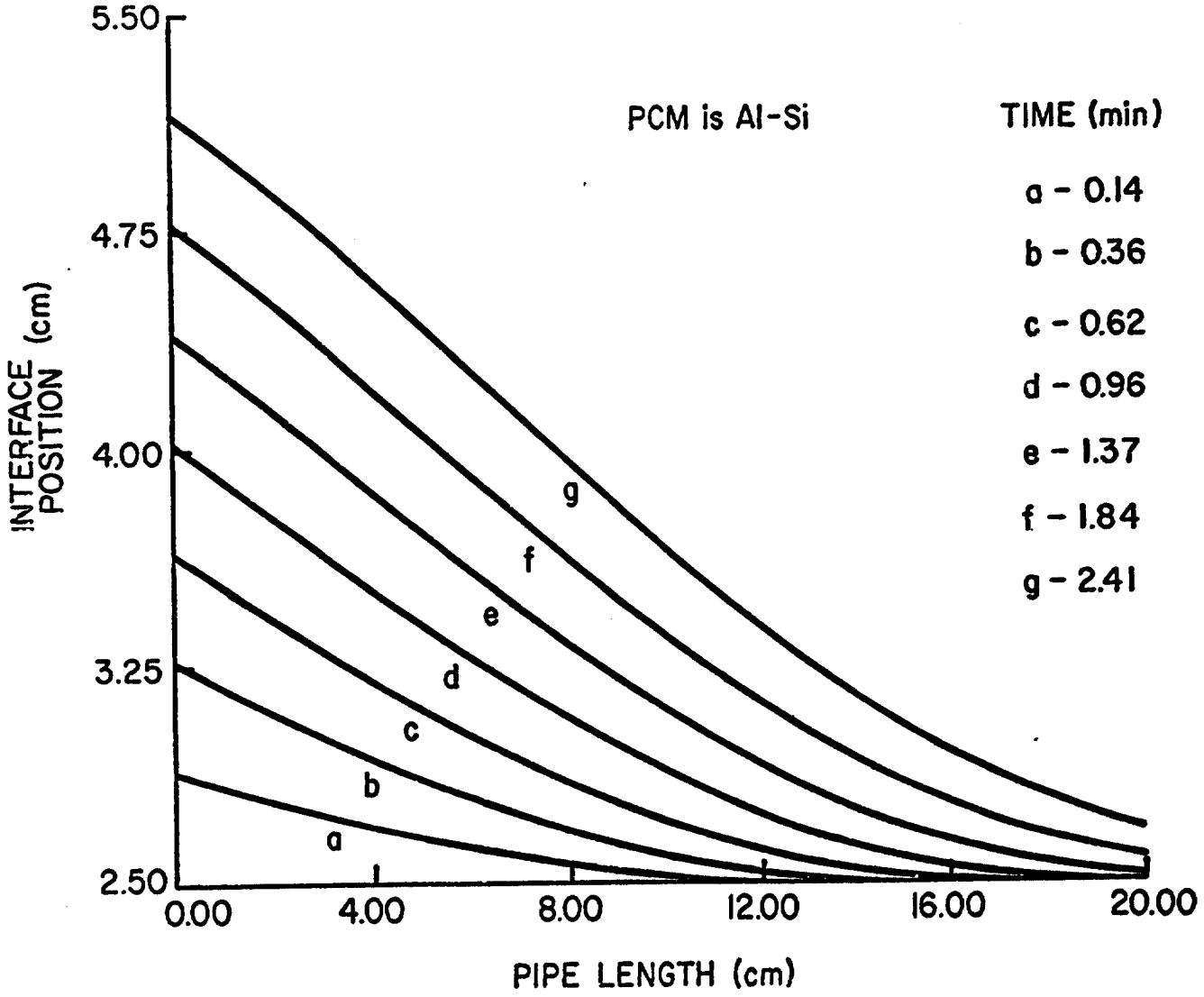

Figure 6. Melt-line location at seven different times within the heat-exchanger for the metal alloy Al-Si. (Biot No. = 145.5)

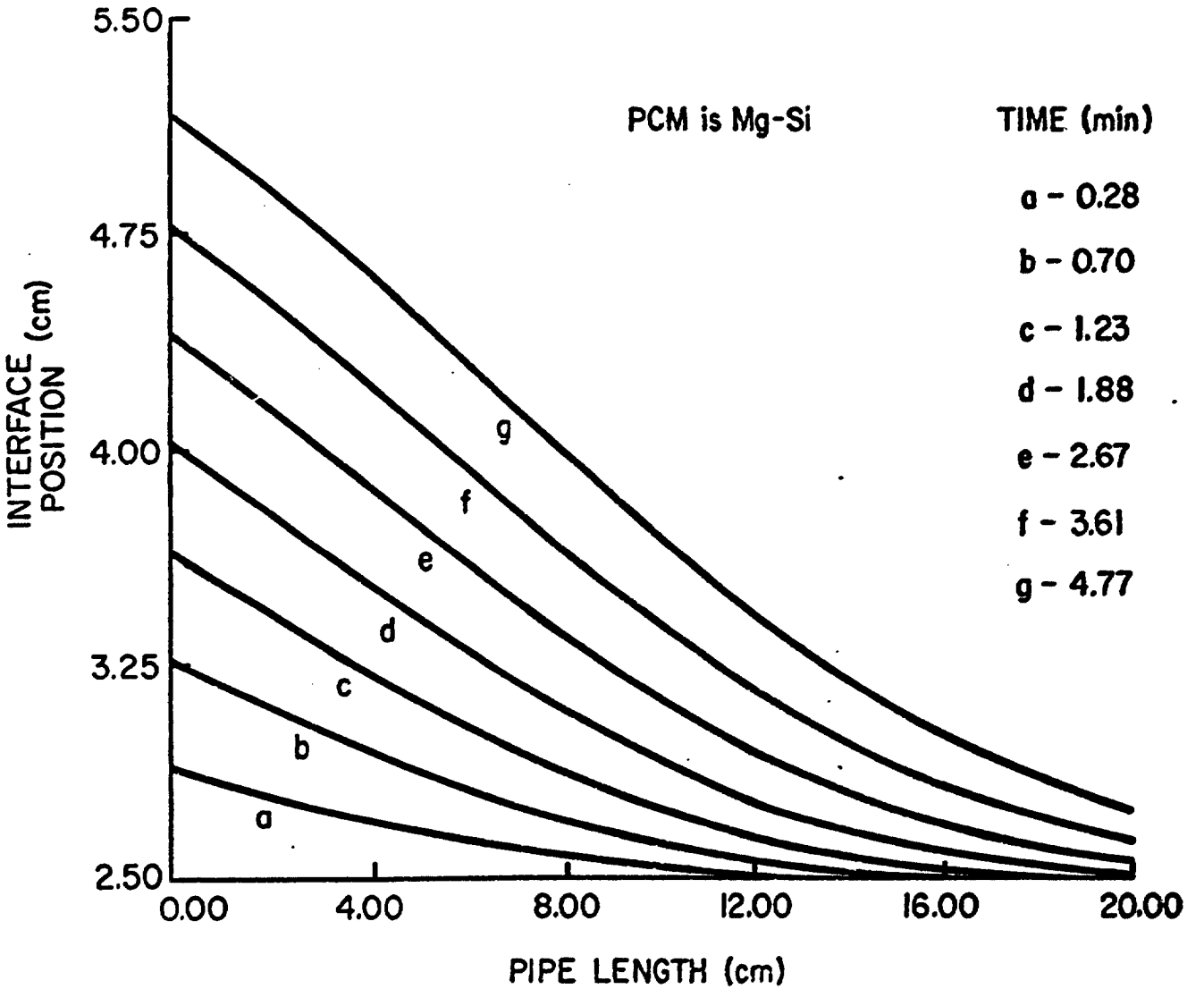

Figure 7. Melt-line location at seven different time within the heat-exchanger for the metal alloy Mg-Si. (Biot No. = 145.5)

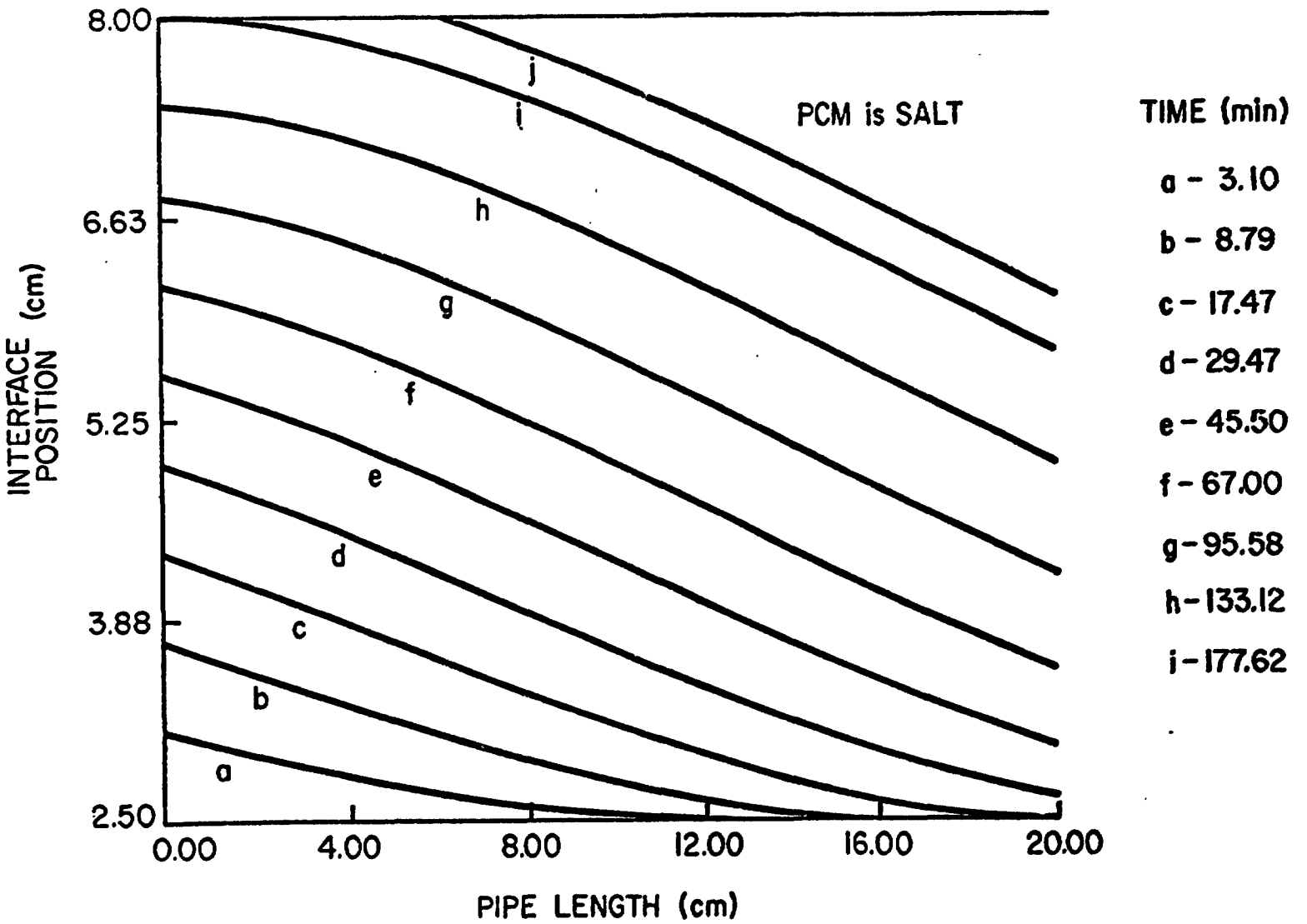

Figure 8. Melt-line location within the heat-exchanger for times up until the salt PCM is almost totally solidified. The heat-transfer coefficient and mass flowrate were reduced to 731 w/m^2-°C and 1.4 gr/sec, respectively, in order to exhibit the melt line propagation along the insulated outer boundary. (Biot No. = 340.4)

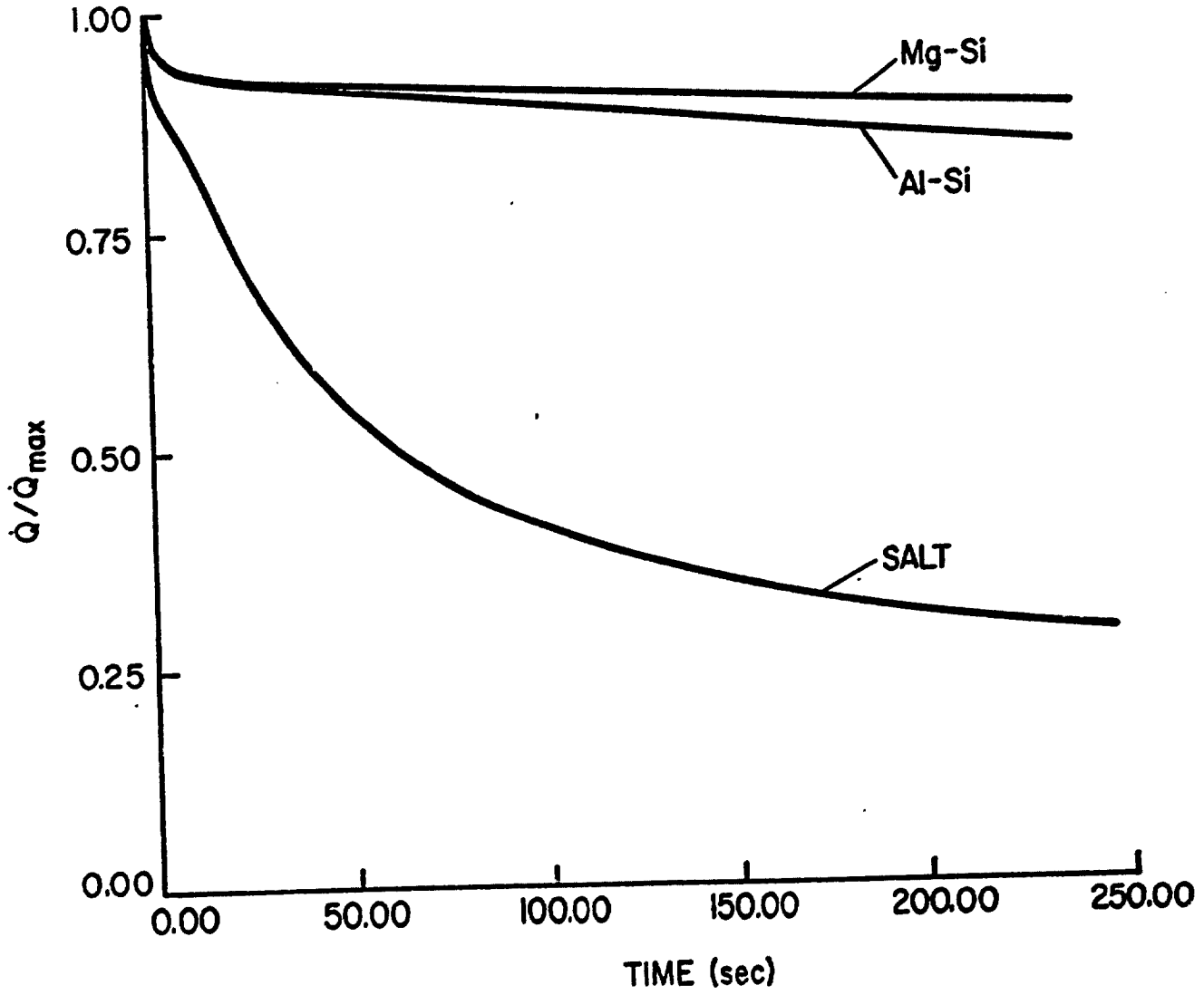

Figure 9. Non-dimensionalized, instantaneous charging rates vs. time (sec.) for the three phase-change materials.

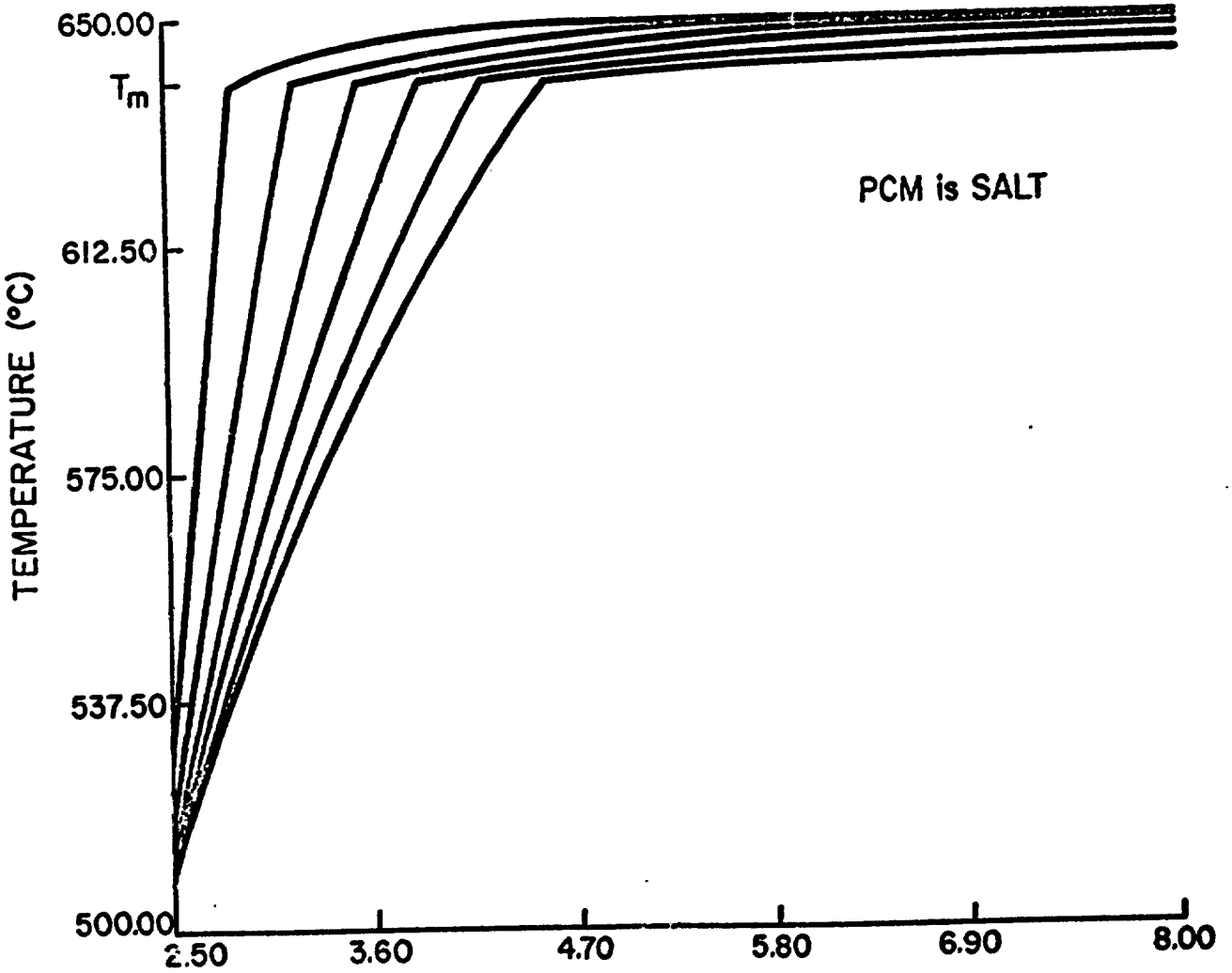

Figure 10. Radial temperature distribution within the first pipe section for different times, using the salt PCM. Times are the same as those in Figure 5.

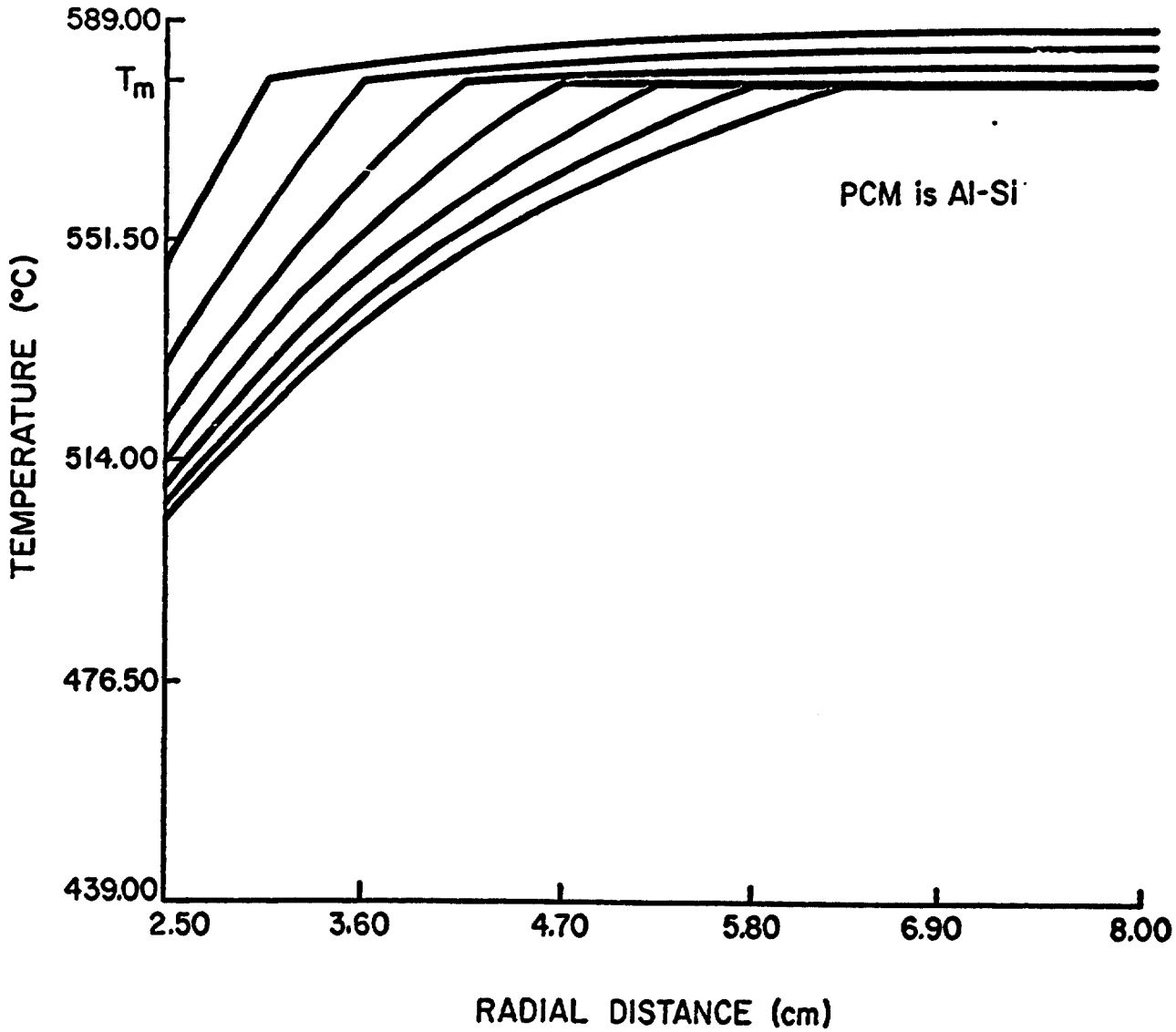

Figure 11. Radial temperature distribution within the first pipe section for different times, using the metal alloy Al-Si. Times are the same as those in Figure 6.

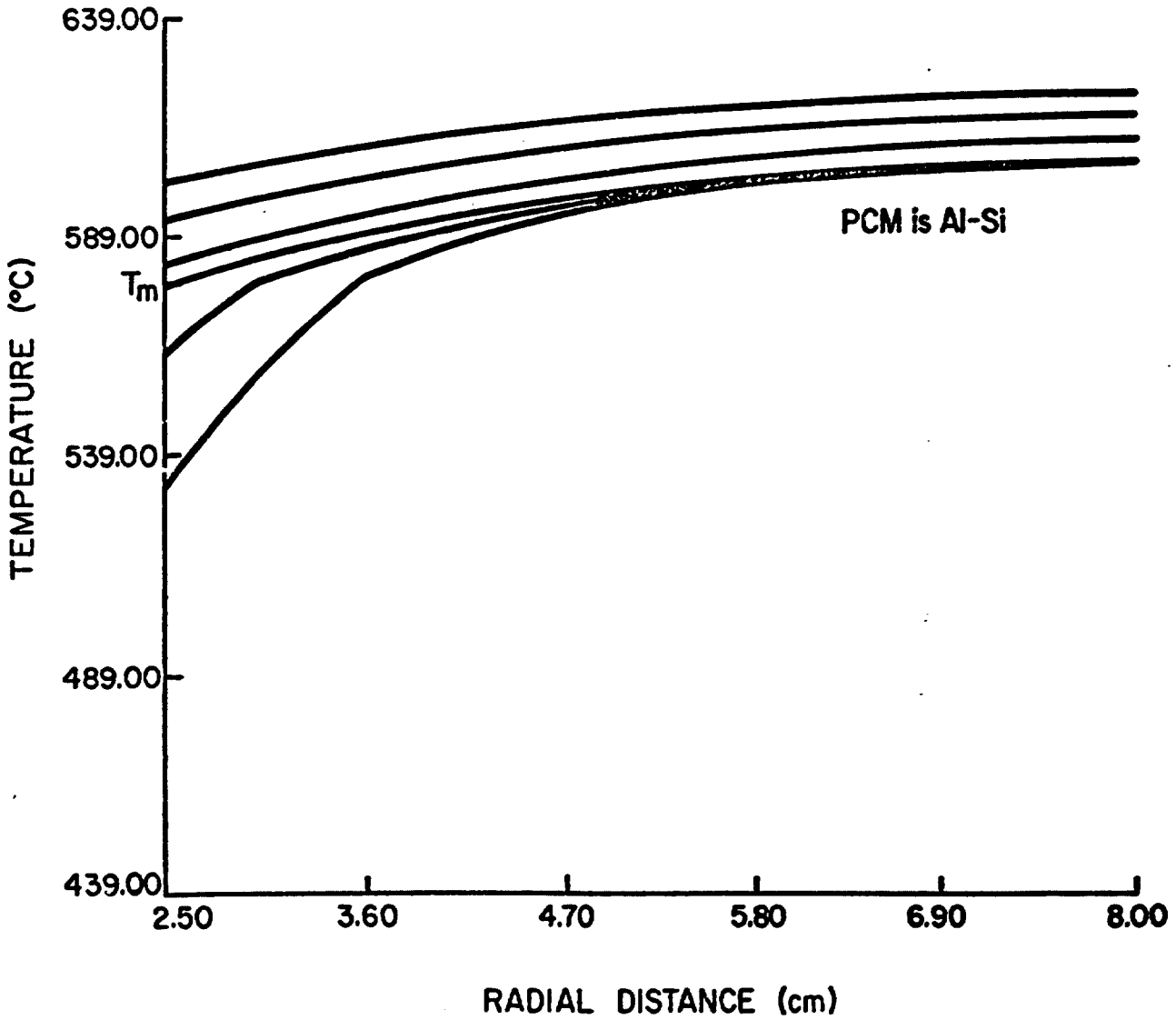

Figure 12. Radial temperature distributions at six locations throughout the heat-exchanger pipe at an intermediate time of 37 seconds, for the metal alloy Al-Si.

puter process time, the entire solidification region is similarly produced. As an example of this, Figure 8 illustrates almost the entire region of the salt PCM being solidified, via the reduction of both the heat-transfer coefficient and mass-flowrate. The interface movement along the insulated boundary is shown, as well as the increase in solidification time. Also of interest, is the effect of mass flowrate on the interface contours. Figures 5 and 8 indicate that the mass flowrate can be reduced to the point where even the salt, with its low thermal conductivity, can transfer much of its energy within the upstream nodes, in a manner similar to that of the metal alloys.

The efficacy of the alloys over the salt in charging a heat storage system is shown in Figure 9 where the area under the curves represents the total energy transferred after a certain time, and is a measure of the effectiveness of the heat exchanger. The values for $\dot{Q}$ are determined by the mass flow rate, $\dot{m}$, specific heat of the fluid, C_f, and the temperature difference between the inlet and outlet fluid temperatures. Of course $\dot{Q}_{max}$ occurs when the temperature difference is the greatest (i.e. initial temperature of the medium minus the inlet fluid temperature).

Figures 10 and 11 exhibit the radial temperatures within the first pipe section at various times, for the salt and Al-Si data respectively. The dissipation of heat with time throughout the superheated region is evident, as well as the temperature non-linearity at the interface. The convecting surface temperature is also depicted as decreasing with time. The fact that the inside surface temperature of the pipe is lower for the salt than the alloy, and not vice versa as one would be lead to believe, is due to the heat convection value chosen for the analysis. Similar to the resistance-network concept, the convection resistance at the wall is greater than that encountered within the alloy medium, but of the same order of magnitude as that within the salt. Hence, the rate-determining step for heat transfer out of the metal alloy, is the convection resistance (unlike the salt), and if this were made smaller (by increasing h) then the surface temperature would decrease. In a sense, the heat-transfer efficiency of the alloys is even greater than that shown. Figure 12 provides an axial composite of radial temperature distributions throughout the partially solidified metal alloy Al-Si at a time of 37 seconds. The inlet and outlet pipe sections are 1 and 11, and every other section is included. The upstream nodes are undergoing solidification, while the downstream sections are approaching the melting temperature.

ACKNOWLEDGEMENTS

The research leading to this publication was funded by NASA via grant NSG 3184. The expertise provided by Professor Ernest C. Birchenall of the University of Delaware, and Mr. Richard Vernon of the NASA Lewis Research Center is gratefully acknowledged, as well as the valuable insight from Mr. Ade Harding, University of Delaware.

REFERENCES

[1] Goodman, T., "The Heat Balance Integral and Its Application to Problems Involving Change of Phase," Trans, Am. Soc. Mech. Eng.

80, 335 (1958).

[2] G. H. Meyer, "Multidimensional Stefan Problems," SIAM J. Numer. Anal., Vol. 10, No. 3, June 1973.

[3] G. Poots, "On the Application of Integral-Methods to the Solution of Problems Involving the Solidification of Liquids Initially at Fusion Temperature," Int. J. Heat Mass Transfer, Vol. 5, 1962, pp. 525-531.

[4] A. D. Solomon, "Melt Time and Heat Flux for a Simple PCM Body," Solar Energy, Vol. 22, 1979, pp. 251-257.

[5] B. A. Boley and J. M. Lederman, "Axisymmetric Melting or Solidification of Circular Cylinders," Int. J. Heat Mass Transfer 13, 413 (1970).

[6] F. Kreith and F. E. Romie, "A Study of the Thermal Diffusion Equation with Boundary Conditions Corresponding to Solidification or Melting of Materials Initially at the Fusion Temperature," Proceedings of the Physics Society, Vol. 68, 1955, p. 277.

[7] L. M. JiJi and S. Weinbaum, "Perturbation Solutions for Melting or Freezing in Annular Regions Initially Not at the Fusion Temperature," Int. J. Heat and Mass Transfer, Vol. 21, 1977, pp. 581-592.

[8] G. S. Shubin, "Analysis of Mass and Heat Transfer Accompanied by Movement of the Phase-Transition Boundary," Heat Transfer-Soviet Research, Vol. 9, No. 1, Jan.-Feb. 1977.

[9] R. Talwar and A. L. Dilpare, "A Two-Dimensional Numerical Solution to Freezing/Melting in Cylindrical Coordinates," ASME Paper No. 77-WA/HT-11, 1977.

[10] C. A. Forster, "Finite-Difference Approach to Some Heat Conduction Problems Involving Change of State," Report of the English Electric Company, Luton, England 1954.

[11] W. D. Murray and F. Landis, "Numerical and Machine Solutions of Transient Heat-Conduction Problems Involving Melting or Freezing," Trans. Am. Soc. Mech. Eng. 81, 106 (1959).

[12] A. Lazaridis, "A Numerical Solution of the Multidimensional Solidification (or Melting) Problem," Int. Journ. Heat Mass Transfer, 13, 1459, (1970).

[13] M. N. Özışık, Heat Conduction, J. Wiley Interscience, (1979).

[14] D. L. Sikarskie and B. A. Boley, "The Solution of a Class of Two-Dimensional Melting and Solidification Problems," Int. J. Solids Struct. 1, 207-234 (1965).

[15] Advanced Thermal Energy Storage (TES) Systems, Boeing Engineering and Construction, Vol. IV, July 1976-December 1976.

[16] A. Harding, Ph.D. Dissertation,(unpub.), Univ. of Delaware,1981

NOMENCLATURE- (non-dimensionalized parameters appear in parenthesis)

A_i	temperature gradient at interface in solid region
B_i	temperature gradient at interface in liquid region
Bi	Biot number, $h\ R/k_1$
C_1	specific heat of solid phase
C_f	specific heat of working fluid
h	heat-transfer coefficient
k_1	thermal conductivity, solid phase
k_2	thermal conductivity, liquid region
K	ratio of k1/k2
L	latent heat of PCM
ℓ	axial length of pipe section
$\dot{m}$	mass flowrate
M	number of pipe sections
N	number of radial nodes
q	node in solid region closest to interface
q+1	node in liquid region closest to interface
R.	reference length
$R_1(\xi_1)$	pipe inner radius
$R_2(\xi_N)$	pipe outer radius
$r(\xi)$	radial coordinate
$R_j(\xi_j)$	radial location of node
$\delta r_i(\delta\xi_i)$	distance between node q and melt-line
$\Delta r(\Delta\xi)$	nodal spacing, $R_2-R_1/N-1$
$S_i(\epsilon_i)$	radial distance to interface
$t(\tau)$	time
$\Delta t(\Delta\tau)$	time increment
T_{fic_i}	fictitious node
T_{f_i}	fluid temperature
T_m	fusion temperature
T_w	wall temperature
$T_{i,j}$	nodal temperature; $1 \leq i \leq M$; $1 \leq j \leq N$
α_1	thermal diffusivity, solid region
α_2	thermal diffusivity, liquid region
ρ	density of PCM
λ	non-dimensionalized parameter, L/C_1
γ	equals γ_ℓ within liquid region; equals 1 within solid region
γ_ℓ	ratio of thermal diffusivities α_2/α_1

APPENDIX I. DETERMINATION OF STABILITY CRITERION

An energy-balance at the convection boundary during the onset of solidification yields,

$$\left.\frac{\partial T}{\partial \xi}\right|_{\xi_1} = Bi(T_1 - T_f) \tag{1}$$

where the subscript "i" has been dropped for simplicity, and (25) provides an expression for $\partial T/\partial \xi \,|_{\xi_1,\ \tau=0}$. Solving for the temperature at the boundary yields

$$T_1 = \frac{4T_2 - T_3 + 2Bi\Delta\xi\ T_f}{3 + 2Bi\Delta\xi} \tag{2}$$

Now after an infinitesimal time step $\Delta\tau$, (2) should also hold for the new values of T_1, T_2 and T_3, denoted by primes as,

$$T_1' = \frac{4T_2' - T_3' + 2Bi\Delta\xi\ T_f}{3 + 2Bi\Delta\xi} \tag{3}$$

but T_2' and T_3' are found from the finite-difference equation (7), as

$$T_2' = T_2\ a + b(T_3 + T_1) + c(T_3 - T_1) \tag{4a}$$

$$T_3' = T_3\ a + b(T_4 + T_2) + c(T_4 - T_2) \tag{4b}$$

where $a = 1 - 2\gamma\Delta\tau/\Delta\xi^2$, $b = \gamma\Delta\tau/\Delta\xi^2$, $c = \Delta\tau\gamma/2\xi\Delta\xi$

Substituting (4a,b) into (3) yields

$$T_1' = 1/d[T_1(4b - 4c) + T_2(4a - b + c) - T_3(a - 4b - 4c) + T_4(-b - c) + 2\Delta\xi BiT_f] \tag{5}$$

where $d = 2\Delta\xi Bi + 3$, and

(5) can be written in simpler form as

$$T_1' = 1/d[\sigma T_1 + \beta T_2 - \eta T_3 - \phi T_4 + \omega] \tag{6}$$

where

$$\sigma = 4\frac{\Delta\tau\gamma}{\Delta\xi}\left(\frac{1}{\Delta\xi} - \frac{1}{2\xi}\right) \tag{7a}$$

$$\beta = 4 - \frac{9\gamma\Delta\tau}{\Delta\xi^2} + \frac{\Delta\tau\gamma}{2\xi\Delta\xi} \tag{7b}$$

$$\eta = 1 - \frac{6\gamma\Delta\tau}{\Delta\xi^2} - \frac{4\Delta\tau\gamma}{2\xi\Delta\xi} \tag{7c}$$

$$\phi = \frac{\gamma\Delta\tau}{\Delta\xi^2} + \frac{\Delta\tau\gamma}{2\xi\Delta\xi} \tag{7d}$$

$$\omega = 2\Delta\xi Bi T_f \tag{7e}$$

The error obtained in (6) is a result of individual errors in all the computed temperatures, hence

$$\Delta T_1' = [\sigma\Delta T_1 + \beta\Delta T_2 - \eta\Delta T_3 - \phi\Delta T_4]/d \tag{8}$$

and the maximum error obtainable from (8) occurs when all the temperature errors have the same sign, hence,

$$\Delta T_{1\,max}' \equiv \delta_1 = [|\sigma||\Delta T_1| + |\beta||\Delta T_2| + |\eta||\Delta T_3| + |\phi||\Delta T_4|]/d \tag{9}$$

Since the temperature T_1 changes the most due to the heat convection at the boundary, its error should be the largest of all associated errors, hence,

$$\Delta T_{1\,max}' = \delta_1' \leq \delta_1/d\ [|\sigma| + |\beta| + |\eta| + |\phi|] \tag{10}$$

If δ_1' in (10) is less than the right hand side of the equation, then the successive values of T_1' at later times is assured to contain an error converging to zero, and in a sense a bound is determined

for the maximum tolerable error used in the finite-difference equations. From (7d) ϕ is always positive, and (7a) contains the second stability criterion where $\Delta\xi << 2\xi_1$ so α is always positive. Thus (10) alters to

$$\delta_1' \leq \delta_1/d \, [\sigma + \phi + |\beta| + |\eta|] \tag{11}$$

and stability is achieved when $\delta_1' < \delta_1$ which implies

$$\sigma + \phi + |\beta| + |\eta| < d \tag{12}$$

Rewriting (7) with $v = \Delta\tau\gamma/\Delta\xi^2$ yields

$$\sigma = 4v[1 - \frac{\Delta\xi}{2\xi}] \tag{13a}$$

$$\beta = 4 - 9v + \frac{v\Delta\xi}{2\xi} \tag{13b}$$

$$\eta = 1 - 6v - \frac{2\Delta\xi v}{\xi} \tag{13c}$$

$$\phi = v + \frac{v\Delta\xi}{2\xi} \tag{13d}$$

Case 1. η is positive, which implies $v(6 + 2\Delta\xi/\xi) < 1$ or $v < 1/6$ in which case then β is surely positive and (12) is then simplified to

$$1 - 5v < \Delta\xi Bi \text{ or } \Delta\xi Bi > 1 \tag{14}$$

which would satisfy the above criteria.

Case 2. β is positive, which implies $v < 4/9$, hence the absolute value of η would be $6v + 2\Delta\xi v/\xi - 1$. After plugging into (12) and simplifying, this leads to $v \leq \Delta\xi Bi$ which is satisfied also by $Bi\Delta\xi > 1$.

APPENDIX II. CONSTANT WALL TEMPERATURE ANALYSIS

The constant-wall temperature boundary condition represents a more complicated and paradoxical condition for use in phase-change problem initiation where the medium is initially at a temperature different from the fusion temperature (i.e. superheated). Essentially, this condition states that at time equal to zero, the wall temperature is at a temperature below the fusion point. This ignores that fact that the wall temperature is actually at the initial temperature at $\tau = 0$, and also that a finite amount of time is required to reduce it to the melting temperature, while also allowing a non-constant temperature distribution to establish within the superheated region. Thus, any attempt to model such a process is at best, an approximation to an unrealistic condition.

One approach is to choose an initial time step significantly smaller than the one computed from Equation 8, Section 3.1, and perform an energy-balance on the small volume of material undergoing phase-change during that time increment.

$$\left(\frac{k_1 A(T_m - T_w)}{\delta r}\right) \Delta\tau = \rho A \delta r \left(L + C_1(T_{initial} - T_m)\right) \qquad (1)$$

and the non-dimensional distance $\delta\xi$ is solved from (1) as

$$\delta\xi = \frac{\delta r}{R} = \frac{1}{R}\left(\frac{k_1(T_m - T_w)}{\rho L + \rho C_1(T_{initial} - T_m)}\right)^{1/2}$$

where the cylindrical volume effects are considered negligible for such a thin ring of material. Following the establishment of an initial $\delta\xi$, the remaining procedure is similar to that of sections 3.1 to 3.3, with the simplification that $T_{i,q-1}$ in Equation (15), Section 3.2 for $i = 2$ (or $T_{i,q}$ when the interface is between the first two nodes) is known as the constant T_w. Lastly, had the initial temperature distribution been something other than a constant, such as a quadratic or parabolic, the starting solution outlined in 3.4 would apply just as well, and obviate the inherent difficulty in determining the solid temperature gradients, A_i, first.

APPENDIX F

HEAT TRANSFER OF PHASE-CHANGE MATERIALS IN TWO-DIMENSIONAL CYLINDRICAL COORDINATES

Michael B. Labdon
Graduate Student

Selçuk İ. Güçeri
Assistant Professor

Mechanical and Aerospace Engineering Department
University of Delaware
Newark, DE 19711 U.S.A.

INTRODUCTION

Materials which undergo a change of phase are being intensely researched for applications in the fields of Thermal Energy Storage and Transfer. The high energy-density and desirable thermal characteristics of these phase-change materials (PCM's) make them attractive candidates for use in such areas as solar energy collection and peak-load leveling [20]. Along with this increased interest in PCM's is the need for accurate modeling of the thermal behavior of such materials. Due to the inherent temperature nonlinearity at the melt-line, the analytical solutions available for solving the phase-change process are relatively few in number, and require restrictive boundary or initial conditions [1-8]. The numerical approaches alternately employed for the problem solution, although somewhat more applicable, also require restrictive conditions which many times reduces the analysis to that of a pseudophase-change process far removed from the actual system itself. Extension to two-dimensional cyclindrical coordinates further reduces the number of available solutions in the literature [9-15]. Talwar and Dilpare [9] appears to be the first attempt at modeling such a phase-change problem.

The method presented in this paper evolved from that initially posited by Forster [10], refined by Murray [11], and subsequently utilized by Lazaridis [12], resulting in a complicated routine difficult to implement in cylindrical coordinates. The feasibility of this solution was shown by Farouk [19], but the required clarification and inherent simplicity was demonstrated by Harding [16] and Labdon [17].

The proposed solution method represents an efficient numerical routine for modeling two-dimensional heat conduction (axial and radial) within an annulus of phase-change material. Finite-difference equations monitor the heat conduction in the regions away from the interface, while truncated Taylor-series expansions of temperature are made near the interface, so as to couple the thermal behavior between the solid and liquid regions. In this manner, the exact melt-line locations and temperature histories are continually determined as the

interface propagates throughout the medium. Inputs include time and spatial-dependent boundary conditions, temperature-dependent properties and initial temperature distributions, while outputs include interface positions and temperature distributions as functions of time.

PROBLEM STATEMENT

The cylindrical geometry under consideration is depicted in Figures 1 and 2. Figure 1 is an axial view of a hollow cylinder of length 'ℓ', containing a PCM partitioned into 'N' equal-thickness, concentric, annular regions or nodes, showing a particular melt-line location. For the following analysis, heat convection is imposed on the inner cylinder R_1, while two-dimensional solidification occurs radially outward toward the insulated boundary R_2.

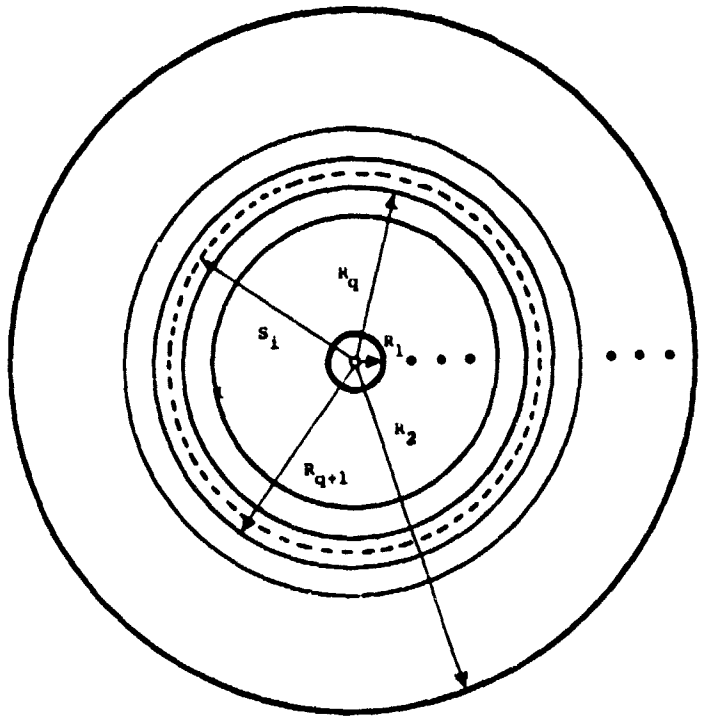

Figure 1. Axial view of the cylinder with representative concentric rings (nodes) of PCM, depicting a particular melt-line location.

The concatenation of 'M' cylinder sections results in a heat exchanger of desired length 'd', as illustrated in Figure 2. An energy balance is performed upon the bulk-temperature of the

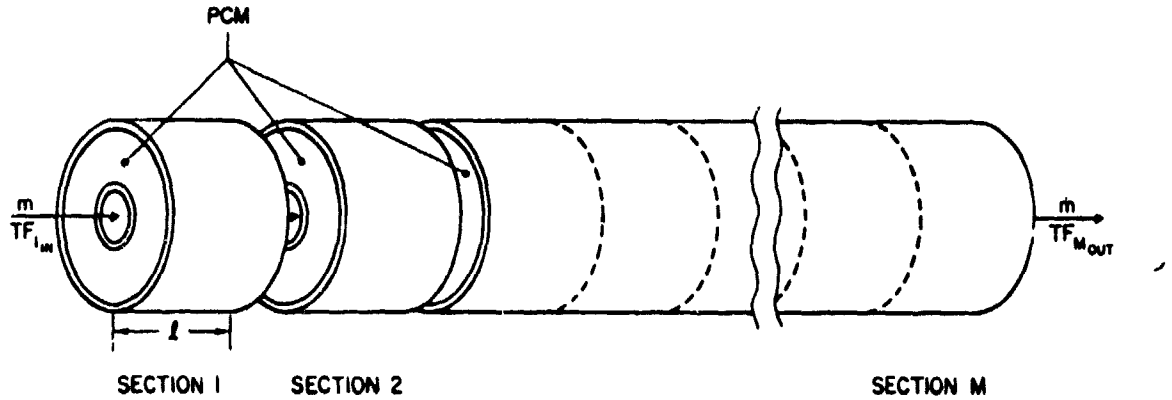

Figure 2. Horizontal view of the hollow cylinder of length 'd', where $d = M\ell$, containing a PCM between an internally convected pipe and an insulated outer one.

convecting fluid as it travels through each cylinder section. In this manner, the melt-line contour is continually traced throughout the phase-change medium, as illustrated in Figure 3, which also shows the two-dimensional mesh network.

PROBLEM SOLUTION

The basic assumptions for the analysis are that the fusion temperature is constant, no crystallization occurs at the interface, the density is constant in both phases and that natural convection effects are neglected. The governing equations and conditions used throughout the medium are:

$$\frac{\partial^2 T_k}{\partial r^2} + \frac{\partial^2 T_k}{\partial z^2} + \frac{1}{r}\frac{\partial T_k}{\partial r} = \frac{1}{\alpha_k}\frac{\partial T_k}{\partial t} \qquad t > 0 \qquad (1,ab)$$

$$\left[k_s \frac{\partial T_s}{\partial r} - k_\ell \frac{\partial T_\ell}{\partial r}\right]\left[1 + \left(\frac{\partial S}{\partial z}\right)^2\right] = L\rho \frac{dS}{dt} \qquad r=S(t),\ t > 0 \qquad (2)$$

$$\frac{\partial T_s}{\partial r} = \frac{h}{k_s}(T_w - T_\infty) \qquad r=R_1,\ t > 0 \qquad (3)$$

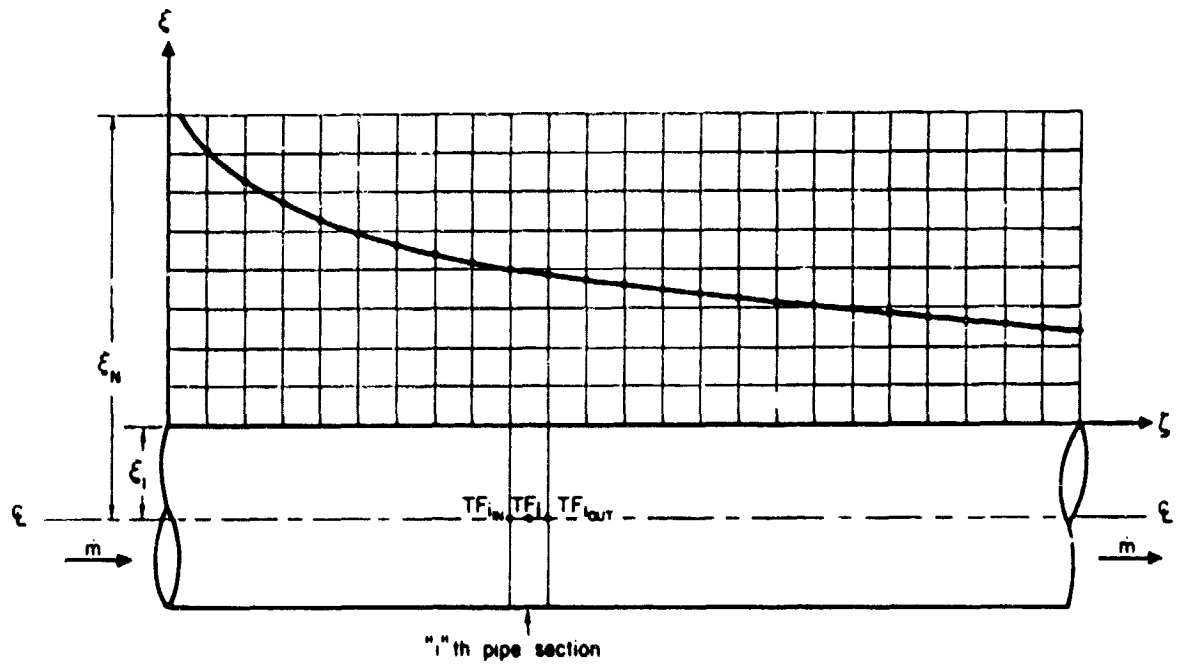

Figure 3. Cross-sectional view of the cylinder with a smooth-line approximation to the 'M+1', radial melt-line locations, and an elemental fluid flow section, at an intermediate time 't'.

$$\left.\frac{\partial T_k}{\partial r}\right|_{R_2} = \left.\frac{\partial T_k}{\partial z}\right|_{z=0} = \left.\frac{\partial T_k}{\partial z}\right|_{z=d} = 0 \qquad (4)$$

$$T = T_m \qquad r=S(t) \qquad (5)$$

$$T_\ell = T_\ell\,(z,r) \qquad t = 0 \qquad (6)$$

where k = s or ℓ depending upon the solid or liquid region. The following non-dimensionalizing parameters are introduced into the above equation,

$$\xi \equiv r/R \;;\; \tau \equiv \alpha_s\, t/R^2 \;;\; \varepsilon(\tau) \equiv S(t)/R \;;\; \Delta\xi \equiv \Delta r/R \;;\; K \equiv k_\ell/k_s$$

$$\gamma_\ell \equiv \alpha_\ell/\alpha_s \;;\; \lambda \equiv L/C_s \;;\; \delta\xi \equiv \delta r/R \;;\; \xi_1 \equiv R_1 \;;\; \xi_N \equiv R_2\; \zeta \equiv z/R$$

(where R is a chosen reference length) generating the following equation in which all variables but temperature are non-dimensionalized:

$$\frac{\partial^2 T_k}{\partial \zeta^2} + \frac{\partial^2 T_k}{\partial \xi^2} + \frac{1}{\xi}\frac{\partial T_k}{\partial \xi} = \frac{1}{\gamma}\frac{\partial T_k}{\partial \tau} \qquad \begin{matrix}\xi_1 \le \xi \le \varepsilon,\ k = s \\ \varepsilon \le \xi \le \xi_N,\ k = \ell\end{matrix} \qquad (7a,b)$$

$$\left[1 + \left(\frac{\partial \varepsilon}{\partial \zeta}\right)^2\right]\left[\frac{\partial T_s}{\partial \xi} - K\,\frac{\partial T_\ell}{\partial \xi}\right] = \lambda\,\frac{d\varepsilon}{d\tau} \qquad \xi = \varepsilon(\tau) \qquad (8)$$

$$\frac{\partial T_s}{\partial \xi} = Bi\,(T_w - T_f) \qquad \xi = \xi_1\ ,\ \tau > 0 \qquad (9)$$

$$\left.\frac{\partial T_k}{\partial \xi}\right|_{\xi_N} = \left.\frac{\partial T_k}{\partial \zeta}\right|_{\zeta=0} = \left.\frac{\partial T_k}{\partial \zeta}\right|_{\zeta=d} = 0 \qquad \tau > 0 \qquad (10)$$

$$T = T_m \quad \xi = \varepsilon(\tau)\ ;\ T_\ell = T_\ell(\zeta,\xi) \qquad \tau = 0 \qquad (11,12)$$

Method 1 - One-Dimensional Taylor Series Expansion

Figure 4 describes the temperature distribution within the interface region for a particular cylinder section. The axial temperature distributions in the ± ζ direction (not shown) account for the two-dimensional movement of the interface. At this point, all that is known are the 'current' melt-line locations at time τ, and the 'old' nodal temperatures at time τ-Δτ. The object of the method is to determine the current nodal temperatures and new melt-line velocity, which requires the successful execution of the following computational logic:

Step 1 - Determine Melt-Line Slopes. The more arduous task of monitoring fusion-front propagation along two orthogonal directions is superseded by the method of determining the radial projection of the normal velocity gradient, shown graphically in Figure 5. The mathematical derivation of this procedure appears in [13], the result of which is a factor $\left[1 + \left(\frac{\partial \varepsilon}{\partial \zeta}\right)^2\right] \equiv \beta^2$ to be multiplied by the normal gradient, that allows continuous monitoring of the melt-line gradient in the radial direction. The term $\frac{\partial \varepsilon}{\partial \zeta}$ represents the slope of the melt-line in the ζ direction, and is determined at each 'i' location as $(\varepsilon_{i+1}-\varepsilon_{i-1})/(2\Delta\zeta)$.

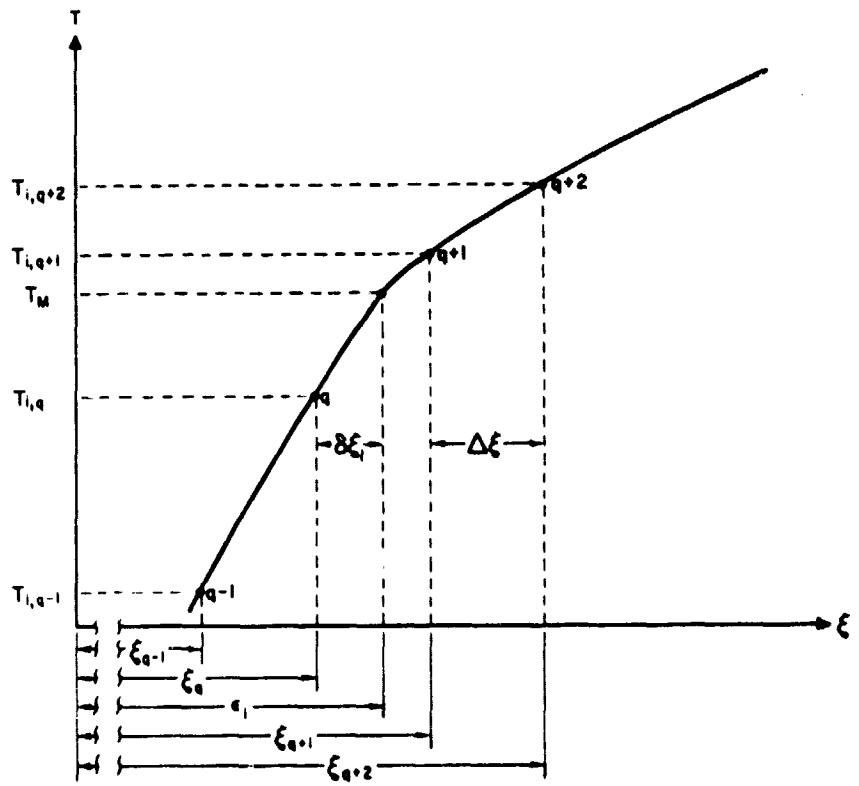

Figure 4. Radial temperature distribution near the interface, within a particular pipe section.

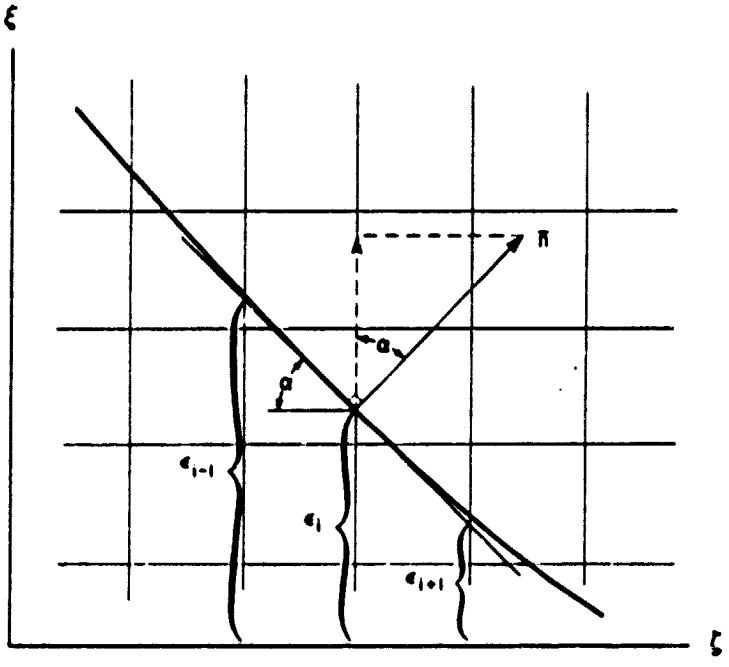

Figure 5. Particular melt-line location depicting radial projection of normal directional gradient, and distances used for localized melt-line slope determination.

Step 2 - Nodal Temperatures. The current nodal temperatures $T_{i,j}$ where $1 \leq i \leq M$; $1 \leq j \leq q-1$ and $q+2 \leq j \leq N$ are computed via the finite-difference equation

$$T'_{i,j} = T_{i,j}\left(1 - \frac{2\gamma\Delta\tau}{\Delta\xi^2} - \frac{2\gamma\Delta\tau}{\Delta\zeta^2}\right) + \frac{\gamma\Delta\tau}{\Delta\zeta^2}\left(T_{i+1,j} + T_{i-1,j}\right) + \frac{\gamma\Delta\tau}{2\xi\Delta\xi}\left(T_{i,j+1} - T_{i,j-1}\right) + \frac{\gamma\Delta\tau}{\Delta\xi^2}\left(T_{i,j+1} + T_{i,j-1}\right) \quad (13)$$

with an associated time stability criterion,

$$\Delta\tau \leq \frac{1}{2\gamma}\left(\frac{1}{\Delta\xi^2} + \frac{1}{\Delta\zeta^2} - \frac{Bi}{2\xi} + \frac{Bi}{\Delta\xi}\right)^{-1} \quad (14)$$

determined from the convection boundary [18].

Step 3 - Determine Axial Temperatures and Gradients. The four axial, inter-node temperatures shown in Figure 6 (dashed circles) are required (at each ε_i location) for determining temperature gradients and second-derivatives at the melt-line. Each temperature is interpolated from a three-point distribution determined from the radial temperature profiles originating from the interface (solid circles). Using these inter-node temperatures and the melting temperature, two quadratic profiles in the form

$$T(\zeta) = a + b\zeta + c\zeta^2 \qquad (15)$$

are utilized, both of which originate at the interface and extend in the $\pm\ \zeta$ directions (horizontal dashed ellipsis of Figure 6). The two second derivatives of temperature in the axial direction and then determined at the melt-line from (15) and are referred to as Z''_s, Z''_ℓ.

Step 4 - Determine Radial Temperature Gradients. Radial Taylor-series expansions of temperature are then applied from each melt-line location ε_i in the $\pm\ \xi$ directions (vertical dashed ellipsis of Figure 6) to the known value of nodal temperature $T_{i,q-1}$ and $T_{i,q+2}$, in the form:

$$T_k(\varepsilon) = T_k\Big|_{\varepsilon_i} + (\xi - \varepsilon_i)\frac{\partial T_k}{\partial \xi}\Big|_{\varepsilon_i} + \frac{(\xi - \varepsilon_i)^2}{2}\frac{\partial^2 T_k}{\partial \xi^2}\Big|_{\varepsilon_i} \qquad (16a,b)$$

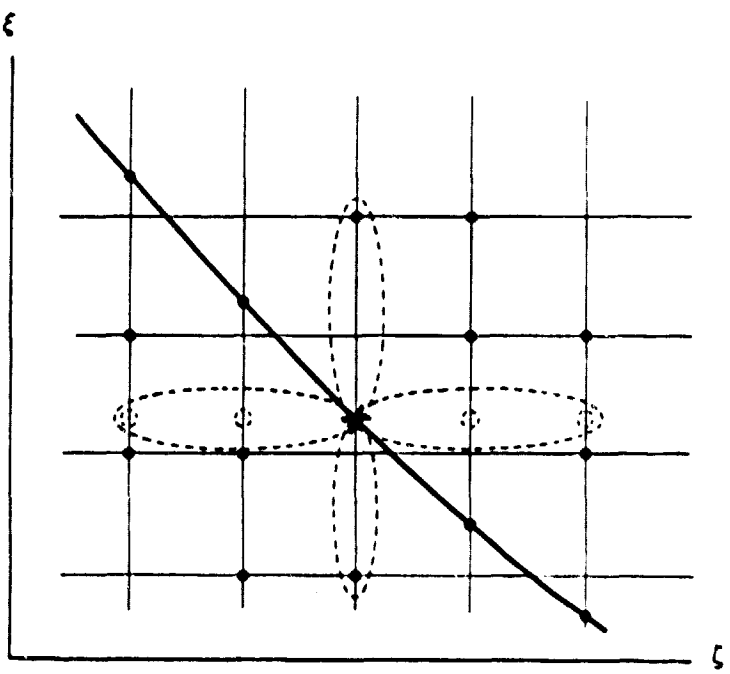

Figure 6. Local temperatures and distributions required for temperature derivative calculations at a particular melt-line location.

In addition, (17) applies at the interface

$$\left.\frac{dT_k}{d\tau}\right|_{\varepsilon_i} = 0 = \left.\frac{\partial T_k}{\partial \tau}\right|_{\varepsilon_i} + \left.\frac{\partial T_k}{\partial \xi}\right|_{\varepsilon_i} \left.\frac{d\varepsilon_i}{d\tau}\right. \beta \qquad (17a,b)$$

The seven equations (7a,b), (8), (16a,b), (17a,b) are then combined in a manner similar to that of [18] to solve for the seven unknowns, namely, the two second derivatives of temperature, the two radial temperature gradients, the two time derivatives of temperature, and the melt-line velocity, all of which are applied at the current interface location. The resulting two equations are coupled in the unknowns $\left.\frac{\partial T_s}{\partial \xi}\right|_{\varepsilon_i}$ and $\left.\frac{\partial T_\ell}{\partial \xi}\right|_{\varepsilon_i}$ defined as A_i and B_i,

$$A_i^2\beta^3 + A_i\left(\frac{\lambda}{\varepsilon_i} + \frac{2\lambda}{d_1}\right) - A_iB_iK\beta^3 + \frac{2\lambda}{d_1^2}\left(T_{i,q-1} - Tm\right) + Z_s'' = 0 \qquad (18)$$

$$B_i^2\beta^3 + B_i\left(\frac{2\gamma\lambda}{Kd_2} - \frac{\gamma\lambda}{K\varepsilon_i}\right) - \frac{A_iB_i\beta^3}{K} + \frac{2\gamma\lambda}{d_2^2K}\left(T_m - T_{i,q+2}\right) + Z_\ell'' = 0 \qquad (19)$$

Step 5 - Calculate Interface Region Nodal Temperatures. The similarity between (15) and (16) indicates that the Taylor-series expansion of three terms is identical to instituting a quadratic temperature profile, and thus the foregoing analysis of the interface regions assures uniformity throughout the method. At this point, (16) can be used to determine the remaining nodal termperatures $T_{i,q}$ and $T_{i,q+1}$.

Step 6 - Determine New Melt-Front Velocity. Via an analysis in [18] the Stefan condition in cylindrical coordinates (8), which heretofore was appropriately utilized in the mathematical derivations, is interpreted differently for use in a numerical routine. The increase in surface area faced by a radially expanding interface alters (8) by the factor below

$$A_i - KB_i = \lambda\left(\frac{\varepsilon_{\tau+\Delta\tau} - \varepsilon_t}{\Delta\tau}\right)\cdot\left(\frac{\varepsilon_{\tau+\Delta\tau} + \varepsilon_\tau}{2\varepsilon_\tau}\right) \qquad (20)$$

which reduces to unity as the time-discretization parameter $\Delta\tau$ is made smaller.

Method 2 - Two-Dimensional Taylor-Series Expansion

As shown in Figure 7, 2 two-dimensional Taylor-series expansions of temperature are applied at the interface in the $\pm\ \xi$ and $\pm\ \zeta$ directions in the form:

$$T(\zeta,\xi) = T(i,\epsilon_i) + \left.\frac{\partial T}{\partial \zeta}\right|_{\epsilon_i} (\zeta - i) + \left.\frac{\partial T}{\partial \xi}\right|_{\epsilon_i} (\xi - \epsilon_i) + \left.\frac{\partial^2 T}{\partial \zeta^2}\right|_{\epsilon_i} \frac{(\zeta - i)^2}{2}$$

$$+ \left.\frac{\partial^2 T}{\partial \xi^2}\right|_{\epsilon_i} \frac{(\xi - \epsilon_i)^2}{2} + \left.\frac{\partial^2 T}{\partial \xi \partial \zeta}\right|_{\epsilon_i} (\xi - \epsilon_i)(\zeta - i)$$

$$= T_M + a(\zeta - i) + b(\xi - \epsilon_i) + c(\zeta - i)^2 + d(\xi - \epsilon_i)^2 + e(\zeta - i)(\xi - \epsilon_i) \qquad (21)$$

where the constants represent the appropriate gradient or second derivative term in (21), and the terms in parentheses represent

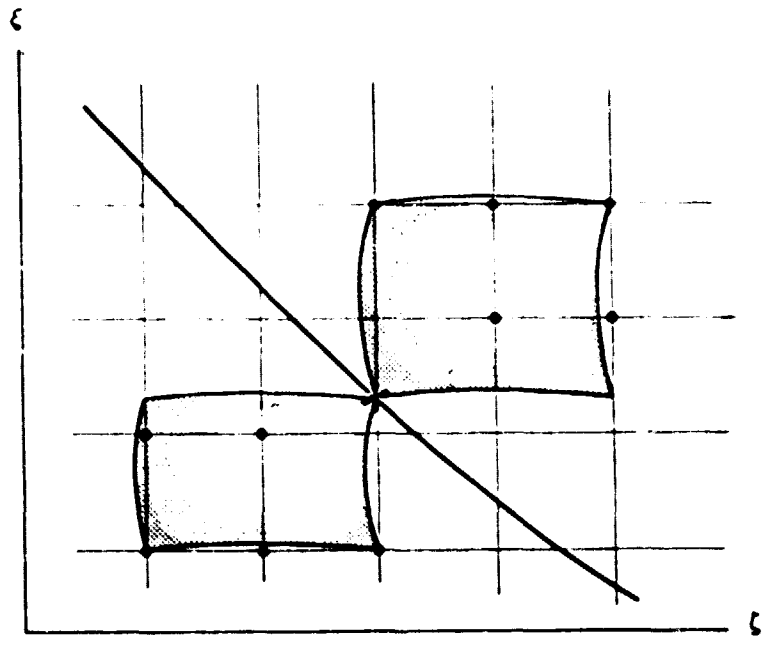

Figure 7. Temperature field surfaces generated from two-dimensional Taylor-series expansions about the interface.

the axial and radial distance to a particular node of known current temperature. Thus, the selection of five known temperatures in the neighborhood of the interface, in both the liquid and solid regions, is sufficient to determine the sought after temperature gradients A_i and B_i in (21). Intuitively, the closer the chosen nodal points to the interface, the more accuracy that would result in generating the two-dimensional surfaces of temperature, and an intricate computer program was utilized to determine the nodes of closest proximity to the interface. Thus, steps 3, 4 and 5 of Method 1 are superseded by the above procedure, which results in decreased computer process times for problem solutions.

Information as to starting and terminating procedures, the fluid energy balance, the melt-line crossing a nodal point, and the use of a constant wall temperature boundary condition can be found in [18]. In particular, the starting procedure requires the following restrictive stability criterion,

$$\frac{h}{k_s} \Delta r > 1.0$$

RESULTS

The following system parameters were chosen to describe the various outputs from the method:

Cylinder inner radius (cm)	- 2.5
Cylinder outer radius (cm)	- 8.0
Cylinder length (cm)	- 20.0
Working fluid	- Helium
Working fluid specific heat (kj/kg-°C)	- 5.2
Mass flow rate (gr/sec)	- 15.0
Heat transfer coefficient (w/m^2-°C)	- 5454.5
Initial superheat (°C)	- T_m + 10
Working fluid temperature (°C)	- T_m - 140

In addition, the following assumptions were used to facilitate data generation only, and are not required by the foregoing analysis:

1. Constant material properties
2. PCM initially superheated
3. Heat convection at inner radius
4. Insulated outer radius
5. Linear bulk-temperature distribution within each pipe section
6. Neglect pipe thermal capacity
7. Constant heat-transfer coefficient and inlet fluid temperature

Figures 8 and 9 depict melt-line contours at various times for the salt PCM $7CaF_2$-54KF-39NaF and the metal alloy PCM Al-Si, respectively. The former, having a lower thermal conductivity, yields the result of relatively straight contours and longer times required for solidification. Figure 9 illustrates the more curved interface shapes due to the greater heat-transfer within the upstream nodes.

Figure 10 contains radial temperatures within the first cylinder section at times corresponding to those in Figure 8 for the salt PCM. The decreasing inner surface temperature and initial superheat with time are evident.

Figure 11 represents an axial composite of several radial temperature distributions within the Al-Si PCM at a time of 20 seconds following the onset of solidification. The upstream sections are undergoing phase-change while the initial superheat is still being dissipated within the downstream ones.

ACKNOWLEDGMENTS

The research leading to this publication was funded by NASA via grant NSG 3184. The expertise provided by Professor Ernest C. Birchenall of the University of Delaware and Mr. Richard Vernon of the NASA Lewis Research Center is gratefully acknowledged.

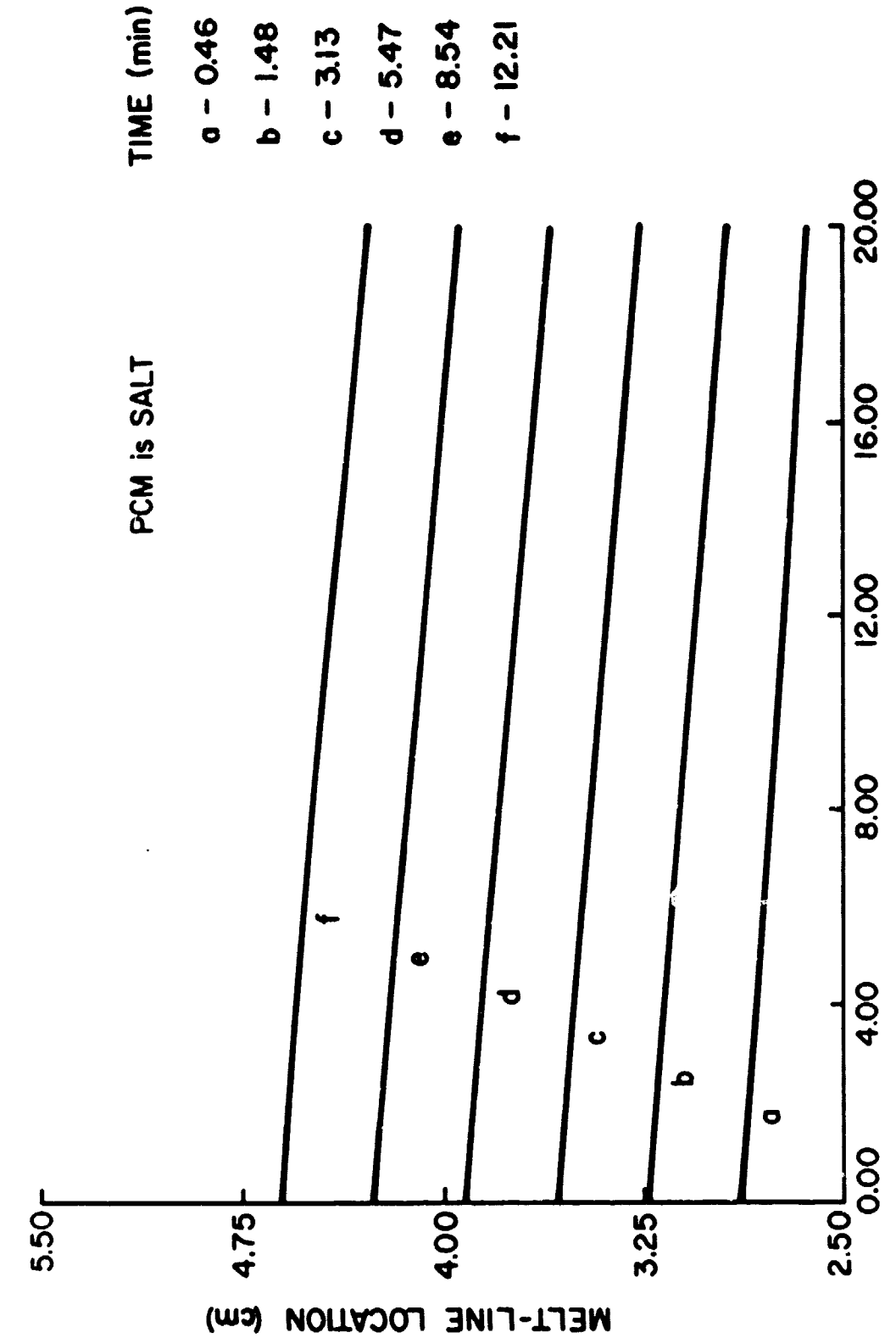

Figure 8 - Melt-line contours at six different times within the annulus for the salt phase-change material $7CaF_2$-54KF-39NaF.

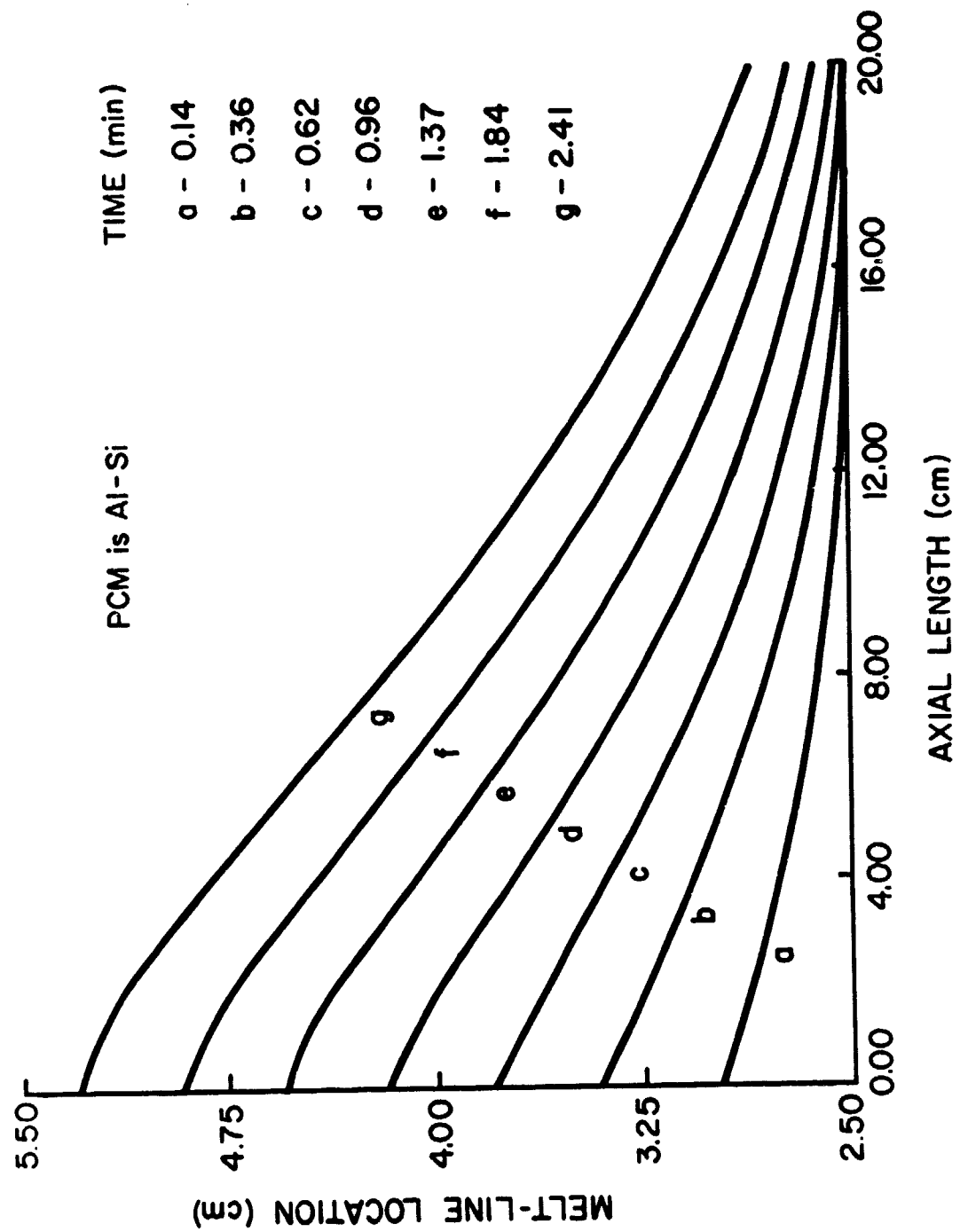

Figure 9 - Melt-line contours at seven different times within the annulus for the metal alloy phase-change material Al-Si.

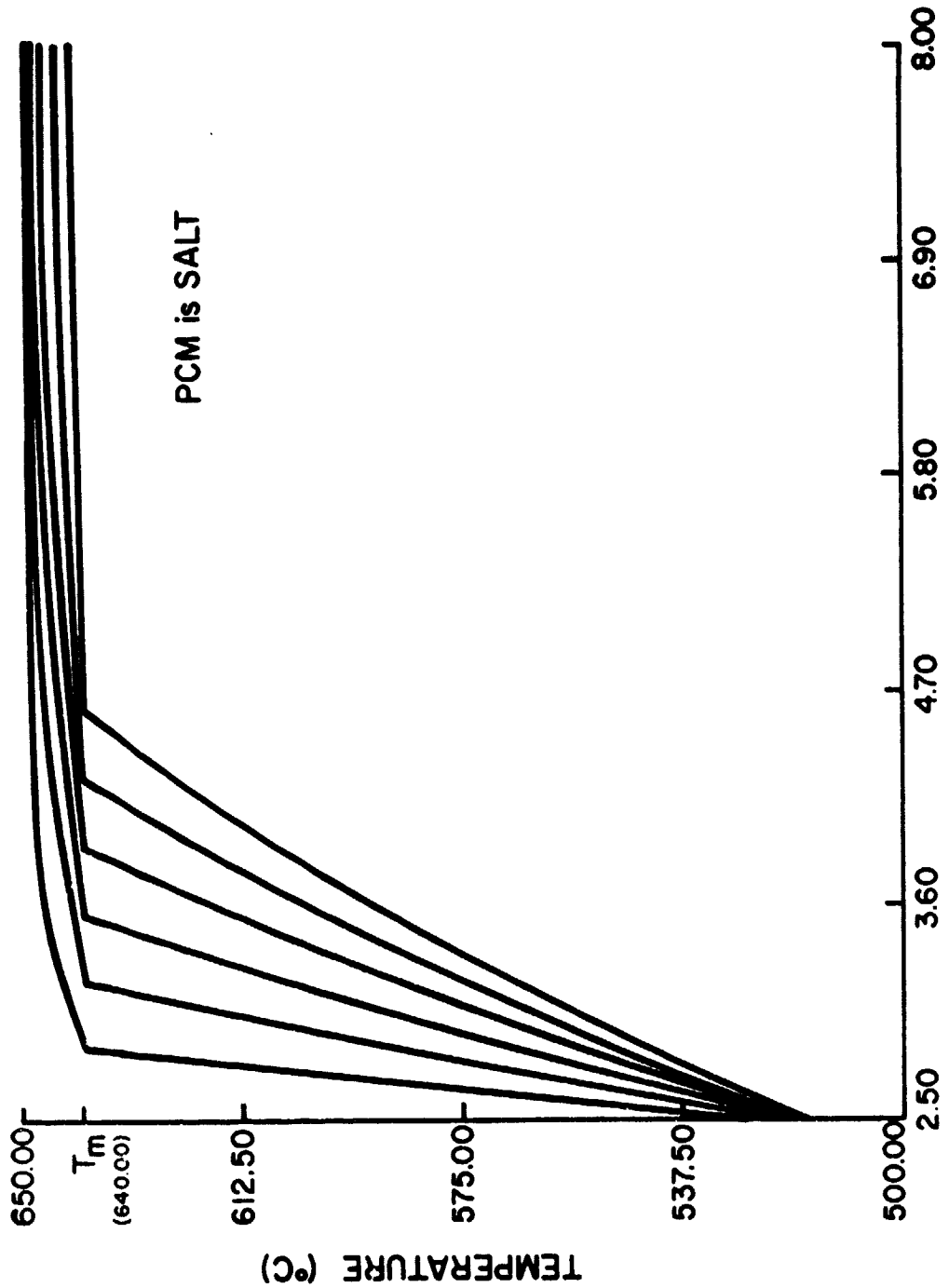

Figure 10 - Radial temperature distributions within the first cylinder section; for the salt PCM, at times corresponding to those of Figure 8.

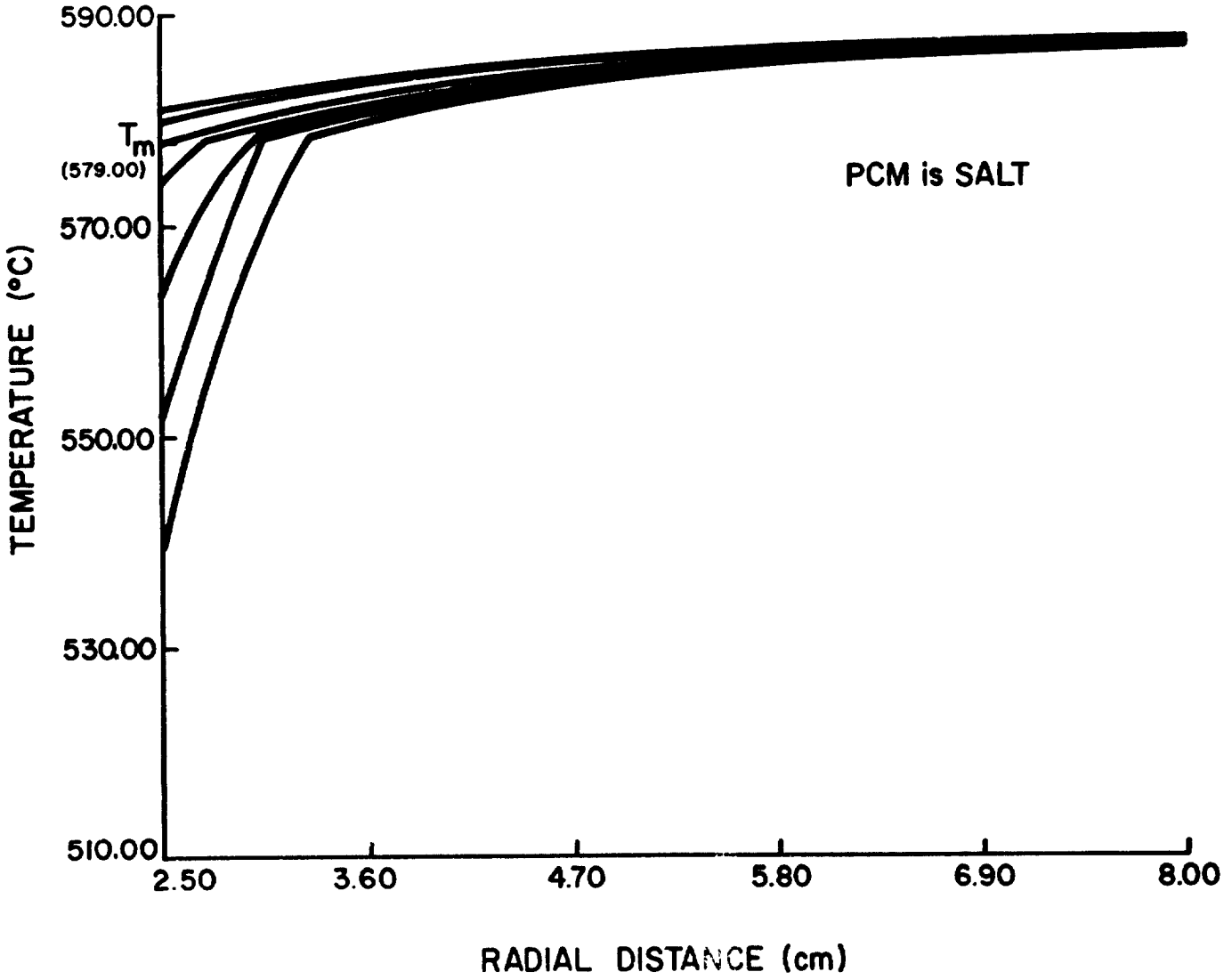

Figure 11 - Axial composite of radial temperature distributions within the cylinder at a time of 20 seconds following the onset of solidification of the metal alloy PCM.

NOMENCLATURE (non-dimensionalized parameters appear in parentheses)

A_i	temperature gradient at interface in solid region
B_i	temperature gradient at interface in liquid region
Bi	Biot number, $h\ R/k_s$
C_l	specific heat of solid phase
C_f	specific heat of working fluid
h	heat-transfer coefficient
k_s	thermal conductivity, solid phase
k_ℓ	thermal conductivity, liquid region
K	ratio of k_ℓ/k_s
L	latent heat of PCM
ℓ	axial length of pipe section
$\dot{m}$	mass flowrate
M	number of pipe sections
N	number of radial nodes
q	node in solid region closest to interface
q+1	node in liquid region closest to interface
R	reference length
$R_1(\xi_1)$	pipe inner radius
$R_2(\xi_N)$	pipe outer radius
$r(\xi)$	radial coordinate
$R_j(\xi_j)$	radial location of node
$\delta r_i(\delta\xi_i)$	distance between node q and melt-line
$\Delta r(\Delta\xi)$	nodal spacing $(R_2-R_1)/(N-1)$
$S_i(\varepsilon_i)$	radial distance to interface

$t(\tau)$	time
$\Delta t(\Delta\tau)$	time increment
T_{f_i}	fluid temperature
T_m	fusion temperature
T_w	wall temperature
$T_{i,j}$	nodal temperature; $1 \leq i \leq M$; $1 \leq j \leq N$
$z(\zeta)$	axial coordinate
Z''_k	second derivatives of temperature in the axial direction evaluated at the interface
d_1	distance from node q to melt-line
d_2	distance from melt-line to node q + 1
α_1	thermal diffusivity, solid region
α_2	thermal diffusivity, liquid region
$\beta^{\frac{1}{2}} = 1 + \left(\frac{\partial s}{\partial z}\right)^2$	which is projection of normal direction onto radial coordinate
ρ	density of PCM
λ	non-dimensionalized parameter, L/C_1
γ	equals γ_ℓ within liquid region; equals 1 within solid region
γ_ℓ	ratio of thermal diffusivities α_2/α_1

REFERENCES

[1] Goodman, T., "The Heat Balance Integral and Its Application to Problems Involving Change of Phase," Trans. Am. Soc. Mech. Eng. 80, 335 (1958).

[2] G. H. Meyer, "Multidimensional Stefan Problems," SIAM J. Numer. Anal., Vol. 10, No. 3, June 1973.

[3] G. Poots, "On the Application of Integral-Methods to the Solution of Problems Involving the Solidification of Liquids Initially at Fusion Temperature," Int. J. Heat Mass Transfer, Vol. 5, 1962, pp. 525-531.

[4] A. D. Solomon, "Melt Time and Heat Flux for a Simple PCM Body," Solar Energy, Vol. 22, 1979, pp. 251-257.

[5] B. A. Boley and J. M. Lederman, "Axisymmetric Melting or Solidification of Circular Cylinders," Int. J. Heat Mass Transfer 13, 413 (1970).

[6] F. Kreith and F. E. Romie, "A Study of the Thermal Diffusion Equation with Boundary Conditions Corresponding to Solidification or Melting of Materials Initially at the Fusion Temperature," Proceedings of the Physics Society, Vol. 68, 1955, p. 277.

[7] L. M. JiJi and S. Weinbaum, "Perturbation Solutions for Melting or Freezing in Annular Regions Initially Not at the Fusion Temperature," Int. J. Heat and Mass Transfer, Vol. 21, 1977, pp. 581-592.

[8] G. S. Shubin, "Analysis of Mass and Heat Transfer Accompanied by Movement of the Phase-Transition Boundary," Heat Transfer-Soviet Research, Vol. 9, No. 1, Jan.-Feb. 1977.

[9] R. Talwar and A. L. Dilpare, "A Two-Dimensional Numerical Solution to Freezing/Melting in Cylindrical Coordinates," ASME Paper No. 77-WA/HT-11, 1977.

[10] C. A. Forster, "Finite-Difference Approach to Some Heat Conduction Problems Involving Change of State," Report of the English Electric Company, Luton, England 1954.

[11] W. D. Murray and F. Landis, "Numerical and Machine Solutions of Transient Heat-Conduction Problems Involving Melting or Freezing," Trans. Am. Soc. Mech. Eng. 81, 106 (1959).

[12] A. Lazaridis, "A Numerical Solution of the Multidimensional Solidification (or Melting) Problem," Int. Journ. Heat Mass Transfer, 13, 1459 (1970).

[13] M. N. Özişik, Heat Conduction, J. Wiley Interscience, (1979), pp. 403-405

[14] D. L. Sikarskie and B. A. Boley, "The Solution of a Class of Two-Dimensional Melting and Solidification Problems," Int. J. Solids Struct. 1, 207-234 (1965).

[15] Advanced Thermal Energy Storage (TES) Systems, Boeing Engineering and Construction, Vol. IV, July 1976 - December 1976.

[16] A. Harding, Ph.D. Dissertation, (unpub.), Univ. of Delaware, 1981.

[17] M. Labdon, Masters Thesis, University of Delaware, Newark, DE, 1981.

[18] M. B. Labdon, S. İ. Güçeri, "Analysis of Cylindrical Heat Exchanger with Phase Change Materials," 3rd Miami Conf. on Alternate Energy Sources, Hemisphere Publishing Co. Dec. 1980.

[19] Farouk, B., "Trombe Michel Wall with Phase Change Materials," 2nd Miami Int. Conf., Dec. 1979.

[20] M. Greeven, "A Solar Receiver for a 25-KW(e) Gas Turbine," Mechanical Engineering, Jan. 1981, pp. 26-29.

APPENDIX G

CONTAINMENT OF HEAT STORAGE ALLOYS

Nikhil S. Nagaswami

ABSTRACT

The present work is directed towards finding optimum containment materials for several recently discovered heat storage alloys. These alloys include binary, ternary and quarternary systems of the elements aluminum, copper, magnesium, zinc, phosphorous and silicon, all fabricated or synthesized at the University of Delaware by Alan Riechman and Diana Farkas. The commercial viability of these systems hinges on their proving more cost effective as compared to several molten salt systems in their respective temperature ranges. Since it is anticipated that the containment system could prove to be as or more expensive than the storage media, this area of research warrants close study.

The containment materials must satisfy several requirements, amongst them: good thermal stability in the temperature range, thermal shock resistance, high strength at elevated temperatures, and remain inert to attack by the alloy, that is, they must exhibit limited solubility, resistance to embrittlement, little or no decomposition, resistance to infiltration or liquid metal penetration (unless the infiltration enhances strength) and form a very slowly growing reaction layer that is protective.

Experimental studies completed and in progress include:

A study of wetting, reaction layer growth, and alloy penetration and diffusion into the containment material, upon exposure, without pressure at temperatures 100 to 150°C above the melting points of the alloys.

Similar studies are also being done for the individual elements comprising these alloys.

The experimental techniques employed in the present work include optical metallography, scanning electron microscopy and electron probe microanalysis.

Six alloys systems are presently being studied. These include three alloys which show good heat storage properties on a volume basis and three alloys that are good on a weight basis. These alloys show promise for application in three temperature ranges: 550-625°, 700-800°, and 950-1050°C.

The containment materials being studied include two stainless steels, S.S.304 and S.S.316L, and a cheap silicon carbide compact, "Carbofrax SiC," from the Carborundum Company.

In all the systems studied thus far, the SiC shows great promise as a containment material, while the stainless steels are attacked to a greater degree by the molten alloys. A conclusive report on all studies conducted will be available soon.

INTRODUCTION

An extensive literature survey has been conducted and various aspects of the containment problem studied. These include: liquid metal and solid-vapor phase embrittlement of metals and refractory structural materials, including mechanisms of embrittlement, specificity of embrittlement, rates of embrittlement, and nature of embrittlement; reaction of liquid metal-structural material couples and modes of decomposition, attack and material diffusion, surface phenomena and morphologies and effect on liquid metal interactions, infiltration of metals and refractory materials by liquid metals, silicon carbide--its preparation, properties and reactions, stainless steels--their properties and the effect of liquid metal environments, analytical procedures and theory behind SEM, TEM, STEM and diffraction studies and applications to the present problem, heat storage alloy applications and future trends for research.

The conclusions of the literature search are presented in the introduction to the thesis based on the present work.

EXPERIMENTAL DETAILS

Alloy Preparation

The first method utilized in preparing the alloys was melting in a resistance furnace under argon atmospheres. The alloying elements were mixed in a graphite crucible which was closed with a tight fitting lid, incorporating a stirrer to facilitate mixing of the molten alloy. The tight fitting lid was used to minimize vaporization losses, particularly of the elements Zn, Mg and P. The set up is illustrated in Figure 1.

The temperature of melting depended on the volatile elements Zn, Mg. P present and on the highest melting constituent present. The graphite crucible containing the elements was introduced into the furnace which is preheated to the melting temperature desired and flushed with argon prior to and during the melting process. The alloy is cooled in the argon atmosphere by switching off the furnace and maintaining the argon flow.

This method proved largely unsuccessful owing to several reasons:

1) When the temperature was maintained at the melting temperature of the highest melting constituent, excessive vaporization of the volatile elements occurs.

FIG 1

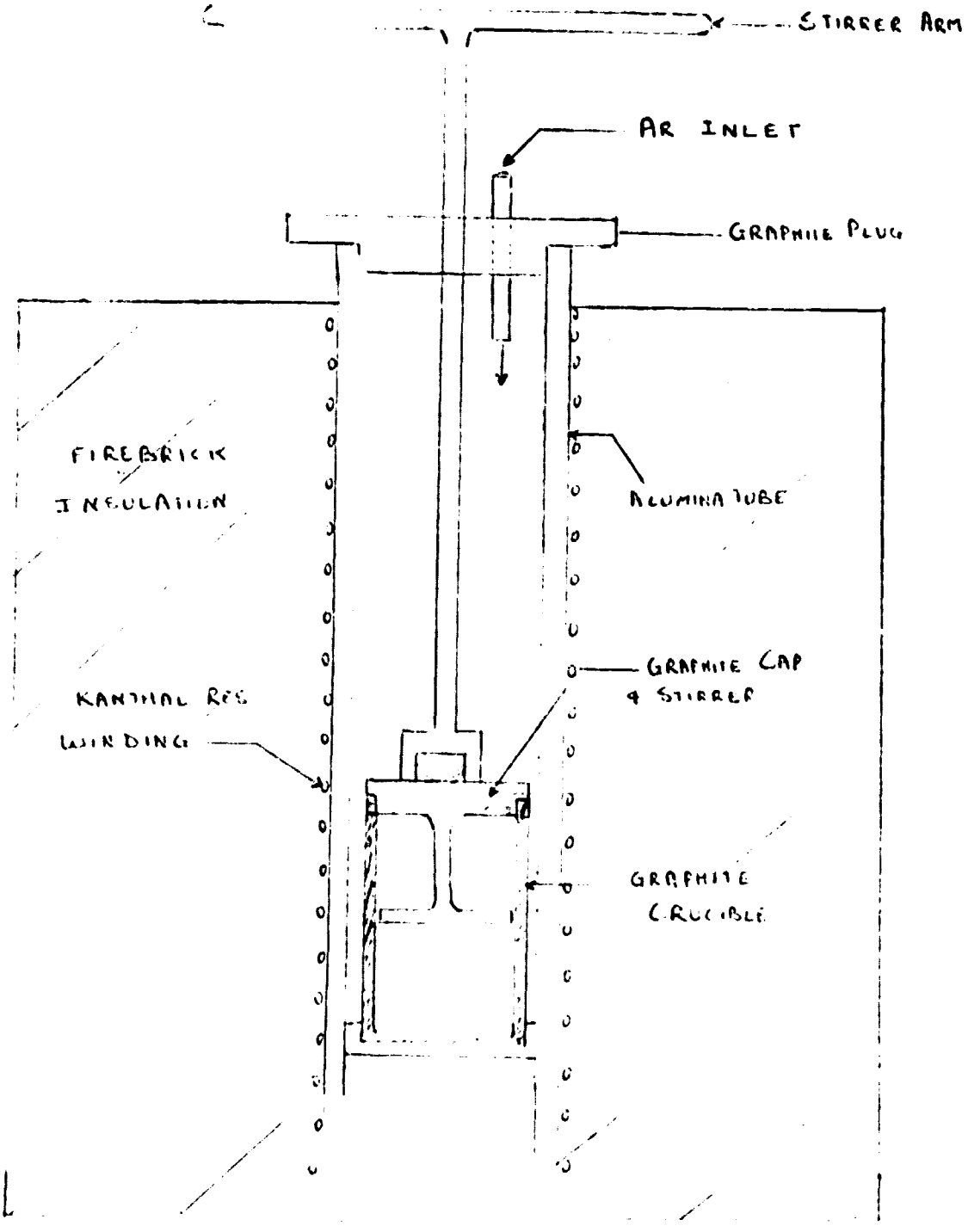
STIRRER ARM
AR INLET
GRAPHITE PLUG
FIREBRICK INSULATION
ALUMINA TUBE
GRAPHITE CAP & STIRRER
KANTHAL RES. WINDING
GRAPHITE CRUCIBLE

2) When the melting temperature is held intermediate between the melting temperatures of the volatile and high melting elements, incomplete melting occurs and the alloy is extremely heterogeneous.

3) Owing to the air trapped in the crucible within the alloying element mix, considerable oxidation of the alloying elements occurs, resulting in incomplete melting and mixing and in a porous sintered mass, even at temperatures higher than the melting temperature of the highest melting element.

In seeking a solution to the above problem the following set up was utilized (Figure 2).

The alloying elements (in the form of chunks--not powders) were weighed and mixed in a graphite crucible, which is placed within a quartz tube as shown. The quartz tube is fitted with an air tight seal and evacuated at room temperature to remove almost all the air in the alloying element mix. The vacuum tight valve is then closed and the tube flushed with argon. In this state, the quartz tube placed within a set of water cooled Cu induction coils is heated. An argon pressure in the tube is maintained by regulating inlet-outlet pressures, while the graphite crucible and "chunky" elements provide for good coupling with the induction coils. Temperatures are measured by means of a thermocouple and an optical pyrometer. Following the melting, the alloy is cooled under argon.

FIG 2

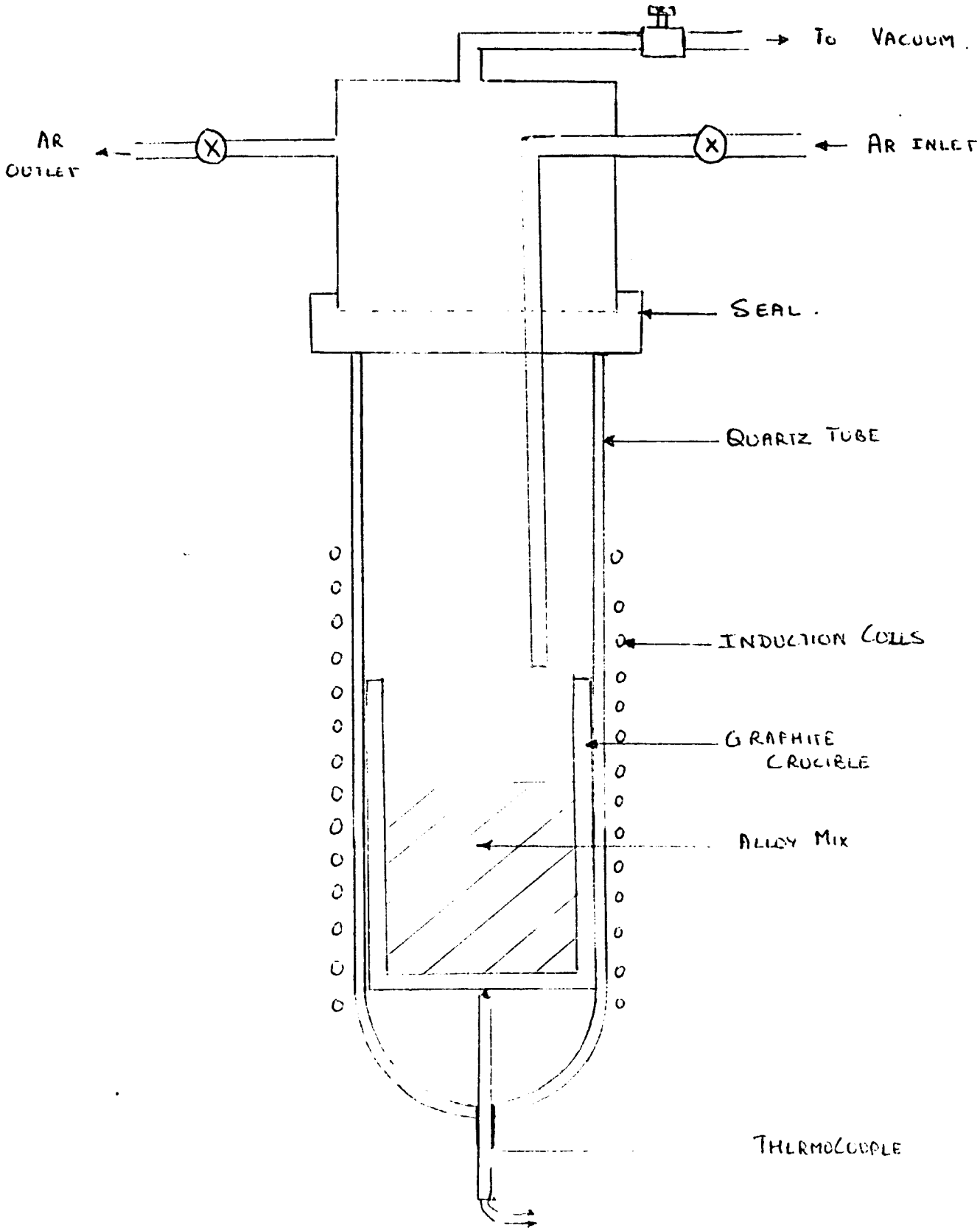
To VACUUM.
AR OUTLET
AR INLET
SEAL.
QUARTZ TUBE
INDUCTION COILS
GRAPHITE CRUCIBLE
ALLOY MIX
THERMOCOUPLE

This system provides for quick, convenient melting of the alloys and minimizes vaporization losses. In addition the induction furnace set up provides good mixing of the alloying elements, while minimizing oxidation due to trapped air.

Containment Study

The experimental set up utilized in this study is illustrated in Figure 3.

A tube furnace constructed by winding Kanthal resistance wire around a high grade alumina tube and packed with refractory firebrick insulation is used. A high density mullite tube is mounted within the alumina tube to provide a contamination-free environment (with minimum outgassing of the heater tube) and to provide more uniform temperatures in the effective reaction zone. A gas inlet port is cemented at one end of the mullite tube. At the other end a nearly gas tight closure has a sliding face shield to facilitate insertion and removal of the specimen holder and temperature measurement. Tantalum baffles are inserted into the mullite tube between the specimen holder and the ends to minimize heat loss to the ends and to provide a uniform temperature zone over the length of the specimen holder. The construction of the specimen holder is illustrated in Figure 4. The entire holder is constructed of 304 SS and is free of warpage upon heating and cooling. The alloy/base material samples are placed in

Furnace Assembly for Specimen Heating.

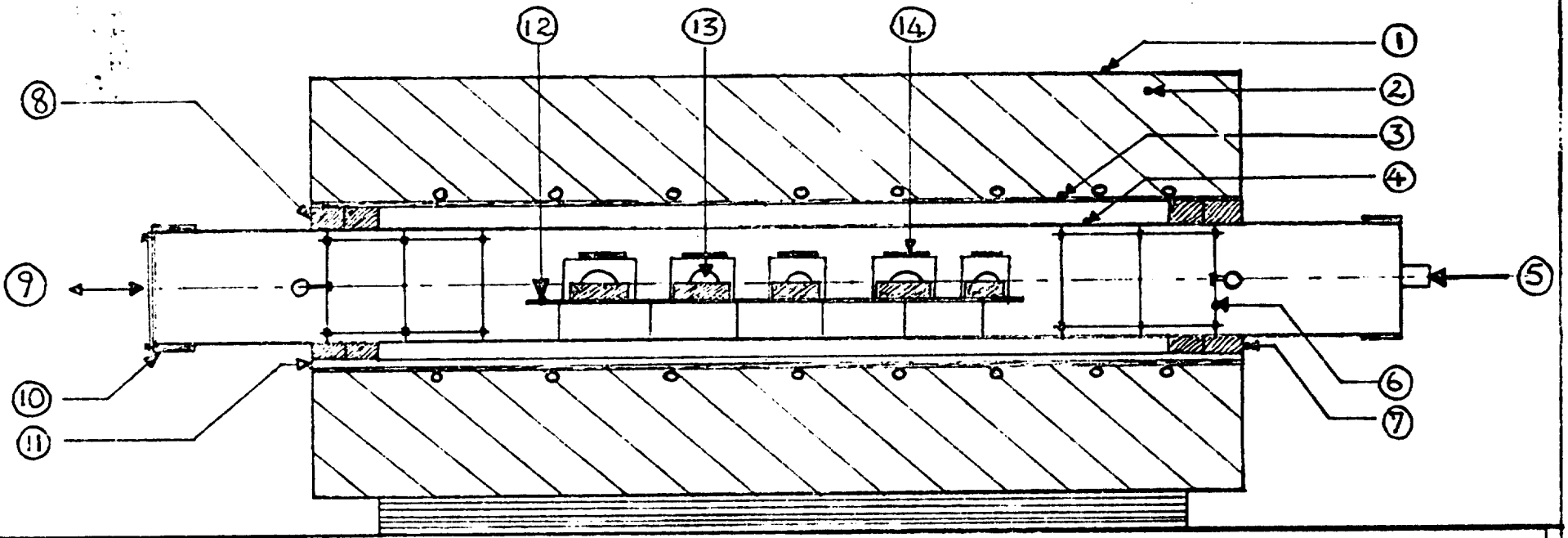

Index.

1. Furnace Casing.
2. Fireclay Refractory.
3. Kanthal Wound, Alumina Refractory Tube.
4. Mullite Refractory Tube.
5. Argon Inlet Port.
6. Tantalum Heat Baffle.
7. Alumina Cement.
8. Alumina Cement
9. Specimen Removal Stage.
10. Stainless Steel Airtight Ends.
11. Thermocouple Sleeve.
12. Warp Free - Specimen Support.
13. Alloy / Containment Material.
14. Airtight Protective Caps.

FIG 4.

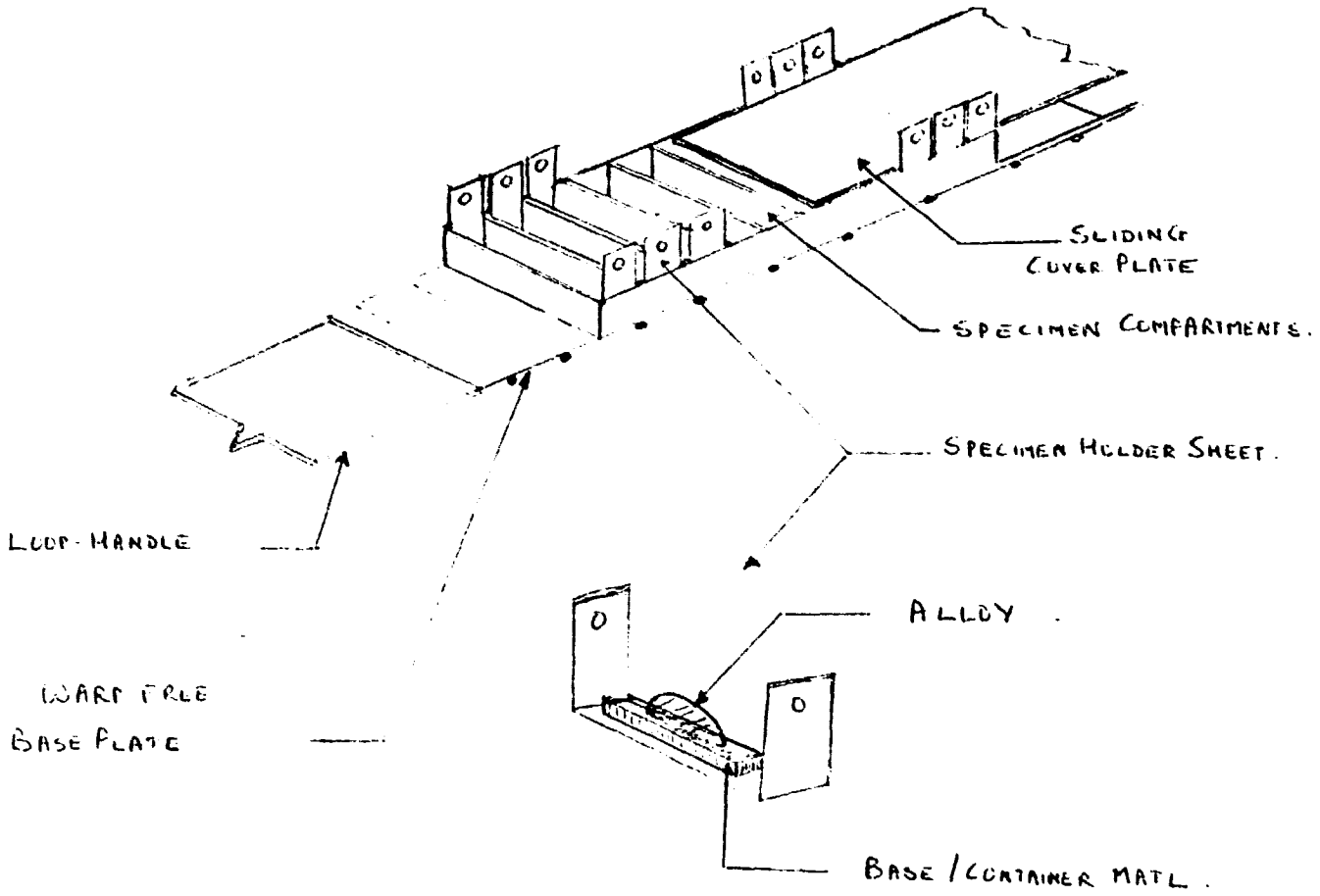
SLIDING COVER PLATE
SPECIMEN COMPARTMENTS.
SPECIMEN HOLDER SHEET.
LOOP-HANDLE
ALLOY.
WARP FREE BASE PLATE
BASE/CONTAINER MATL.

individual receptables in the holder and are removed by means of a tight fitting SS304 strip bent to fit the receptacle. Each sample is further isolated in its receptacle by means of a tight fitting SS304 sheet which slides over the holder, thus preventing excessive volatilization and loss of elements and contamination of samples.

The reaction temperature is maintained 100-200°C above the melting point of the alloy, to allow enhanced reaction/diffusion/penetration rates and ensure complete melting of the alloys. Volatilization of the elements from the alloy is much lower than it is from the elements themselves and does not require using the minimum temperatures required for melting.

The specimen holder with the samples isolated by the covering strip is introduced into the furnace which is flushed with argon and maintained at temperature. The furnace is closed off, and an argon flow sufficient to maintain a pure atmosphere is provided. The durations of the exposures used are 24, 48, 100, 300 hours, done in individual batches. Following each heat the specimens are cooled to room temperature in the argon atmosphere by switching off the furnace heat. The samples are then removed carefully and identified prior to analysis.

Analytic Procedures

The samples obtained in the containment study (alloy element or alloys on base material) are visually inspected for extent of wetting and reaction.

In those instances that the alloy wets the base or forms a sessile drop on cooling, the effect is recorded using an optical metallograph.

The alloy is then ground off the base material to within 0.5mm of the surface, and the base is sectioned by means of a diamond impregnated cutoff wheel. Different grades of abrasive wheel are used for the SS304, 316 and SiC samples. The cutoff position is selected to obtain a representative section.

The sample is then mounted in epoxy resin (cured at room temperature). Alumina fillers are used to improve the hardness and abrasion resistance of the mold to more closely match the sample, thus providing better edge retention and minimizing relief between sample and mount.

The samples are then ground on SiC papers down to 600 mesh and subsequently polished on diamond impregnated cloths (low nap for better retention of inclusions and precipitates) for SiC and SS304 and 316. Alumina polishing abrasives are used also in the case of the stainless steels. The final grade of abrasive used is down to 0.25μm.

The sample surface is thus polished flat and free of surface relief, well suited for SEM observation and EDAX analysis.

Problems associated with smearing the softer alloying elements are thus minimized and practically eliminated by grinding off excess alloy, sectioning through the unattacked rear face of the sample, grinding and polishing while keeping the specimen reaction edge suitably oriented, and cleaning efficiently by means of swabbing with alcohol, using ultrasonic baths between preparation stages and at the end of preparation.

Etching is only carried out on as-received samples of the base materials and on base materials subjected to the same thermal cycles under argon as the alloy/base material samples, to remove artifacts due to thermal cycling alone, such as alloying element segregation.

SEM micrographs are used to study the growth of surface reaction layers and penetration-infiltration of the base material, while EDAX-electron microprobe analysis, performed on beam-size spots and in-line scans at successive depths into the base material from the reaction layer, are used to study elemental diffusion and distribution. Suitable corrections (ZAF, magnification, specimen tilt with respect to electron beam and detector window) are applied and spectral artifacts eliminated prior to analysis of the results obtained.

This system of analysis is seen to provide an effective, reliable means of studying the containment problem.

Preliminary qualitative results are included in Figures 5a-f.

SUMMARY

The alloy systems used are listed in Table 1 along with related physical and thermal properties.

The base materials studied include SS304, SS316L and SiC ("Carbofrax" from Carborundum Co.).

Results obtained to date indicate considerable reactivity of the stainless steels towards several of the heat storage alloys, while the SiC remains inert or forms a very slowly growing reaction layer with the molten alloys. The surface oxide on SiC has been found to be principally responsible for the poor wetting characteristics exhibited by the alloys. However, since several examples are cited in the literature wherein the liquid metal finally diffuses in through a resistant surface layer to attack the bulk or undermines the surface layer by initial infiltration at a crack, additional studies are being undertaken wherein the SiO_2 layer on the SiC samples is removed to the extent possible by means of treatments with HF.

Figure 5. Reaction of stainless steels and silicon carbide with molten heat storage alloys. Elemental diffusion curves are based on the longest exposure indicated. Concentrations are relative. The apparent effective thickness of the reaction layer and its dependence on time is shown at the top of each curve.

[M. Pt.: 585°C]

ALLOY: AL - 12% SI (AT %).

a

BASE MATL: S.S. 304

6 HRS

16 HRS

REACTION LAYER GROWTH

ELEMENT CONCENTRATION (REL)

AL.

SI.

'R DISTANCE INTO BASE MATERIAL

b

BASE MATL: SiC.

6 HRS
12 HRS
24 HRS
2 WEEKS
3 WEEKS.

REACTION LAYER GROWTH

SI

Cu

ELEMENT CONCENTRATION (REL)

'R DISTANCE INTO BASE MATERIAL

[M.Pt.: 770°C]

ALLOY: Cu - 27% Si - 17% Mg

c

BASE MATL: S.S. 304.

6 HRS.
12 HRS.
16 HRS

REACTION LAYER GROWTH

ELEMENT CONCENTRATION (REL).

Cu.

Si

Mg

⊥'R DISTANCE INTO BASE MATERIAL

d

BASE MATL: SiC.

6 HRS.
12 HRS.
24 HRS.

REACTION LAYER GROWTH.

ELEMENT CONCENTRATION (REL).

Si

Cu

Mg

⊥'R DISTANCE INTO BASE MATERIAL.

[M.Pt.:520°C] ALLOY: AL - 22% CU - 18% MG - 6% ZN. (AT.%)

e

BASE MATL: S.S. 304.

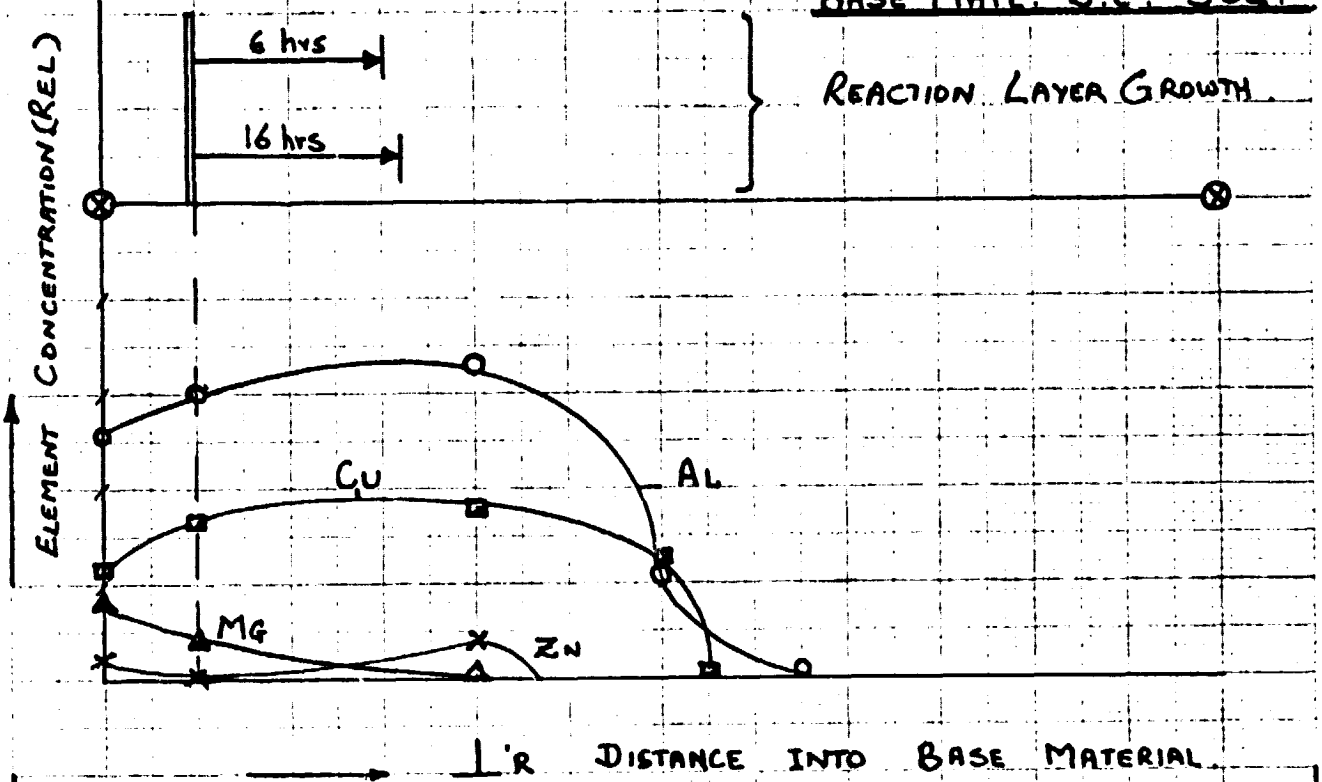

f

BASE MATL. SiC.

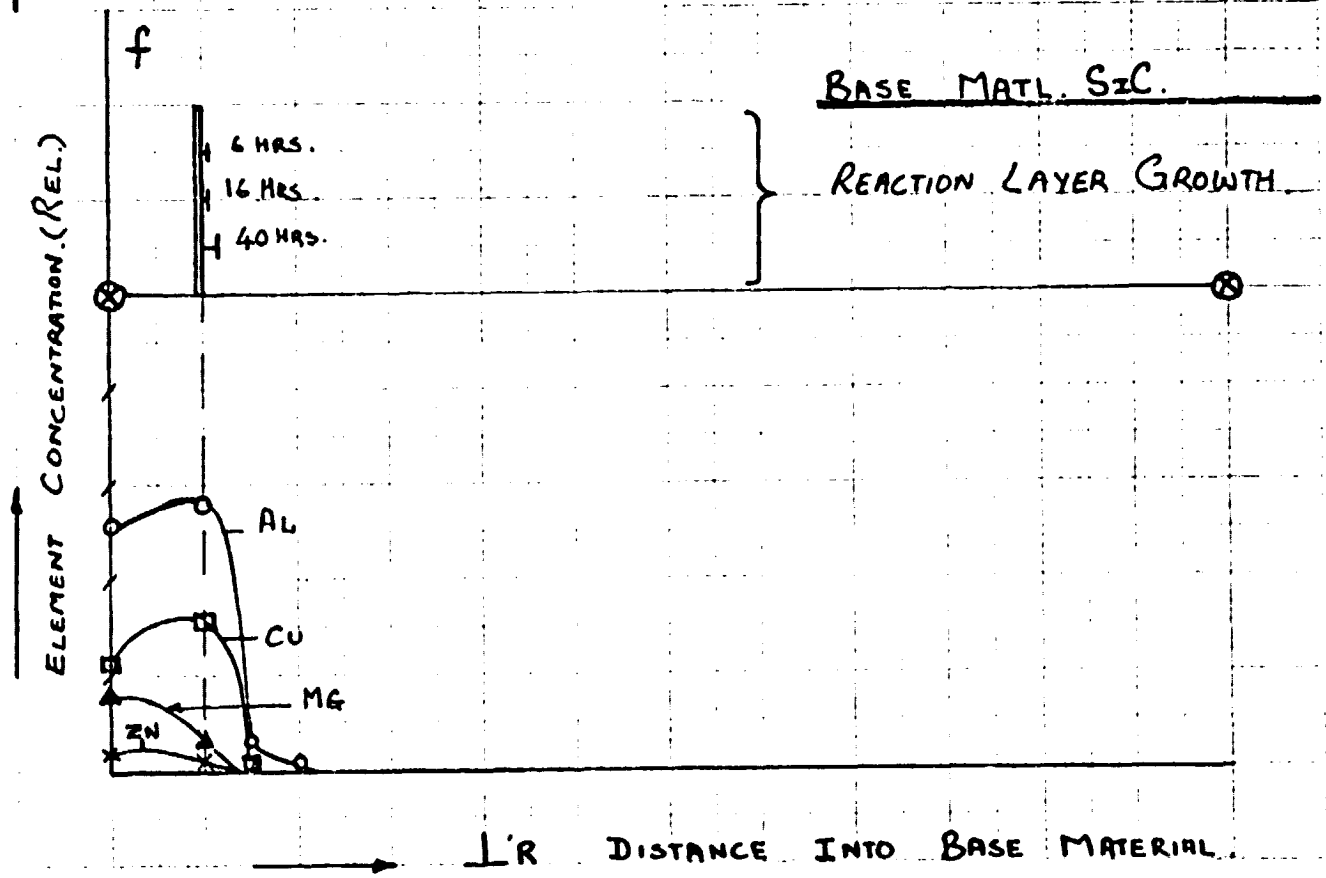

Additional areas of research worthy of study in finding a solution to the present problem include:

a) Special surface or heat treatment of the stainless steels.

b) Studies on SiC surface layer structures and the dependence of liquid metal interaction on this aspect.

c) The development of SiC coatings and their use with stainless steels or other suitable structural material to overcome certain commercial drawbacks in the shaping of complex SiC shapes.

d) Containment studies carried out over long periods and under pressures such as that to be found at the bottom of a tall liquid alloy bath.

e) Effect on mechanical properties of the base materials due to reaction/infiltration by liquid metals.

TABLE 1

ALLOY DATA

ALLOY (MOLE FRACTIONS)	EUTECTIC TEMP °C	ΔH_f (KJ/KG)	DENSITY (KG/M³)	ΔH_f (KJ/M³ x 10⁻⁵)	$C_{p_{SOLID}}$ KJ/KG · °K.	
AL - 0.126Si - 0.05Mg	560	545	2300	12.54	1.39	*
AL - 0.12Si	579	515	2250	11.59	1.49	*
ZN - 0.4Cu - 0.1Mg	705	191	8070	15.26	0.42	◎
Cu - 0.02P - 0.14Zn	720	318	9000	25.76	0.54	◎
Si - 0.35Cu - 0.2Mg	776	423	4150	17.55	0.75	◎
Si - 0.47Mg	946	959	1900	14.38	0.79	*

* . ALLOYS BASED ON KJ/KG BASIS

◎ ALLOYS BASED ON KJ/M³ BASIS